

**EXPLORING THE SPATIAL REGULATION OF FcεRI SIGNALING WITH SUPER-
RESOLUTION FLUORESCENCE LOCALIZATION MICROSCOPY**

A Dissertation

Presented to the Faculty of the Graduate School
of Cornell University

in Partial Fulfillment of the Requirements for the Degree of
Doctor of Philosophy

By

Sarah Ann Shelby

January 2015

© 2015 Sarah Ann Shelby

EXPLORING THE SPATIAL REGULATION OF FcεRI SIGNALING WITH SUPER-RESOLUTION FLUORESCENCE LOCALIZATION MICROSCOPY

Sarah Ann Shelby, Ph. D.
Cornell University 2015

Allergic signaling is initiated on the plasma membrane of mast cells through cross-linking of immunoglobulin E (IgE) bound to its receptor, FcεRI, by multivalent antigen. Signaling proceeds through controlled spatial assembly of FcεRI receptors with interaction partners in a process that gives rise to specific signaling outcomes. Antigen-stimulated redistribution of signaling molecules has proven difficult to characterize by fluorescence imaging due to the small length scales over which this redistribution occurs. We employ super-resolution fluorescence localization microscopy to measure antigen-stimulated changes in the nanoscale organization and mobility of FcεRI, as well as its spatial association with its signaling partner Lyn kinase, with the goal of understanding the physical mechanisms by which spatial redistribution of signaling molecules on the membrane causes the initiation of the signaling response.

Using super-resolution imaging, we record receptor organization and dynamics on live mast cells undergoing antigen-mediated signaling, allowing us to measure nanoscale clustering and diffusion of FcεRI simultaneously. Through comparison of cross-linking-induced changes in these properties as a function of time, we are able to resolve two distinct temporal phases of receptor clustering and immobilization. We correlate the time-dependence of the distinct phases with a functional signaling

response, Ca^{2+} mobilization, to assess the relevance of each phase to the onset of signaling.

We also use super-resolution imaging to measure interactions of $\text{Fc}\epsilon\text{RI}$ with Lyn. Because of the improved resolution of our imaging technique, we detect coupling of Lyn to cross-linked IgE- $\text{Fc}\epsilon\text{RI}$ that occurs at early stages after antigen stimulation and is associated with the initiation of the stimulated response. Lyn association with $\text{Fc}\epsilon\text{RI}$ is assessed through direct imaging, and we can measure the average physical properties of Lyn/ $\text{Fc}\epsilon\text{RI}$ co-clusters. Through this quantitative approach, we examine mechanisms of regulation of Lyn co-redistribution with IgE- $\text{Fc}\epsilon\text{RI}$. In particular we show that the actin cytoskeleton negatively regulates $\text{Fc}\epsilon\text{RI}$ signaling by reducing the local accumulation of Lyn with $\text{Fc}\epsilon\text{RI}$ clusters during the onset of the response. The spatial resolution afforded by this technique makes it an effective tool for investigating interactions that give rise to the changes in the organization or mobility of signaling molecules during the initiation of signaling, and how these changes translate into cellular functions.

BIOGRAPHICAL SKETCH

Sarah was born on July 16, 1986 to Diane and Robert Shelby in San Jose, California, 10 minutes after her twin sister Megan. Sarah spent most of her childhood and young adult years traipsing around the woods with her siblings and dogs, cooking, and building things before trading her suburban Bay Area hometown for life in Berkeley, CA to attend college. Sarah was at the University of California, Berkeley from 2004 to 2008, during which time she earned a degree in Chemical Biology and discovered the wonders of lipid membranes while conducting undergraduate research on the interface between lipid bilayers and silver nanoparticles in the lab of Professor Jay T. Groves. After graduation, Sarah took a year "off" to work at the Biological Nanostructures division of the Molecular Foundry nanoscience center at Lawrence Berkeley National Laboratory. There, she worked in the lab of Dr. Ron Zuckermann on another kind of self-assembled bilayer made of protein-mimetic polymers, and enjoyed a truly spectacular view of the San Francisco Bay from her bench. Attracted by the vibrant biomembrane research community at Cornell, Sarah came to Ithaca in 2009 to pursue a graduate degree in Biophysics. She was taken under the wing of Dr. Sarah Veatch and was soon inducted into the Baird-Holowka Lab. Here, her research project has taken a decidedly more biological turn, but remains resolutely nano-sized. Sarah is going on to a post-doctoral position with (now Professor) Sarah Veatch at the University of Michigan in Ann Arbor.

For Megan, who understands.

ACKNOWLEDGEMENTS

It's more than a little baffling to think that my graduate career is coming to a close, but during occasional moments of clarity I am a bit shocked by how much I've learned over the past five and a half years. I have my advisors, colleagues, and friends to thank for that. Of course, the two people who deserve the most credit are Barbara Baird and Dave Holowka. Together, they have helped me come into my own as a scientist and have cultivated my appreciation for a two-pronged attack of big-picture thinking and flawless execution. At the same time they manage to be genuinely wonderful people and have made the lab feel like a second home. Thanks to Warren Zipfel. For better or worse, working with him has removed any reservations I previously had against disassembling, large, delicate, and expensive pieces of optical equipment. I also certainly owe a lot to Sarah Veatch, who can rightfully claim to have taught me (almost) everything I know that Dave didn't teach me. She has been and will continue to be an incredibly insightful and thoughtful mentor and friend.

Thanks to all past and present members of the Baird-Holowka Lab. Team BRB: Norah, Josh, Kate, Devin, Lily, and, Eshan. Thanks for letting me hassle you into leaving lab early on Fridays. My other fellow members of Team Balowka through the ages: Roselynn, Jordan, Marcus, Marek, Kirsten, Chris, Kari, Amit, Deepti, Jinmin, and Alice. Thank you for brightening my days, for peer pressuring me into signing up for races, and for all of the delicious cake.

For keeping life outside of lab interesting, thanks to my fellow Biophysicists and other Ithacan friends especially Delbert, Sara, Brendan, Nate, Andrea, Ruth, and most

of all Norah, who is constantly revealing herself to be even more competent and generous than I had previously thought. My California buddies, especially my fellow Ph. D.-seekers, former cubicle-sharers, and my best, oldest friends are a very strong and very exuberant base of support.

Speaking of exuberance, thanks to Chris, who deserves a lot of credit for his dedication to the self-appointed job of Head Cheerleader over the last few years in spite of my equally relentless efforts to discredit him.

Thanks to my parents. From a young age, my mother has been fast and furious with encouragement that I was capable of great success in being whatever I wanted to be, and my father, who has his own Ph. D., is someone who I have always aspired to become more like. If I had to choose two people who were most responsible for fostering my love of science, which ultimately led to my decision to go for a doctorate, it would be them. My step-parents and siblings have been unbelievably understanding, loving, and most importantly a lot of fun to be around.

There are far too many people to name who deserve thanks, so before I attempt to do just that: thank you. Thank you all so so so much.

TABLE OF CONTENTS

Biographical Sketch.....	v
Dedication.....	vi
Acknowledgements.....	vii
Table of Contents.....	ix
List of Figures.....	x
List of Abbreviations	xiii
Chapter 1. Introduction	
The Immunological Response to Allergen.....	1
Heterogeneous Organization of the Plasma Membrane	3
Super-Resolution Fluorescence Localization Microscopy.....	11
Current Studies.....	17
References.....	20
Chapter 2. Distinct Stages of Stimulated FcεRI Receptor Clustering and Immobilization are Identified Through Super-Resolution Imaging.	
Summary.....	29
Introduction.....	30
Material and Methods.....	32
Results and Discussion.....	44
References.....	97
Chapter 3. Antigen-Stimulated Nanoscale Co-Localization of IgE Receptor with Lyn Kinase is Regulated by the Actin Cytoskeleton.	
Summary.....	103
Introduction.....	104
Material and Methods.....	108
Results and Discussion.....	119
References.....	159
Chapter 4. Conclusions and Future Directions	
Conclusions.....	165
Future Directions.....	169
References.....	172
Appendix A. Super-Resolution Imaging of IgE Receptor Cross-Linking by Structurally-Defined Ligands in RBL Mast Cells.....	174
Appendix B. Registration of Two-Color Super-Resolution Fluorescence Localization Images.....	190

LIST OF FIGURES

1.1	FcεRI clustering triggers a degranulation response via a signaling cascade.	5
1.2	Schematic of super-resolution localization microscopy image rendering.	13
2.1	Quantitative super-resolution localization microscopy TIRF imaging of IgE-FcεRI redistribution after antigen addition in chemically fixed cells.	45
2.2	RBL-2H3 cells retain the antigen-stimulated responses in super-resolution imaging buffer.	52
2.3	Quantitative super-resolution localization microscopy imaging of IgE-FcεRI redistribution after antigen addition in live cells.	56
2.4	Antigen stimulation leads to slower and more confined diffusion of IgE-FcεRI receptor complexes.	62
2.5	Average receptor diffusion displays two different phases of dependence on the number of proteins in the average cluster.	67
2.6	Average receptor diffusion vs. correlation amplitude and correlation length.	68
2.7	Slower and more confined diffusion of single receptors correlates with regions of high receptor density.	72
2.8	Distributions of single-trajectory diffusion constant are broader than expected for Brownian diffusion post-stimulation.	75
2.9	Antigen-induced changes in receptor clustering and mobility are reversible.	79
2.10	The shape, frequency, and duration of Ca ²⁺ oscillations are severely affected by changes in cellular cholesterol.	82
2.11	Cholesterol perturbations affect the extent of antigen-stimulated degranulation as measured by β-hexosaminidase release.	85
2.12	Perturbations of membrane cholesterol alter receptor clustering.	87
2.13	Perturbations of membrane cholesterol have corresponding effects on receptor diffusion, receptor clustering, and cellular Ca ²⁺	88

	responses.	
2.14	Cholesterol perturbation affects average parameter values in live cell experiments.	91
3.1	Two-color super-resolution imaging measures distributions of IgE receptor and Lyn as a function of antigen stimulation.	121
3.2	Pair-correlation analysis shows stimulation time-dependent nanoscale co-localization of IgE-FcεRI and Lyn.	125
3.3	4G10/IgE-FcεRI cross-correlation amplitude increases with stimulation time.	131
3.4	Cortical actin undergoes dynamic reorganization in the first minutes after antigen addition.	134
3.5	Antigen-stimulated coupling of IgE-FcεRI to actin is not readily detectable by two-color super-resolution imaging.	137
3.6	Inhibition of actin polymerization enhances Lyn/IgE-FcεRI cross-correlation amplitude.	140
3.7	Lyn mEos3.2 and Dy654 IgE auto-correlation fit parameters for cells treated with actin polymerization inhibitors.	142
3.8	Receptor-correlated phosphotyrosine is enhanced due to inhibition of actin polymerization.	149
3.9	Increased receptor phosphorylation due to cytochalasin and latrunculin is mediated by Lyn.	151
3.10	Lipid anchorage of mEos3.2 constructs determines antigen-induced recruitment to IgE/FcεRI and the effects of cytoskeletal perturbation.	155
A1	Schematic of Y _n DNP ₃ ligands.	175
A2	Y ₁₆ DNP ₃ addition causes rapid clustering of IgE-FcεRI in super-resolution images.	178
A3	Pair auto-correlation functions are used to quantify receptor clustering as a function of Y ₁₆ DNP ₃ stimulation time.	179
A4	Average IgE-FcεRI mobility drops quickly after Y ₁₆ DNP ₃ addition.	180

A5	IgE-Fc ϵ RI mobility and average physical properties of clusters depend on the stimulating ligand.	182
A6	The relationship between ligand-induced immobilization and number of correlated proteins depends on the ligand used.	183
A7	Live cell images reflect ligand-induced immobilization of the population of IgE-Fc ϵ RI complexes.	184
A8	The whole population of IgE-Fc ϵ RI complexes is more rapidly immobilized by Y ₁₆ DNP ₃ stimulation than by DNP-BSA.	187
B1	Two-color imaging systems have significant nonlinear offsets between channels that extend well beyond the resolution of a single-color fluorescence localization image.	192
B2	One channel can be effectively spatially mapped onto the other using a piecewise, non-linear transformation.	195
B3	The drift in the emission splitting system can cause drift in the alignment transformation over time.	197
B4	Control experiments using fluorescent nanospheres that simulate super-resolution localization data collection routines confirm channel alignment.	199

LIST OF ABBREVIATIONS

AF488	AlexaFluor 488
AF532	AlexaFluor 532
AF647	AlexaFluor 647
Ag	antigen
BSS	buffered saline solution
BCR	B cell receptor
BME	Beta-mercaptoethanol
Ca ²⁺	soluble calcium ion
Cpb	Csk-binding protein
CRAC	Calcium release activated calcium
Csk	C-terminal Src kinase
CytoD	Cytochalasin D
DAG	diacylglycerol
DCT	DNP aminocaproyl-L-tyrosine
DNP	Dinitrophenyl
DNP-BSA	Bovine serum albumin decorated with dinitrophenyl groups
Dy654	Dyomics 654
Ebp50	Ezrin-binding protein 50
EM-CCD	Electron-multiplying charge-coupled device
ER	endoplasmic reticulum
ESR	Electron spin resonance
F-actin	Filamentous actin
FBS	Fetal bovine serum
FFT	Fast Fourier transform

FRET	Förster resonance energy transfer
FCS	Fluorescence correlation spectroscopy
FPR	Fluorescence photobleaching recovery
fps	Frames per second
GG	geranylgeranyl
GPI	glycophosphosphatidylinositol
GTT	glutathione
GEM	glycolipid-enriched microdomains
HA	Hemagglutinin A
IgE	immunoglobulin E
IB	Imaging buffer
IP ₃	inositol-1,4,5-bisphosphate
IP ₃ R	inositol-1,4,5-bisphosphate receptor
ITAM	immune tyrosine activation motif
LAT	linker for the activation of T cells
LatA	Latrunculin A
lwm	Local weighted mean
MβCD	Methyl-beta-cyclodextrin
MβCD+chol	Methyl-beta-cyclodextrin complexed with cholesterol
MEM	Modified Eagle medium
MSD	Mean squared displacement
MIRR	multi-chain immune recognition receptor
N.A.	Numerical aperture
OS	Oxygen-scavenging
PAG	Phosphoprotein associated with GEMs
(f)PALM	(fluorescence) photo-activation localization microscopy

PI(4,5)P ₂	phosphatidylinositol-4,5-bisphosphate
PKC	protein kinase C
PLC _γ	phospholipase C-gamma
PM	plasma membrane
PSF	Point spread function
PTP _α	Protein tyrosine phosphatase alpha
RBL	Rat basophilic leukemia
SEM	Scanning electron microscopy OR standard error of the mean
SH2	Src homology 2
SOC	store operated calcium
SOCE	store operated calcium entry
SPT	Single particle tracking
(d)STORM	(direct) stochastic optical reconstruction microscopy
STIM1	Stromal interaction molecule 1
TCR	T cell receptor
TIRF	Total internal reflection fluorescence microscopy
Y _n -DNP ₃	Y-shaped DNA ligand with n base pairs and 3 DNP groups

CHAPTER ONE

INTRODUCTION

1. The immunological response to allergen

The symptoms of allergy are caused by an inflammatory response that is mediated by the immune system. Allergens bind specifically to immune cells within the body and trigger a strong pro-inflammatory biochemical cascade. Mast cells are tissue-resident cells of the immune system that mediate this inflammatory process in the body (1–3). Although they take on a variety of normal physiological functions, including the immune response to helminth parasitic infection (4), they are most well-known for their role in type I hypersensitivity allergic responses. Allergic disease has become an increasingly serious public health concern in the developed world. In the United States it is the 6th leading cause of chronic disease and affects over 50 million people annually (5). In the case of anaphalaxis, the reaction of mast cells to allergen is systemic and the resulting inflammatory response can be severe to lethal. The allergic response is the consequence of Immunoglobulin E (IgE) mediated signaling in mast cells, which causes release of chemical mediators of inflammation, such as histamines, from secretory granules within the cell (2).

1.1. *IgE signaling in mast cells*

IgE is one of the five isotypes of immunoglobulins secreted by B cells. In allergic individuals, allergen-specific IgE is secreted by B cells that have differentiated into

plasma cells following the initial encounter with the allergen. This IgE is circulated in the blood where it can be tightly bound by the high-affinity receptor for IgE (6), Fc ϵ RI, which is expressed in abundance on the plasma membrane of mast cells. Upon subsequent exposure to the allergen, IgE/Fc ϵ RI complexes are cross-linked in the plasma membrane due to specific, multivalent binding of the allergen to IgE. Receptor cross-linking initiates a transmembrane signaling cascade that ends in cellular degranulation, which is the release of secretory granule contents from the cell.

1.2. The Fc ϵ RI receptor

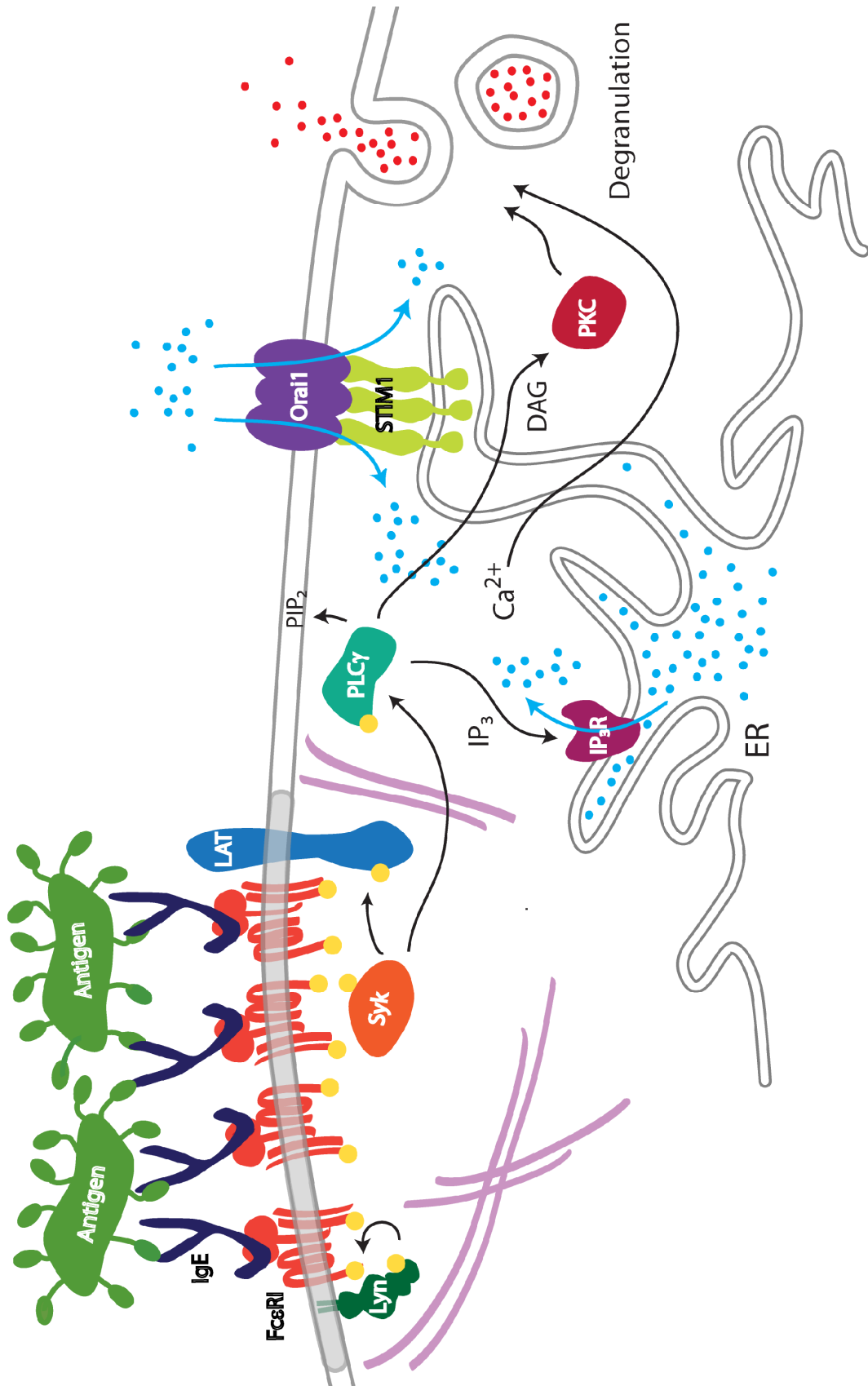
The Fc ϵ RI receptor functions to transduce the allergen or antigen detection signal across the plasma membrane. Together, Fc ϵ RI and Fc γ R receptors, T-cell receptors (TCR), and B-cell receptors (BCR) constitute the multi-chain immune recognition receptor (MIRR) family of receptors (7). Many basic features of B- and T-cell signaling are shared with the Fc ϵ RI system (8). Fc ϵ RI is a tetramer consisting of four transmembrane subunits: one α chain, one β chain, and two disulfide-linked γ chains. The α subunit binds IgE with high affinity via its extracellular domain (9). The β and two γ subunits extend primarily from the cytoplasmic side of the membrane and serve to propagate the activation signal. The β chain contains an immunoreceptor tyrosine-based activation motif (ITAM) that mediates binding of the Src family kinase Lyn for purposes of signal amplification. The γ chains also contain ITAMs that are phosphorylated upon receptor activation to recruit and activate Syk tyrosine kinase (10).

1.3. Receptor cross-linking induced signaling

Multivalent binding of antigen to IgE-FcεRI and resulting receptor cross-linking results in the initiation of a signaling cascade that ends in cellular degranulation. Fig. 1.1 shows a schematic of the signaling pathway. Lyn kinase is recruited to cross-linked receptors where it phosphorylates receptor ITAMs. Once phosphorylated, the ITAM on the β subunit has increased affinity for binding Lyn, resulting in amplification. Phosphorylated ITAMs on the γ subunits recruit Syk kinase via its tandem SH2 domains and Syk is phosphorylated and activated. Activated Syk phosphorylates a variety of substrates, importantly the adapter protein LAT and phospholipase C γ (11). Activated PLCγ at the membrane cleaves phosphatidylinositol-4,5-bisphosphate (PI(4,5)P₂) within the membrane, producing inositol-1,4,5-trisphosphate (IP₃) and diacylglycerol (DAG), which in turn activates protein kinase C (PKC). IP₃ diffuses through the cytosol before binding by IP₃ receptor on the endoplasmic reticulum. This in turn causes Ca²⁺ release from stores in the ER, which triggers coupling between STIM1 in the ER membrane and the Ca²⁺ channel Orai1 in the plasma membrane, resulting in Ca²⁺ influx in the process known as store-operated Ca²⁺ entry (SOCE) (12). Elevated cytoplasmic Ca²⁺ concentrations caused by SOCE together with PKC activation by DAG are necessary for the release of secretory granules containing pro-inflammatory mediators, including histamine, serine proteases, proteoglycans, and serotonin (13). Activation of mast cells also causes *de novo* production and release of cytokines and lipid mediators of inflammation (14).

2. Heterogeneous organization of the plasma membrane

Fig. 1.1 FcεRI clustering triggers a degranulation response via a signaling cascade. When IgE-FcεRI complexes are clustered through binding by multivalent antigen, active Lyn is recruited to receptors and phosphorylates receptor ITAMs, which recruit and activate Syk. Syk in turn phosphorylates LAT and PLCγ, which cleaves PIP₂ to produce IP₃ and DAG. DAG activates PKC. IP₃ binds IP₃ receptors, resulting in release of Ca²⁺ from stores in the ER. Depletion of ER stores causes STIM1 in the ER and Orai1 in the plasma membrane to assemble to form the CRAC channel and admit extracellular Ca²⁺ into the cell. Elevated cytosolic Ca²⁺ together with active PKC are required for initiation of cellular degranulation. *Figure modified and used with permission from Dr N.L. Smith.*



2.1. Cross-linking induces spatial and temporal reorganization of FcεRI

Receptor oligomerization has readily observable effects on the spatial distribution and diffusion behavior of IgE-FcεRI. While the receptor is randomly distributed and mobile on the membrane before activation, stimulation with soluble multivalent antigen causes clustering of IgE- FcεRI into discrete, punctate aggregates on the cell surface and is associated with a marked decrease in receptor mobility (15).

The physical structure of receptor clusters themselves is a major determinant of signaling outcome. A number of studies using engineered antigens or ligands for IgE have revealed a sensitivity of the signaling response to ligand valency and physical distance between IgE binding sites (16–18), both of which directly affect the structure of the resulting IgE-FcεRI clusters. Likewise, ligand binding affinity affects the signaling capacity of clustered receptors. Clustered receptors with readily dissociable cross-links effectively trigger degranulation responses, whereas poorly dissociable cross-links do not (19). Thus, the dynamic assembly of receptor clusters also has an important role in signaling. Changes in receptor mobility upon cross-linking are related to this process. Receptor diffusion decreases markedly following cross-linking, but the specific role for and mechanism of immobilization is unclear. Immobilization is readily observed under conditions that produce robust signaling responses (15, 20), but small, mobile clusters have also been shown to be signaling competent (21).

There is a continued need for efforts to address the questions of how specific receptor clustering and immobilization behaviors affect signaling outcomes. Namely, by what mechanisms does the spatial and temporal reorganization of receptors regulate coupling to the membrane environment and downstream signaling partners to lead to

differential responses by the cell. Lateral organization on the membrane is known to be important for cell signaling, and it is widely accepted that proteins and lipids are distributed in the plasma membrane in a heterogeneous fashion.

2.2. Lipid phase separation and the raft hypothesis

Membrane lipid phase behavior has been proposed to be an underlying physical contributor to the heterogeneous architecture of the plasma membrane and is thought to be a mechanism for membrane compartmentalization in cellular signaling. The propensity for lipids to phase separate into liquid ordered and liquid disordered phases has been observed in cholesterol-containing model membranes as well as membranes extracted from live cells (22, 23). The “raft hypothesis” (24) proposes that the interactions which generate phase separation in model membrane systems are present among plasma membrane lipids. It suggests that proteins and lipids that are found in liquid ordered vs. liquid disordered phases of model membranes will also preferentially associate in the plasma membrane to form regions in which order-preferring or -avoiding species are concentrated. However, these structures are unlikely to reflect the well-defined phase separation found in model membranes (25). Instead, the current definition of membrane rafts describes them as “small (10-200 nm), heterogeneous, highly dynamic, sterol- and sphingolipid-enriched domains that compartmentalize cellular processes”, which “can sometimes be stabilized to form larger platforms through protein-protein and protein-lipid interactions” (26).

2.3. The role of the actin cytoskeleton

Contacts with the cytoskeleton may also contribute to the functional organization of the plasma membrane. Single-particle tracking (SPT) experiments have shown that actin imposes diffusion barriers on membrane proteins and lipids (27, 28), suggesting that filaments act as partitions to compartmentalize membrane components within the cortical actin meshwork. These compartments or "corrals" are restricted to the dimensions of the meshwork and are typically only a few hundred nanometers in size (29). There is evidence showing that the actin cytoskeleton selectively interacts with structures formed by lipid-driven membrane heterogeneity and order-preferring proteins (30–32), and that the formation of clusters of raft-associated proteins is stabilized by actin (33, 34). Additionally, depletion of membrane cholesterol causes actin cytoskeletal rearrangement (35), and disruption of the actin cytoskeleton decreases membrane order (36), pointing to an interplay between actin-membrane contacts and membrane heterogeneity. Together, these data suggest that the actin cytoskeleton interacts with proteins and lipids arranged by membrane lipid domains to impose a higher level of organization and regulation on these structures.

2.4. Membrane heterogeneity affects mast cell signaling

Both lipid-driven membrane heterogeneity and the actin cytoskeleton have shown to be important in mast cell stimulation. Data from numerous biochemical studies have led to the conclusion that IgE-FcεRI receptor cross-linking causes it to stabilize liquid ordered-like membrane domains, and that this association is required for receptor phosphorylation and the propagation of the activation signal (37–40). Cross-linking of membrane components causes large-scale phase separation in model membranes of

defined composition, where GM1 complexed by cholera toxin partitions into the ordered phase (41), suggesting that cross-linking can alter protein-lipid interactions and stabilize lipid phase heterogeneity. Further, confocal microscopy shows co-segregation of cross-linked IgE-Fc ϵ RI with other raft-marking components under certain labeling conditions (42). Association of cross-linked Fc ϵ RI with liquid ordered-like regions leads to receptor phosphorylation through increased contact with active Lyn kinase, which itself is found within these domains (43). The exclusion of the disorder-preferring protein tyrosine phosphatase α (PTP- α) from membrane domains containing cross-linked IgE-Fc ϵ RI and active Lyn prevents dephosphorylation of both species (44–46). A similar mechanism of signal enhancement through co-segregation with Lyn in liquid ordered-like membrane domains has also been described for the B cell receptor (47).

The actin cytoskeleton also appears to be directly involved in the recruitment of Lyn to clustered IgE-Fc ϵ RI. Actin co-segregates with large-scale clusters of cross-linked receptors by confocal microscopy (31). In experiments where cells are stimulated by surface-patterned antigen, the recruitment of Lyn to IgE-Fc ϵ RI clustered over the patterned antigen is dependent on actin at the level of Lyn recruitment detectable by fluorescence microscopy (48). The actin adapter proteins paxillin and vinculin also co-localize with IgE-Fc ϵ RI over patterns (49), suggesting actin-membrane contact sites are involved in signaling. Single particle tracking experiments show that IgE receptors are confined within actin-defined domains and that the actin cytoskeleton is involved in immobilization of cross-linked receptors (50). A negative regulatory role for actin in the Fc ϵ RI signaling cascade has been suggested based on the enhancing effects of treatment with cytoskeleton-disrupting drugs such as cytochalasin D and latrunculin A

on receptor phosphorylation and degranulation (19, 31, 51). Together, these data represent mounting evidence that plasma membrane heterogeneity driven both by lipids and by actin is exploited by the cell to functionally compartmentalize and regulate signaling on the membrane.

The length scales of proposed actin- and lipid- induced organization of the plasma membrane as well as the scale of IgE receptor clustering itself are all under a few hundred nanometers (52–54). As a consequence, receptor clustering and membrane heterogeneity have proven difficult to directly visualize in intact cells at the relevant length scale in the tens to hundreds of nanometers because of the diffraction limit of light. Many experimental approaches have been taken to characterize FcεRI signaling on the nanoscale. These include FRET and ESR measurements of the dimensions of membrane lipid domains (55–58), FCS of FcεRI and Lyn kinase (59–61), and single particle tracking experiments of FcεRI (21, 50, 62). The need for nanometer resolution to map receptor spatial distributions at high resolution has motivated studies where electron microscopy was used to image immunogold-labeled IgE- FcεRI on stimulated and unstimulated cells (52). Recent work has quantitatively measured co-redistribution of Lyn and IgE-FcεRI into protein-rich clusters upon stimulation with antigen using scanning electron microscopy (SEM). Lyn and receptor co-clustering was seen to be dependent both on cholesterol and protein-protein interactions (53). Monte Carlo methods have also been used to simulate the nanoscale distributions of lipid phases and diffusion behavior of membrane proteins based on the minimal assumptions that lipid phase heterogeneity is based on critical fluctuations (63), which are pinned to a cortical actin meshwork (64, 65), and these simulation have now been validated by *in*

vitro experimental results (66). These approaches have contributed to our understanding of receptor signaling on the nanoscale, but have not yet allowed for collection of high resolution images and information on receptor dynamics under similar conditions or from the same sample. A more detailed understanding of the recruitment of downstream signaling proteins and the involvement of actin has been limited by currently available experimental techniques.

3. Super-Resolution Fluorescence Localization Microscopy

3.1. The concept of localization microscopy

The need for quantitative tools for the characterization of nanoscale membrane organization has led to the development of increasingly powerful biophysical techniques and instrumentation. Recent advances in fluorescence microscopy have enabled sub-diffraction imaging of biological samples using photo-conversion of fluorescent dyes. The first of these techniques emerged simultaneously from several independent laboratories. They include (direct) stochastic optical reconstruction microscopy (STORM/dSTORM) (67, 68) and (fluorescence) photo-activation localization microscopy (PALM /FPALM) (69, 70), and are together referred to as super-resolution localization microscopy.

Super-resolution localization microscopy is based on the principle that the fluorescence spot obtained from imaging a spatially isolated single molecule can be used to localize that molecule very precisely. By fitting the single molecule emission to a two-dimensional Gaussian function, localization precisions under 10nm can be achieved

with sufficient collection of photons (71). In conventional fluorescence imaging, biological samples are often densely labeled. Fluorescence emission from individual fluorophores overlaps spatially due to diffraction, and single molecule localization cannot be performed. The localization microscopy approach relies on photo-conversion of fluorophores between fluorescent and non-fluorescent states to achieve a sparse distribution of probes, i.e. separation by a distance greater than the Abbe limit, for independent localization with high precision. After one subset of fluorophores is imaged, those probes are converted to a non-fluorescent state and another subset is activated and imaged. Image reconstruction sums all probe locations collected during many photo-conversion cycles and results in a spatial map of fluorophores with resolution in the tens of nanometers. Fig. 1.2 shows a schematic demonstrating super-resolution image data collection and rendering.

The implementation of super-resolution localization techniques was enabled by the development of photo-convertible probes including photo-activatable and photo-switchable proteins (72–74) that are used for labeling in PALM/FPALM, and photo-convertible organic dyes (75, 76) that are used for STORM/dSTORM. Manipulation of these fluorophores with illumination and buffer conditions yields control over their fluorescent state. This allows the imaging of single molecules to be separated in time, which is the underlying technical advance that has made super-resolution localization microscopy possible.

In recent years the field has witnessed a rapid expansion of the functionality and application of localization microscopy. As the library of available photo-convertible probes increases, multi-color super resolution localization microscopy is becoming

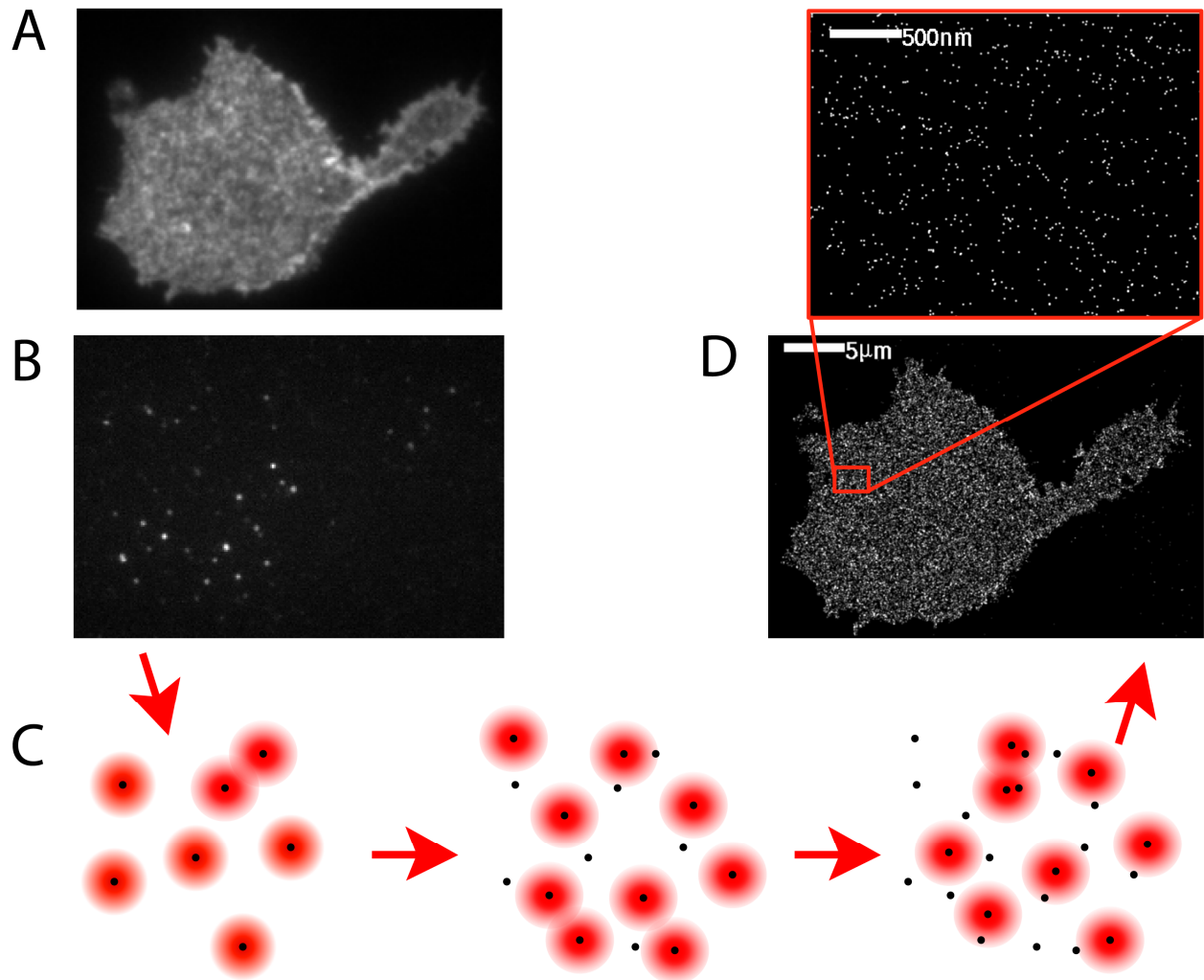


Fig. 1.2 Schematic of super-resolution localization microscopy image rendering. In a typical TIRF image, single molecule PSFs overlap and single molecules are indistinguishable (A). Following probe photo-conversion, only a subset of probes remains fluorescent (B). Individual probes are fit with a 2D Gaussian function and their positions are precisely determined. Through many photo-conversion cycles, probe positions are accumulated (C). Probe positions are summed to render a high-resolution image (D),

increasingly common through sample labeling with multiple photo-convertible fluorophores, facilitating experiments that characterize molecular interactions between or relative organization of several labeled species (77–80). Additionally, imaging conditions have also been optimized to allow for super resolution localization imaging of live cells, and improvements in time resolution have made the technique capable of capturing dynamic cell processes (81–83).

3.2. Measuring mobility with localization microscopy techniques

In live cells, probe blinking can also be exploited for use in single particle tracking (SPT) of molecules of interest (83–86). Traditional SPT is an excellent tool for measuring the diffusion behavior of molecules, but typically these recordings must be performed at low probe densities that prevent characterization of the spatial organization of molecules. Super-resolution localization microscopy relies on photo-conversion instead of sparse labeling to achieve low probe densities suitable for localization and tracking. Samples are densely labeled, and through controlled photo-conversion of probes, a high density of trajectories can be measured from a given sample. This not only enables measurement of a large population of diffusers, but also provides a means to correlate diffusion behavior of individual probes with the spatial structure of the sample. Single particle tracking can measure the diffusion rate of molecules of interest and can detect anomalous diffusion modes that may reflect interactions of the diffusers with their environment. In the context of the cell membrane, these could include transient pinning of membrane proteins, confinement by the actin cytoskeleton, or other protein-protein or protein-lipid interactions.

3.3. Quantitative analysis of protein distributions

In addition to SPT, quantification of the distribution of proteins through statistical analysis of the spatial map of localizations generated in a super resolution experiment is a robust tool for characterizing molecular interactions. This analysis has proven useful in the characterization of clustering and organization in super-resolution images of proteins associated with the cell membrane (87–91). In particular, pair-correlation analysis is a numerical method for extracting the average relative proximity of particles in a static image. It has been used to report the physical properties of membrane protein clusters, such as their average size and density, through the calculation of the correlation function $g(r)$ (53, 87, 88). The correlation function is sensitive to subtle inhomogeneity in the distributions of proteins, and is a robust tool for detection of even weak clustering. In two-color experiments, pair cross-correlations can be used to measure co-localization of two separate species labeled with different fluorophores, allowing for measurement of interactions between membrane components (86–88, 92, 93).

3.4. Potential artifacts

While the capability of super-resolution localization microscopy is promising, it is important to recognize the possible contribution of imaging artifacts in super-resolution data. As this still burgeoning technology is becoming more widely adopted, quantitative analysis of super resolution data should be subject to careful interpretation. In particular, individual probe localizations cannot be interpreted as unique, individually labeled

species. Proteins of interest can be “over-counted” due to multiple labeling by primary and secondary antibodies, conjugation of multiple fluorophores to a single labeled species, or reversible probe photo-conversion (87). As a result, individual proteins can appear in images as small clusters, leading to spurious interpretation. However, pair-correlation analysis can be used as a tool to distinguish the true distribution of a protein of interest from over-counting artifacts. In two-color super resolution experiments, pair cross-correlations are insensitive to the effects of over-counting molecules in individual color channels. As a consequence, cross-correlations can accurately report properties of co-clusters comprised of two membrane species without the need for over-counting correction (87). However, channel cross-talk can result in artifactually high cross-correlations, and so proper probe choice and the necessary controls are required for multi-color imaging (92, 94).

3.5. Localization imaging of cell membrane components

Super-resolution localization techniques are well-suited for studies of cell membrane proteins and lipids, where they have been used to provide information about the spatial organization and diffusion behavior of molecules within the context of the heterogeneous structure of the membrane. Nanoscale clustering of membrane proteins involved in a wide array of cell functions, from cell adhesion (69, 82, 95), to viral entry (84, 96), to chemotaxis (97) have been characterized. These studies have also examined clustering of proteins involved in processes mediated by membrane heterogeneity and immune receptor signaling in particular. For example, clustering and diffusion of the raft-associated protein hemagglutinin A (HA) has been characterized and

shown to be dependent on the actin cytoskeleton (86, 90). Several groups have examined clustering of proteins involved in T cell receptor signaling, a process that is closely related to the FcεRI signaling cascade. The clustering behaviors of T cell receptor (TCR), the tyrosine kinase Zap70, and the adaptor protein LAT were measured before and after receptor activation and shown to be dependent on the actin cytoskeleton (91, 98, 99). Sherman et. al directly visualized interactions between TCR and downstream signaling proteins including Zap70, LAT, and another adapter protein SLP-76 using two-color localization imaging (93). The authors were able to visualize activation of LAT by Zap70, and showed dependence of LAT-SLP-76 co-cluster structure on actin polymerization. Together, these efforts are beginning to paint a more detailed picture of associations between membrane proteins and their interaction partners, and how these contacts may be influenced by factors such as lipid environment and the actin cytoskeleton.

4. Current Studies

This dissertation describes our efforts to use the tools of super-resolution localization microscopy to better understand the physical mechanisms by which IgE signaling is initiated by receptor cross-linking and propagated in the early stages of the pathway. For these experiments, we use rat basophilic leukemia 2H3 (RBL-2H3) cells as a model system for mast cells (100). With tools of super-resolution localization microscopy, we have characterized receptor clustering and immobilization in fine detail and have identified two distinct stages of clustering and immobilization behavior following stimulation with multivalent antigen. To probe the interactions of IgE receptors

with other membrane components more directly, we have used two-color super-resolution localization microscopy to measure the recruitment of Lyn kinase to clustered receptors.

Chapter Two describes our work to apply super-resolution fluorescence localization microscopy, exploiting its capabilities for both high resolution imaging and for single-molecule recording of receptor diffusion, to the IgE receptor system. With this technique, we monitor the dynamics of clustering and mobility changes of IgE receptors in live RBL-2H3 mast cells undergoing a stimulated immune response. We do this both by quantifying average properties of receptors and by examining the behavior of single molecules. We find that clustering and immobilization proceed in two distinct phases that we correlate with a downstream signaling response, namely Ca^{2+} mobilization. In addition, we explore how receptor mobility and organization are altered by perturbations, including reversal of receptor cross-linking with monovalent hapten and modulation of the cholesterol content of cell membranes.

We further extend these studies to a system where receptor cross-linking is more spatially controlled in experiments shown in Appendix A. We characterize changes in receptor diffusion and organization that occur when receptors are cross-linked with structurally-defined trivalent ligands. These ligands are based on a double-stranded DNA scaffold and have well-defined inter-DNP spacings.

To address the questions of how downstream signaling partners interact with clustered receptors and how these interactions may be temporally and spatially regulated by heterogeneous membrane structures, we have turned to two-color super-resolution microscopy. With the goal of elucidating the interactions that occur during the

first stages of signaling, we focus on Lyn kinase. Lyn is one of the first interaction partners for IgE receptors following receptor cross-linking, and this interaction has been shown biochemically to be regulated by membrane lipids and the actin cytoskeleton. In Chapter Three we describe the antigen-dependent co-localization of IgE receptors with Lyn. We find that Lyn/IgE co-localization is enhanced following treatment of cells with cytoskeleton-disrupting drugs including latrunculin and cytochalasin D. Enhanced recruitment is also observed for a minimal fluorescent construct that only retains the lipid anchorage of Lyn.

In sum, these studies demonstrate the capability of super-resolution microscopy to enable detailed characterization of membrane processes at biologically relevant length scales in the tens of nanometers. Our results have helped elucidate the structural interactions leading to controlled spatial assembly of activated receptors and specific partners at the plasma membrane during the earliest stages of signaling. These findings contribute to improved understanding of the IgE-FcεRI signaling system, immunoreceptor signaling, and membrane heterogeneity-mediated cell signaling in general.

REFERENCES

1. Gilfillan, A.M., S.J. Austin, and D.D. Metcalfe. 2011. Mast cell biology: introduction and overview. *Adv. Exp. Med. Biol.* 716: 2–12.
2. Stone, K.D., C. Prussin, and D.D. Metcalfe. 2010. IgE, mast cells, basophils, and eosinophils. *J. Allergy Clin. Immunol.* 125: S73–80.
3. Metcalfe, D.D., R.D. Peavy, and A.M. Gilfillan. 2009. Mechanisms of mast cell signaling in anaphylaxis. *J. Allergy Clin. Immunol.* 124: 639–646; quiz 647–648.
4. Ierna, M.X., H.E. Scales, K.L. Saunders, and C.E. Lawrence. 2008. Mast cell production of IL-4 and TNF may be required for protective and pathological responses in gastrointestinal helminth infection. *Mucosal Immunol.* 1: 147–155.
5. Center for Disease Control. 2003. CDC Fast Facts A-Z: Vital Health Statistics. .
6. Geha, R.S., H.H. Jabara, and S.R. Brodeur. 2003. The regulation of immunoglobulin E class-switch recombination. *Nat. Rev. Immunol.* 3: 721–732.
7. Kinet, J.P. 1999. The high-affinity IgE receptor (FcεRI): from physiology to pathology. *Annu. Rev. Immunol.* 17: 931–972.
8. Holowka, D., and B. Baird. 2001. FcεRI as a paradigm for a lipid raft-dependent receptor in hematopoietic cells. *Semin. Immunol.* 13: 99–105.
9. Hakimi, J., C. Seals, J.A. Kondas, L. Pettine, W. Danho, and J. Kochan. 1990. The alpha subunit of the human IgE receptor (FcεRI) is sufficient for high affinity IgE binding. *J. Biol. Chem.* 265: 22079–22081.
10. Cambier, J.C. 1995. Antigen and Fc receptor signaling. The awesome power of the immunoreceptor tyrosine-based activation motif (ITAM). *J. Immunol. Baltim. Md 1950.* 155: 3281–3285.
11. Siraganian, R.P., J. Zhang, K. Suzuki, and K. Sada. 2002. Protein tyrosine kinase Syk in mast cell signaling. *Mol. Immunol.* 38: 1229–1233.
12. Kurosaki, T., and Y. Baba. 2010. Ca²⁺ signaling and STIM1. *Prog. Biophys. Mol. Biol.* 103: 51–58.
13. Siraganian, R.P. 2003. Mast cell signal transduction from the high-affinity IgE receptor. *Curr. Opin. Immunol.* 15: 639–646.
14. Blank, U., and J. Rivera. 2004. The ins and outs of IgE-dependent mast-cell exocytosis. *Trends Immunol.* 25: 266–273.

15. Menon, A.K., D.A. Holowka, W.W. Webb, and B.A. Baird. 1986. Cross-linking of receptor-bound IgE to aggregates larger than dimers leads to rapid immobilization. *J. Cell Biol.* 102: 541–550.
16. Paar, J.M., N.T. Harris, D. Holowka, and B. Baird. 2002. Bivalent Ligands with Rigid Double-Stranded DNA Spacers Reveal Structural Constraints on Signaling by FcεRI. *J. Immunol.* 169: 856–864.
17. Sil, D., J.B. Lee, D. Luo, D. Holowka, and B. Baird. 2007. Trivalent ligands with rigid DNA spacers reveal structural requirements for IgE receptor signaling in RBL mast cells. *ACS Chem. Biol.* 2: 674–684.
18. Holowka, D., D. Sil, C. Torigoe, and B. Baird. 2007. Insights into immunoglobulin E receptor signaling from structurally defined ligands. *Immunol. Rev.* 217: 269–279.
19. Pierini, L., N.T. Harris, D. Holowka, and B. Baird. 1997. Evidence Supporting a Role for Microfilaments in Regulating the Coupling between Poorly Dissociable IgE–FcεRI Aggregates and Downstream Signaling Pathways. *Biochemistry.* 36: 7447–7456.
20. Menon, A.K., D.A. Holowka, W.W. Webb, and B.A. Baird. 1986. Clustering, mobility, and triggering activity of small oligomers of immunoglobulin E on rat basophilic leukemia cells. *J. Cell Biol.* 102: 534–540.
21. Andrews, N.L., J.R. Pfeiffer, A.M. Martinez, D.M. Haaland, R.W. Davis, T. Kawakami, J.M. Oliver, B.S. Wilson, and D.S. Lidke. 2009. Small, mobile FcεRI aggregates are signaling competent. *Immunity.* 31: 469–479.
22. Dietrich, C., L.A. Bagatolli, Z.N. Volovyk, N.L. Thompson, M. Levi, K. Jacobson, and E. Gratton. 2001. Lipid rafts reconstituted in model membranes. *Biophys. J.* 80: 1417–1428.
23. Baumgart, T., A.T. Hammond, P. Sengupta, S.T. Hess, D.A. Holowka, B.A. Baird, and W.W. Webb. 2007. Large-scale fluid/fluid phase separation of proteins and lipids in giant plasma membrane vesicles. *Proc. Natl. Acad. Sci. U. S. A.* 104: 3165–3170.
24. Simons, K., and E. Ikonen. 1997. Functional rafts in cell membranes. *Nature.* 387: 569–572.
25. Munro, S. 2003. Lipid Rafts: Elusive or Illusive? *Cell.* 115: 377–388.
26. Pike, L.J. 2006. Rafts defined: a report on the Keystone symposium on lipid rafts and cell function. *J. Lipid Res.* 47: 1597–1598.
27. Kusumi, A., and Y. Sako. 1996. Cell surface organization by the membrane skeleton. *Curr. Opin. Cell Biol.* 8: 566–574.

28. Fujiwara, T., K. Ritchie, H. Murakoshi, K. Jacobson, and A. Kusumi. 2002. Phospholipids undergo hop diffusion in compartmentalized cell membrane. *J. Cell Biol.* 157: 1071–1081.
29. Kusumi, A., and K. Suzuki. 2005. Toward understanding the dynamics of membrane-raft-based molecular interactions. *Biochim. Biophys. Acta BBA - Mol. Cell Res.* 1746: 234–251.
30. Harder, T., and K. Simons. 1999. Clusters of glycolipid and glycosylphosphatidylinositol-anchored proteins in lymphoid cells : accumulation of actin regulated by local tyrosine phosphorylation. *Eur. J. Immunol.* 29: 556–562.
31. Holowka, D., E. d. Sheets, and B. Baird. 2000. Interactions between FcεRI and lipid raft components are regulated by the actin cytoskeleton. *J. Cell Sci.* 113: 1009 – 1019.
32. Chichili, G.R., and W. Rodgers. 2009. Cytoskeleton–membrane interactions in membrane raft structure. *Cell. Mol. Life Sci.* 66: 2319–2328.
33. Goswami, D., K. Gowrishankar, S. Bilgrami, S. Ghosh, R. Raghupathy, R. Chadda, R. Vishwakarma, M. Rao, and S. Mayor. 2008. Nanoclusters of GPI-Anchored Proteins Are Formed by Cortical Actin-Driven Activity. *Cell.* 135: 1085–1097.
34. Plowman, S.J., C. Muncke, R.G. Parton, and J.F. Hancock. 2005. H-ras, K-ras, and inner plasma membrane raft proteins operate in nanoclusters with differential dependence on the actin cytoskeleton. *Proc. Natl. Acad. Sci. U. S. A.* 102: 15500–15505.
35. Kwik, J., S. Boyle, D. Fooksman, L. Margolis, M.P. Sheetz, and M. Edidin. 2003. Membrane cholesterol, lateral mobility, and the phosphatidylinositol 4,5-bisphosphate-dependent organization of cell actin. *Proc. Natl. Acad. Sci. U. S. A.* 100: 13964–13969.
36. Jin, L., A.C. Millard, J.P. Wuskell, X. Dong, D. Wu, H.A. Clark, and L.M. Loew. 2006. Characterization and application of a new optical probe for membrane lipid domains. *Biophys. J.* 90: 2563–2575.
37. Field, K.A., D. Holowka, and B. Baird. 1997. Compartmentalized Activation of the High Affinity Immunoglobulin E Receptor within Membrane Domains. *J. Biol. Chem.* 272: 4276 –4280.
38. Field, K.A., D. Holowka, and B. Baird. 1999. Structural Aspects of the Association of FcεRI with Detergent-resistant Membranes. *J. Biol. Chem.* 274: 1753 –1758.
39. Gosse, J.A., A. Wagenknecht-Wiesner, D. Holowka, and B. Baird. 2005. Transmembrane Sequences Are Determinants of Immunoreceptor Signaling. *J. Immunol.* 175: 2123 –2131.

40. Sheets, E.D., D. Holowka, and B. Baird. 1999. Membrane organization in immunoglobulin E receptor signaling. *Curr. Opin. Chem. Biol.* 3: 95–99.
41. Hammond, A.T., F.A. Heberle, T. Baumgart, D. Holowka, B. Baird, and G.W. Feigenson. 2005. Crosslinking a lipid raft component triggers liquid ordered-liquid disordered phase separation in model plasma membranes. *Proc. Natl. Acad. Sci. U. S. A.* 102: 6320–6325.
42. Pyenta, P.S., D. Holowka, and B. Baird. 2001. Cross-correlation analysis of inner-leaflet-anchored green fluorescent protein co-redistributed with IgE receptors and outer leaflet lipid raft components. *Biophys. J.* 80: 2120–2132.
43. Sheets, E.D., D. Holowka, and B. Baird. 1999. Critical Role for Cholesterol in Lyn-mediated Tyrosine Phosphorylation of Fc ϵ RI and Their Association with Detergent-resistant Membranes. *J. Cell Biol.* 145: 877–887.
44. Young, R.M., D. Holowka, and B. Baird. 2003. A Lipid Raft Environment Enhances Lyn Kinase Activity by Protecting the Active Site Tyrosine from Dephosphorylation. *J. Biol. Chem.* 278: 20746–20752.
45. Young, R.M., X. Zheng, D. Holowka, and B. Baird. 2005. Reconstitution of Regulated Phosphorylation of Fc ϵ RI by a Lipid Raft-excluded Protein-tyrosine Phosphatase. *J. Biol. Chem.* 280: 1230–1235.
46. Holowka, D., J.A. Gosse, A.T. Hammond, X. Han, P. Sengupta, N.L. Smith, A. Wagenknecht-Wiesner, M. Wu, R.M. Young, and B. Baird. 2005. Lipid segregation and IgE receptor signaling: A decade of progress. *Biochim. Biophys. Acta BBA - Mol. Cell Res.* 1746: 252–259.
47. Sohn, H.W., P. Tolar, and S.K. Pierce. 2008. Membrane heterogeneities in the formation of B cell receptor–Lyn kinase microclusters and the immune synapse. *J. Cell Biol.* 182: 367–379.
48. Wu, M., D. Holowka, H.G. Craighead, and B. Baird. 2004. Visualization of plasma membrane compartmentalization with patterned lipid bilayers. *Proc. Natl. Acad. Sci. U. S. A.* 101: 13798–13803.
49. Torres, A.J., L. Vasudevan, D. Holowka, and B.A. Baird. 2008. Focal adhesion proteins connect IgE receptors to the cytoskeleton as revealed by micropatterned ligand arrays. *Proc. Natl. Acad. Sci. U. S. A.* 105: 17238–17244.
50. Andrews, N.L., K.A. Lidke, J.R. Pfeiffer, A.R. Burns, B.S. Wilson, J.M. Oliver, and D.S. Lidke. 2008. Actin restricts Fc ϵ RI diffusion and facilitates antigen-induced receptor immobilisation. *Nat. Cell Biol.* 10: 955–963.
51. Frigeri, L., and J.R. Apgar. 1999. The Role of Actin Microfilaments in the Down-Regulation of the Degranulation Response in RBL-2H3 Mast Cells. *J. Immunol.* 162: 2243–2250.

52. Wilson, B.S., S.L. Steinberg, K. Liederman, J.R. Pfeiffer, Z. Surviladze, J. Zhang, L.E. Samelson, L. Yang, P.G. Kotula, and J.M. Oliver. 2004. Markers for Detergent-resistant Lipid Rafts Occupy Distinct and Dynamic Domains in Native Membranes. *Mol. Biol. Cell.* 15: 2580–2592.
53. Veatch, S.L., E.N. Chiang, P. Sengupta, D.A. Holowka, and B.A. Baird. 2012. Quantitative nanoscale analysis of IgE-Fc ϵ RI clustering and coupling to early signaling proteins. *J. Phys. Chem. B.* 116: 6923–6935.
54. Shelby, S.A., D. Holowka, B. Baird, and S.L. Veatch. 2013. Distinct stages of stimulated Fc ϵ RI receptor clustering and immobilization are identified through super-resolution imaging. *Biophys. J.* 105: 2343–2354.
55. Gidwani, A., H.A. Brown, D. Holowka, and B. Baird. 2003. Disruption of lipid order by short-chain ceramides correlates with inhibition of phospholipase D and downstream signaling by Fc ϵ RI. *J. Cell Sci.* 116: 3177–3187.
56. Gidwani, A., D. Holowka, and B. Baird. 2001. Fluorescence Anisotropy Measurements of Lipid Order in Plasma Membranes and Lipid Rafts from RBL-2H3 Mast Cells. *Biochemistry.* 40: 12422–12429.
57. Sengupta, P., D. Holowka, and B. Baird. 2007. Fluorescence Resonance Energy Transfer between Lipid Probes Detects Nanoscopic Heterogeneity in the Plasma Membrane of Live Cells. *Biophys. J.* 92: 3564–3574.
58. Ge, M., A. Gidwani, H.A. Brown, D. Holowka, B. Baird, and J.H. Freed. 2003. Ordered and Disordered Phases Coexist in Plasma Membrane Vesicles of RBL-2H3 Mast Cells. An ESR Study. *Biophys. J.* 85: 1278–1288.
59. Larson, D.R., J.A. Gosse, D.A. Holowka, B.A. Baird, and W.W. Webb. 2005. Temporally resolved interactions between antigen-stimulated IgE receptors and Lyn kinase on living cells. *J. Cell Biol.* 171: 527–536.
60. Kelly, C.V., B.A. Baird, and H.G. Craighead. 2011. An array of planar apertures for near-field fluorescence correlation spectroscopy. *Biophys. J.* 100: L34–36.
61. Kelly, C.V., D.L. Wakefield, D.A. Holowka, H.G. Craighead, and B.A. Baird. 2014. Near-field fluorescence cross-correlation spectroscopy on planar membranes. *ACS Nano.* 8: 7392–7404.
62. Feder, T.J., I. Brust-Mascher, J.P. Slattery, B. Baird, and W.W. Webb. 1996. Constrained diffusion or immobile fraction on cell surfaces: a new interpretation. *Biophys. J.* 70: 2767–2773.
63. Veatch, S.L., P. Cicuta, P. Sengupta, A. Honerkamp-Smith, D. Holowka, and B. Baird. 2008. Critical Fluctuations in Plasma Membrane Vesicles. *ACS Chem Biol.* 3: 287–293.

64. Machta, B.B., S. Papanikolaou, J.P. Sethna, and S.L. Veatch. 2011. Minimal Model of Plasma Membrane Heterogeneity Requires Coupling Cortical Actin to Criticality. *Biophys. J.* 100: 1668–1677.
65. Ehrig, J., E.P. Petrov, and P. Schwille. 2011. Near-critical fluctuations and cytoskeleton-assisted phase separation lead to subdiffusion in cell membranes. *Biophys. J.* 100: 80–89.
66. Honigsmann, A., S. Sadeghi, J. Keller, S.W. Hell, C. Eggeling, and R. Vink. 2014. A lipid bound actin meshwork organizes liquid phase separation in model membranes. *eLife.* 3.
67. Rust, M.J., M. Bates, and X. Zhuang. 2006. Stochastic optical reconstruction microscopy (STORM) provides sub-diffraction-limit image resolution. *Nat. Methods.* 3: 793–795.
68. Heilemann, M., S. van de Linde, M. Schüttelpeiz, R. Kasper, B. Seefeldt, A. Mukherjee, P. Tinnefeld, and M. Sauer. 2008. Subdiffraction-Resolution Fluorescence Imaging with Conventional Fluorescent Probes. *Angew. Chem. Int. Ed.* 47: 6172–6176.
69. Betzig, E., G.H. Patterson, R. Sougrat, O.W. Lindwasser, S. Olenych, J.S. Bonifacino, M.W. Davidson, J. Lippincott-Schwartz, and H.F. Hess. 2006. Imaging Intracellular Fluorescent Proteins at Nanometer Resolution. *Science.* 313: 1642 – 1645.
70. Hess, S.T., T.P.K. Girirajan, and M.D. Mason. 2006. Ultra-High Resolution Imaging by Fluorescence Photoactivation Localization Microscopy. *Biophys. J.* 91: 4258–4272.
71. Thompson, R.E., D.R. Larson, and W.W. Webb. 2002. Precise nanometer localization analysis for individual fluorescent probes. *Biophys. J.* 82: 2775–2783.
72. Patterson, G.H., and J. Lippincott-Schwartz. 2002. A photoactivatable GFP for selective photolabeling of proteins and cells. *Science.* 297: 1873–1877.
73. Habuchi, S., R. Ando, P. Dedecker, W. Verheijen, H. Mizuno, A. Miyawaki, and J. Hofkens. 2005. Reversible single-molecule photoswitching in the GFP-like fluorescent protein Dronpa. *Proc. Natl. Acad. Sci. U. S. A.* 102: 9511–9516.
74. Wiedenmann, J., S. Ivanchenko, F. Oswald, F. Schmitt, C. Röcker, A. Salih, K.-D. Spindler, and G.U. Nienhaus. 2004. EosFP, a fluorescent marker protein with UV-inducible green-to-red fluorescence conversion. *Proc. Natl. Acad. Sci. U. S. A.* 101: 15905–15910.
75. Heilemann, M., E. Margeat, R. Kasper, M. Sauer, and P. Tinnefeld. 2005. Carbocyanine dyes as efficient reversible single-molecule optical switch. *J. Am. Chem. Soc.* 127: 3801–3806.

76. Bates, M., T.R. Blosser, and X. Zhuang. 2005. Short-range spectroscopic ruler based on a single-molecule optical switch. *Phys. Rev. Lett.* 94: 108101.
77. Gunewardene, M.S., F.V. Subach, T.J. Gould, G.P. Penoncello, M.V. Gudheti, V.V. Verkhusha, and S.T. Hess. 2011. Superresolution imaging of multiple fluorescent proteins with highly overlapping emission spectra in living cells. *Biophys. J.* 101: 1522–1528.
78. Dempsey, G.T., J.C. Vaughan, K.H. Chen, M. Bates, and X. Zhuang. 2011. Evaluation of fluorophores for optimal performance in localization-based super-resolution imaging. *Nat. Methods.* 8: 1027–1036.
79. Wilmes, S., M. Staufienbiel, D. Liße, C.P. Richter, O. Beutel, K.B. Busch, S.T. Hess, and J. Piehler. 2012. Triple-Color Super-Resolution Imaging of Live Cells: Resolving Submicroscopic Receptor Organization in the Plasma Membrane. *Angew. Chem.* 124: 4952–4955.
80. Jungmann, R., M.S. Avendaño, J.B. Woehrstein, M. Dai, W.M. Shih, and P. Yin. 2014. Multiplexed 3D cellular super-resolution imaging with DNA-PAINT and Exchange-PAINT. *Nat. Methods.* 11: 313–318.
81. Jones, S.A., S.-H. Shim, J. He, and X. Zhuang. 2011. Fast, three-dimensional super-resolution imaging of live cells. *Nat. Methods.* 8: 499–508.
82. Shroff, H., C.G. Galbraith, J.A. Galbraith, and E. Betzig. 2008. Live-cell photoactivated localization microscopy of nanoscale adhesion dynamics. *Nat. Methods.* 5: 417–423.
83. Manley, S., J.M. Gillette, and J. Lippincott-Schwartz. 2010. Single-particle tracking photoactivated localization microscopy for mapping single-molecule dynamics. *Methods Enzymol.* 475: 109–120.
84. Manley, S., J.M. Gillette, G.H. Patterson, H. Shroff, H.F. Hess, E. Betzig, and J. Lippincott-Schwartz. 2008. High-density mapping of single-molecule trajectories with photoactivated localization microscopy. *Nat Meth.* 5: 155–157.
85. Giannone, G., E. Hosy, F. Levet, A. Constals, K. Schulze, A.I. Sobolevsky, M.P. Rosconi, E. Gouaux, R. Tampé, D. Choquet, and L. Cognet. 2010. Dynamic Superresolution Imaging of Endogenous Proteins on Living Cells at Ultra-High Density. *Biophys. J.* 99: 1303–1310.
86. Gudheti, M.V., N.M. Curthoys, T.J. Gould, D. Kim, M.S. Gunewardene, K.A. Gabor, J.A. Gosse, C.H. Kim, J. Zimmerberg, and S.T. Hess. 2013. Actin Mediates the Nanoscale Membrane Organization of the Clustered Membrane Protein Influenza Hemagglutinin. *Biophys. J.* 104: 2182–2192.

87. Veatch, S.L., B.B. Machta, S.A. Shelby, E.N. Chiang, D.A. Holowka, and B.A. Baird. 2012. Correlation functions quantify super-resolution images and estimate apparent clustering due to over-counting. *PLoS One*. 7: e31457.
88. Sengupta, P., T. Jovanovic-Taliman, D. Skoko, M. Renz, S.L. Veatch, and J. Lippincott-Schwartz. 2011. Probing protein heterogeneity in the plasma membrane using PALM and pair correlation analysis. *Nat. Methods*. 8: 969–975.
89. Owen, D.M., C. Rentero, J. Rossy, A. Magenau, D. Williamson, M. Rodriguez, and K. Gaus. 2010. PALM imaging and cluster analysis of protein heterogeneity at the cell surface. *J. Biophotonics*. 3: 446–454.
90. Hess, S.T., T.J. Gould, M.V. Gudheti, S.A. Maas, K.D. Mills, and J. Zimmerberg. 2007. Dynamic clustered distribution of hemagglutinin resolved at 40 nm in living cell membranes discriminates between raft theories. *Proc. Natl. Acad. Sci. U. S. A.* 104: 17370–17375.
91. Williamson, D.J., D.M. Owen, J. Rossy, A. Magenau, M. Wehrmann, J.J. Gooding, and K. Gaus. 2011. Pre-existing clusters of the adaptor Lat do not participate in early T cell signaling events. *Nat Immunol*. 12: 655–662.
92. Stone, M.B., and S.L. Veatch. 2014. Far-Red Organic Fluorophores Contain a Fluorescent Impurity. *ChemPhysChem*. 15: 2240–2246.
93. Sherman, E., V. Barr, S. Manley, G. Patterson, L. Balagopalan, I. Akpan, C.K. Regan, R.K. Merrill, C.L. Sommers, J. Lippincott-Schwartz, and L.E. Samelson. 2011. Functional Nanoscale Organization of Signaling Molecules Downstream of the T Cell Antigen Receptor. *Immunity*. 35: 705–720.
94. Kim, D., N.M. Curthoys, M.T. Parent, and S.T. Hess. 2013. Bleed-through correction for rendering and correlation analysis in multi-colour localization microscopy. *J. Opt.* 15: 094011.
95. Shroff, H., C.G. Galbraith, J.A. Galbraith, H. White, J. Gillette, S. Olenych, M.W. Davidson, and E. Betzig. 2007. Dual-color superresolution imaging of genetically expressed probes within individual adhesion complexes. *Proc. Natl. Acad. Sci.* 104: 20308–20313.
96. Lehmann, M., S. Rocha, B. Mangeat, F. Blanchet, H. Uji-i, J. Hofkens, and V. Piguet. 2011. Quantitative Multicolor Super-Resolution Microscopy Reveals Tetherin HIV-1 Interaction. *PLoS Pathog.* 7: e1002456.
97. Greenfield, D., A.L. McEvoy, H. Shroff, G.E. Crooks, N.S. Wingreen, E. Betzig, and J. Liphardt. 2009. Self-Organization of the Escherichia coli Chemotaxis Network Imaged with Super-Resolution Light Microscopy. *PLoS Biol.* 7.

98. Hsu, C.-J., and T. Baumgart. 2011. Spatial Association of Signaling Proteins and F-Actin Effects on Cluster Assembly Analyzed via Photoactivation Localization Microscopy in T Cells. *PLoS ONE*. 6.
99. Lillemeier, B.F., M.A. Mortelmaier, M.B. Forstner, J.B. Huppa, J.T. Groves, and M.M. Davis. 2010. TCR and Lat are expressed on separate protein islands on T cell membranes and concatenate during activation. *Nat Immunol*. 11: 90–96.
100. Seldin, D.C., S. Adelman, K.F. Austen, R.L. Stevens, A. Hein, J.P. Caulfield, and R.G. Woodbury. 1985. Homology of the rat basophilic leukemia cell and the rat mucosal mast cell. *Proc. Natl. Acad. Sci*. 82: 3871–3875.

CHAPTER TWO

DISTINCT STAGES OF STIMULATED FcεRI RECEPTOR CLUSTERING AND IMMOBILIZATION ARE IDENTIFIED THROUGH SUPER-RESOLUTION IMAGING¹

SUMMARY

Recent advances in fluorescence localization microscopy have enabled imaging of chemically fixed and living cells at 20nm lateral resolution. We apply this methodology to simultaneously record receptor organization and dynamics on the ventral surface of live RBL-2H3 mast cells undergoing antigen-mediated signaling. Cross-linking of IgE bound to FcεRI by multivalent antigen initiates mast cell activation, which leads to inflammatory responses physiologically. We quantify receptor organization and dynamics as cells are stimulated at room temperature (22°C). Within 2 min of antigen addition, receptor diffusion coefficients decrease by an order of magnitude, and single particle trajectories are confined. Within 5 min of antigen addition, receptors organize into clusters containing ~100 receptors with average radii of ~70nm. By comparing simultaneous measurements of clustering and mobility, we determine that there are two distinct stages of receptor clustering. In the first stage, which precedes stimulated Ca²⁺ mobilization, receptors slow dramatically but are not tightly clustered. In the second stage, receptors are tightly packed and confined. We

¹ Published as S. A. Shelby, D. Holowka, B. Baird and S. L. Veatch, *Distinct stages of stimulated FcεRI receptor clustering and immobilization are identified through super-resolution imaging*. Biophysical Journal , 2013. **105**(10): p. 2343-2354. Reprinted with permission.

find that stimulation-dependent changes in both receptor clustering and mobility can be reversed by displacing multivalent antigen with monovalent ligands, and can be modulated through enrichment or reduction in cellular cholesterol levels.

INTRODUCTION

Mast cell activation results in secretion of chemical mediators of inflammation from intracellular granules as part of the adaptive immune response, which is responsible for the symptoms of allergy. The first steps of this process occur at the plasma membrane, where antigen-specific immunoglobulin E (IgE) bound to its receptor, FcεRI, is cross-linked by soluble multivalent antigen (1, 2). Cross-linking of IgE-FcεRI causes signal initiation by phosphorylation of immunoreceptor tyrosine-based activation motifs on FcεRI β and γ₂ subunits by Lyn kinase. The resulting tyrosine phosphorylation leads to Ca²⁺ mobilization and cellular degranulation (1–3). Oligomerization has readily observable effects on the spatial distribution and diffusion behavior of IgE-FcεRI. Receptors are uniformly distributed and mobile on the membrane before activation. Stimulation with antigen causes clustering of IgE-FcεRI into punctate aggregates on the cell surface and a marked decrease in receptor mobility (4, 5).

Cross-linked IgE-FcεRI puncta can be visualized with conventional fluorescence microscopy. However, quantitative measurements of receptor cluster formation require sub-diffraction-limited spatial resolution, comparable to the dimensions of clusters. Previous work has used a variety of experimental approaches to characterize the dynamic, antigen-induced, nanoscale reorganization of FcεRI to understand this initiation step in signaling. Receptor distributions at high spatial resolution have been

studied with electron microscopy using immunogold labeling of IgE-FcεRI (6–8). Additionally, dynamics of IgE-FcεRI during the time course of activation have been captured by fluorescence photobleaching recovery (FPR) (5, 9, 10) and fluorescence correlation spectroscopy (FCS) (11). Single particle tracking (SPT) of individual receptors labeled with fluorescent dye- or quantum dot-conjugated IgE has characterized the motion of single proteins (12–14). To date, these approaches have either achieved high resolution spatial measurements in chemically fixed systems or measured receptor mobility in live cells using non-imaging methods or without nanoscale spatial resolution.

Advances in fluorescence microscopy now enable sub-diffraction imaging using photoconvertible fluorescent dyes. Super-resolution techniques, including (direct) stochastic optical reconstruction microscopy (STORM/dSTORM) (15, 16) and (fluorescence) photoactivation localization microscopy (PALM/FPALM) (17, 18), have been used in fixed cells to quantify membrane protein distributions and clustering in other systems (19–24). Super-resolution techniques in live cells capture high-resolution maps of protein distributions (25, 26) in addition to diffusion information from single molecule trajectories (27–29). Further, the use of localization microscopy for single particle tracking methods provides improved number statistics over traditional single particle tracking because the photoconversion process allows for sampling of an ensemble of receptors over the course of a single live cell measurement. The present work applies super-resolution fluorescence localization microscopy, exploiting its capabilities for both high resolution imaging and for single-molecule recording of receptor diffusion. With this technique, we monitor the kinetics of clustering and mobility

changes of IgE receptors in live RBL-2H3 mast cells undergoing a stimulated immune response. We do this both by quantifying average properties of receptors and by examining the behavior of single molecules. In addition, we explore how receptor mobility and diffusion are altered by perturbations, including reversal of receptor cross-linking with monovalent hapten and modulation of the cholesterol content of cell membranes.

MATERIALS AND METHODS

Chemicals and Reagents

Amine reactive AlexaFluors 647 and 532 (AF647 and AF532), Fluo-4-AM, and Tetraspeck .125 μm fluorescent nanospheres were purchased from Life Technologies (Carlsbad, CA). β -mercaptoethanol, reduced L-glutathione, methyl- β -cyclodextrin, cholesterol-complexed methyl- β -cyclodextrin, glucose oxidase, and catalase were purchased from Sigma (St. Louis, MO). AF532 and AF647 -IgE were prepared by conjugating purified mouse monoclonal anti-2,4-dinitrophenyl (DNP) IgE with AF532 or AF647, as previously described (11, 30). AF647-IgE was measured to have a dye:protein ratio of 2.2:1. Multivalent antigen, dinitrophenyl- conjugated BSA (DNP-BSA), with an average of 24 DNP molecules per BSA was prepared as described previously (31). Glutaraldehyde (25% stock) was purchased from Ted Pella (Redding, CA). Para-formaldehyde was purchased from Electron Microscopy Services (Hatfield, PA). Cell culture supplies including MEM, Trypsin-EDTA, and gentamicin sulfate were

purchased from (Life Technologies), and FBS was purchased from Atlanta Biologicals (Atlanta, GA). Cell culture dishes were purchased from MatTek (Ashland, MA).

Sample Preparation

Rat Basophilic Leukemia (RBL-2H3) cells were maintained with media containing MEM 20% FBS, 10 µg/ml gentamicin sulfate as described previously (30), then harvested using Trypsin-EDTA. MatTek Dishes were prepared with fiduciary markers by applying a dilute (1:1000 dilution in phosphate-buffered saline) solution of Tetraspeck fluorescent nanospheres to freshly oxygen plasma-cleaned wells for 15 minutes before rinsing three times with RBL-2H3 media. Cells were then plated sparsely in the dishes (0.1×10^6 /well) overnight at 37°C.

Fixed cell samples:

The cells were sensitized with either AF647-labeled IgE (1µg/ml) (for single-color experiments) or a mixture of AF647-labeled IgE and AF532-labeled IgE (1µg/ml total) (for two-color experiments) in HEPES-buffered media (80% MEM, 20% fetal bovine serum, 50mg/L gentamicin, and 20mM HEPES) for 1 to 2 hours at room temperature. Dishes containing cells were rinsed and incubated in media at 37°C for 5 minutes, rinsed again with warm PBS, treated with 1 µg/mL DNP-BSA in media (for 0,1,5, or 10 min) at 37°C, rinsed with warm PBS, and then chemically fixed (4% paraformaldehyde 0.1% glutaraldehyde in PBS) for 10 minutes at room temperature. Samples were then blocked with 2% fish gelatin, 2 mg/mL BSA in PBS for 10 minutes. For both single- and

two-color experiments, fixed samples were washed 3 or more times with PBS and once with buffer containing 100mM Tris, 10mM NaCl, and 10% w/w glucose before imaging.

Live cell samples:

The cells were sensitized with AF647-labeled IgE (1 μ g/ml) in HEPES-buffered media for 1 to 2 hours at room temperature. Dishes containing sensitized cells were rinsed first with media, then once with super-resolution imaging buffer (IB: 30mM Tris, 135mM NaCl, 5mM KCl, 1mM MgCl₂, 1.8mM CaCl₂, 55mM glucose, 500 μ g/mL glucose-oxidase, 40 μ g/mL catalase, and 50mM glutathione at pH 8) before imaging.

Super Resolution Imaging

Imaging Setup:

Single label fixed samples were imaged on an inverted microscope (Leica DM-IRB, Wetzlar, Germany) under TIRF illumination through a 1.42 numerical aperture (N.A.) 100X Leica objective lens with a 100mW 642nm diode-pumped solid state (DPSS) laser (Crystalaser, Reno, NV) which is attenuated with neutral density filters as needed for the illumination requirements of the experiment. Typical laser power used during super-resolution data collection was about 60mW at the sample. Two-color experiments on fixed cells were conducted on an inverted Olympus IX81-ZDC microscope with a cellTIRF module (Olympus America, Center Valley, PA) under TIRF illumination through a 1.45 N.A. 100X Olympus objective lens with either a variable power 75mW 642nm DPSS laser (Coherent, Santa Clara, CA) or a 150mW DPSS 532 laser (Cobolt, Stockholm, Sweden). In both instrument setups, images were recorded

with an Andor iXon 897 EM-CCD camera (Belfast, UK) using custom image acquisition code written in Matlab (The MathWorks, Natick, MA). Live cell samples were imaged on both microscopes. The camera field of view was cropped during imaging to include only a region of interest that encompasses the entire cell being imaged in order to reduce image file size and increase the camera frame rate. Camera frame rates were dependent on our exposure time of 10ms, camera settings, and the size of the cropped region of interest.

Fixed cell imaging

Cells were imaged in the presence of an oxygen-scavenging and reducing imaging buffer (100mM Tris, 10mM NaCl, 10% w/w glucose, 500 µg/mL glucose-oxidase, 40µg/mL catalase, and 1% β-mercaptoethanol at pH 8.5). After individual cells were located using relatively low power illumination, laser power was increased to induce AF647, or AF532 photo-switching. Movies of AF647, or AF532 photo-switching were acquired with 10ms exposure time at frame rates between 25 and 32 frames per second for at least 2500 frames.

Live cell imaging

Live cells were imaged at room temperature to limit the effects of receptor internalization during the imaging experiment. Imaging was performed in the presence of super-resolution imaging buffer (IB: 30mM Tris, 135mM NaCl, 5mM KCl, 1mM MgCl₂, 1.8mM CaCl₂, 55mM glucose, 500µg/mL glucose-oxidase, 40µg/mL catalase, and 50mM glutathione at pH 8). Live cells were imaged at room temperature with frame

exposure times of 10ms and frame rates between 25 and 32 fps for at least 5 minutes before addition of DNP₂₄-BSA at a final concentration of 1µg/ml and monitored as stimulation progressed for at least 10 minutes for data reported in Figs. 1-4, 2.1, and 2.8. In experiments where antigen was competed off of surface IgE using DNP aminocaproyl-L-tyrosine (DCT), a stimulating dose of 0.1µg/ml antigen was used, and DCT at a final concentration of 20 µM was added 7 minutes after antigen addition (Fig. 5). Cells were imaged for at least 10 minutes after the addition of DCT. In membrane cholesterol perturbation experiments (Figs. 2.13, 2.12, 2.13, 2.10, and 2.11), methyl-β-cyclodextrin (MβCD) or cholesterol-complexed methyl-β-cyclodextrin (MβCD+chol) was added at a final concentration of 10mM 5 min before the addition of either DNP-BSA at a final concentration of 0.1ug/ml or a blank addition of an equivalent volume of buffer in experiments where cells were not stimulated. In experiments when cholesterol perturbation is followed by stimulation with DNP-BSA, cells were imaged for an additional 5 minutes in the presence of MβCD or MβCD+chol before antigen was added at a final concentration of 0.1ug/ml. The cells were then imaged for at least 10 minutes following stimulation. In experiments where cells were not stimulated after cholesterol perturbation, they were imaged for at least 15 minutes after addition of MβCD or MβCD+chol.

Image Analysis

Super-resolution image reconstruction

Movies of AF647 or AF532 photoswitching were analyzed as described in (32). In brief, diffraction-limited spots are fit to a two-dimensional Gaussian function though least

squares fitting using the built-in Matlab function *fminfunc()*. Localized probes that are outliers in spot width, brightness, aspect ratio, and 2D gaussian fit quality are excluded from the reconstructed image. In fixed cell measurements, probes that are localized in the same position in sequential frames, within twice the average localization precision, are combined. For live cell experiments, single molecule trajectories are determined as described below and only the first localization positions are included in reconstructed images. The average number of localizations that are accepted after culling and grouping is 12 per 10ms frame. For all experiments reconstructed images are assembled by incrementing a pixel value once for each time a localized signal is identified at that location. These images are then convolved with a two-dimensional Gaussian for display purposes. Super-resolution images are reconstructed from varying numbers of individual frames of raw data. For example, fixed cell images are reconstructed from at least 2500 frames (~100 s of integrated imaging time) of raw data, amounting to a total of approximately 30,000 single localizations, whereas live cell images are reconstructed from between 500 and 2000 frames (~20 and 80 s integrated imaging time), amounting to between approximately 6,000 and 24,000. The localization precision was calculated from correlation functions as described in (32) and had typical values around 20nm for a given imaging experiment using AF647 as the super-resolution probe.

Correlation function analysis of super-resolution images

Receptor clustering in super-resolution images is analyzed using spatial auto- and cross-correlation functions. Correlation functions are calculated from reconstructed

images of localized fluorophores as described previously (32). Briefly, reconstructed images (I) are masked (M) to exclude contributions from cell edges, and autocorrelation functions are tabulated using fast Fourier transforms (FFTs) according to:

$$g(r) = 1/\rho^2 \times \text{FFT}^{-1}(|\text{FFT}(I)|^2) / \text{FFT}^{-1}(|\text{FFT}(M)|^2)$$

where ρ is the average density of localized signals within the masked region. The autocorrelation of the mask is included to properly account for boundary conditions. A Matlab function that tabulates $g(r)$ from images is included in Supplementary material in (32). Cross-correlation functions for fixed cell images are tabulated similarly from masked images from two distinct images I_1 and I_2 with average densities ρ_1 and ρ_2 according to:

$$c(r) = 1/(\rho_1 \rho_2) * \text{RE}(\text{FFT}^{-1}(\text{FFT}(I_1) \times \text{FFT}(I_2)^*)) / \text{FFT}^{-1}(|\text{FFT}(M)|^2)$$

where * denotes a complex conjugate and RE() indicates the real part. Auto-correlation functions from single color live cell images were quantified as described in the main text.

Correcting for over-counting in fixed cell images

Auto-correlation functions from single-color fixed cell images are subject to additional clustering due to over-counting of labeled proteins, and quantifications are corrected for possible over-counting as described previously (32) and summarized below. When over-counting is present in a super-resolution image, the measured auto-correlation as a function of distance r , $g_{\text{meas}}(r)$, has the form

$$g_{\text{meas}}(r) = [\delta(r)/\rho + g(r>0)] * g_{\text{PSF}}(r),$$

where here the terms in square brackets are the delta function present at $r = 0$ ($\delta(r)$) plus the auto-correlation arising from the real distribution of labeled protein centers at distances greater than $r = 0$ ($g(r>0)$). Both terms are convoluted (*) with the correlation function of the effective point spread function (PSF) of the measurement $g_{\text{PSF}}(r)$, as described in detail in (32)). ρ is the average density of labeled molecules in the analyzed area. If a Gaussian shape of the PSF is assumed, the equation becomes

$$g_{\text{meas}}(r) = \exp\{-r^2/4\sigma^2\}/(4\pi \sigma^2 \rho) + g(r>0) * g_{\text{PSF}}(r)$$

where the first term represents the contribution to $g_{\text{meas}}(r)$ of over-counting. g_{PSF} is estimated by comparing the auto-correlation of images reconstructed from all identified single molecule centers to those of images reconstructed from data grouped to account for localized single molecules within a threshold of twice the localization precision and are identified in sequential frames as described previously (32). g_{PSF} is then fit to a two-dimensional Gaussian function to determine σ , and we assume a surface density of the receptor to be 200 molecules/ μm^2 (33). The measured correlation function is then fit to the above equation to determine the correlation function due to the real distribution of labeled molecules. $g(r>0)$ is approximated by an exponential function, $1+A\exp(-r/\xi)$, and A and ξ are extracted as fit parameters.

Cross-correlation functions from two-color experiments do not contain additional contributions from over-counting and can be fit to a single filtered exponential function to extract clustering parameters. Measured cross-correlations are of the form:

$$g_{\text{meas}}(r) = g_{\text{PSF}}(r) * g(r>0)$$

where $g(r>0)$ represents the correlation function arising from the real distribution of labeled molecules at distances greater than $r = 0$ and $g_{\text{PSF}}(r)$ is a function that applies a

Gaussian filter with width proportional to the resolution of the image and represents the PSF of the measurement. $g(r>0)$ is well fit by a single exponential function, yielding

$$g_{\text{Fit}}(r) = g_{\text{PSF}}(r) * [1 + (A \exp(-r/\xi))]$$

where A and ξ are extracted as fit parameters.

Single particle tracking and diffusion analysis

Single receptor trajectories are generated from fluorophore locations recorded within a masked area in live cell experiments using a simple tracking algorithm, in which localized probes in successive frames are linked in a trajectory if a localization in one frame falls within some maximum distance (here, 400-500nm) of a localization in the previous frame. This maximum step size is chosen by examining the resultant step size distribution and ensuring that it follows a log normal distribution. If a probe localization in one frame could be linked to more than one localization in the previous frame, i.e. the tracks merge, then the merged tracks are terminated to avoid artifacts. Also, if a point cannot be linked to the previous frame, the algorithm will look back up to several time points (3) to compensate for fast blinking of fluorophores or single molecules lost in image processing. Similar results were obtained with more complicated tracking algorithms that perform global minimizations (34).

Mean squared displacement (MSD) as a function of time interval τ is calculated over all trajectories that persist longer than two frames from the positions as a function of time ($x(t)$ and $y(t)$). In general, the MSD in 2 dimensions is defined as

$$\text{MSD}(\tau) = \langle (x(t+\tau) - x(t))^2 \rangle + \langle (y(t+\tau) - y(t))^2 \rangle$$

where the angled brackets denote an average over all t . MSD curves are tabulated for individual trajectories, or over all segments acquired in a single cell over a specified time window (typically 500 frames). Diffusion coefficients for individual molecules are only reported if trajectories extend at least some minimum number of frames (typically 14). Short and long time diffusion coefficients are determined through a weighted linear least squares fitting routine in Matlab (lsqnonlin), where weights were the inverse standard error of the mean for each $\text{MSD}(\tau)$.

In Fig. 2.7D, we generate three dimensional histograms from single trajectory data by keeping track of the average diffusion coefficient (D_S) for single tracks, and the average density of receptors along each trajectory. The average density along the trajectory is determined by first reconstructing a super-resolution image from the first point of all trajectories localized within a 1000 frames (40 s) of acquired raw data. For Fig. 2.7D, this image had a pixel dimension of 20nm by 20nm, and after reconstruction the image was convolved with a Gaussian filter with half-width of 40nm. This intensity image is then normalized so that the total average surface density is maintained at $200/\mu\text{m}^2$. Finally, long trajectories were placed upon this image and the pixel value at each localized point along the trajectory was averaged. The three dimensional histogram was constructed by binning in both diffusion coefficient and average intensity. Histograms were filtered with a Gaussian function with half-width ≤ 1 bin in order to smooth contours.

Ca²⁺ mobilization measurements

RBL-2H3 cells were plated in 35mm dishes and allowed to adhere at 37 °C overnight. Cells were then sensitized with 1ug/ml unlabeled IgE for at least 2h at 37 °C prior to imaging. The cells were rinsed then labeled with the Ca^{2+} -sensitive dye Fluo-4-AM by incubating in 0.4 μg of dye in 1ml of BSS containing 1mg/ml BSA (BSS-BSA) for 10min at room temperature. Cells were rinsed again to remove excess dye and imaged immediately in either BSS-BSA or in imaging buffer (IB) used for super-resolution experiments at room temperature. Fluo-4 fluorescence intensity was imaged at 2 fps under 10x magnification. Samples were monitored as the cells were stimulated by addition of either 1 or 0.1 μM DNP-BSA 5 minutes after the start of imaging. To test the effects of cholesterol perturbation on cellular Ca^{2+} responses, M β CD or M β CD+chol was added to the dish 5 minutes after the start of imaging at a final concentration of 10mM and allowed to incubate for 5 minutes before cells were stimulated with 0.1 μM DNP-BSA as above. Fluo-4 intensity for each cell was determined by recording the average fluorescence intensity within a circle of radius 5 pixels (7.25 μm) from the localized cell center as a function of time. The time averaged fractional intensity is normalized to 1 for each cell prior to treatments, and signals from at least 500 cells are averaged to obtain the average intensity traces shown in Figs. 2.5, 7, and 2.2. Small reductions in average Fluo-4 intensity vs. time due to bleaching and/or dye leakage were corrected for by fitting any downward slope present in the average Fluo-4 intensity curve within the first five minutes of imaging, prior to stimulation or addition of perturbation. The average intensity curve for all time points is then normalized by this fit. For cumulative curves of Ca^{2+} mobilization initiation events, individual cells are defined

as having initiated a Ca^{2+} response if their intensity increases by a factor of 2.5 more than the average intensity of the cell prior to treatments.

Degranulation experiments

To test the effects of imaging buffer on RBL degranulation, cells were sensitized with unlabeled anti-DNP IgE at a final concentration of $1\mu\text{g}/\text{mL}$ and plated at a density of 0.5×10^6 cells per well in a 96-well plate overnight at 37°C . Adherent cells were washed in BSS-BSA and then washed into either BSS-BSA, live cell imaging buffer (IB) without a reducing agent or oxygen scavenging enzymes (135mM NaCl, 5mM KCl, 1mM MgCl_2 , 1.8mM CaCl_2 , 55mM glucose, 30mM Tris, at pH 8), or complete imaging buffer which includes reducing agents and oxygen scavenging enzymes (135mM NaCl, 5mM KCl, 1mM MgCl_2 , 1.8mM CaCl_2 , 55mM glucose, 30mM Tris, at pH 8 *with* $500\mu\text{g}/\text{mL}$ glucose-oxidase, $40\mu\text{g}/\text{mL}$ catalase, and 10, 50 or 100 mM glutathione or 10 mM β -mercaptoethanol at pH 8). After the addition of multivalent ligand DNP_{24} -BSA at $1\mu\text{g}/\text{ml}$ final concentration, the cells were incubated at 37°C for an hour, and the supernatants were taken from each well to assay the extent of β -hexosaminidase release from the cells as previously described (35). Stimulated degranulation is expressed as a percentage of the total cellular β -hexosaminidase activity present in cell lysates after solubilization in 0.1% Triton X-100.

To test the effects of cholesterol perturbations on RBL-2H3 degranulation, cells were plated and sensitized with unlabeled IgE in the same manner as above. After washing with BSS-BSA, cells were washed into BSS-BSA, complete IB, or complete IB containing 10mM $\text{M}\beta\text{CD}$ or $\text{M}\beta\text{CD}+\text{chol}$. Following a 5 min incubation, DNP-BSA was

added to some samples at .1ug/ml final concentration and the samples were incubated at 37°C for one hour. β -hexosaminidase released was assayed as above.

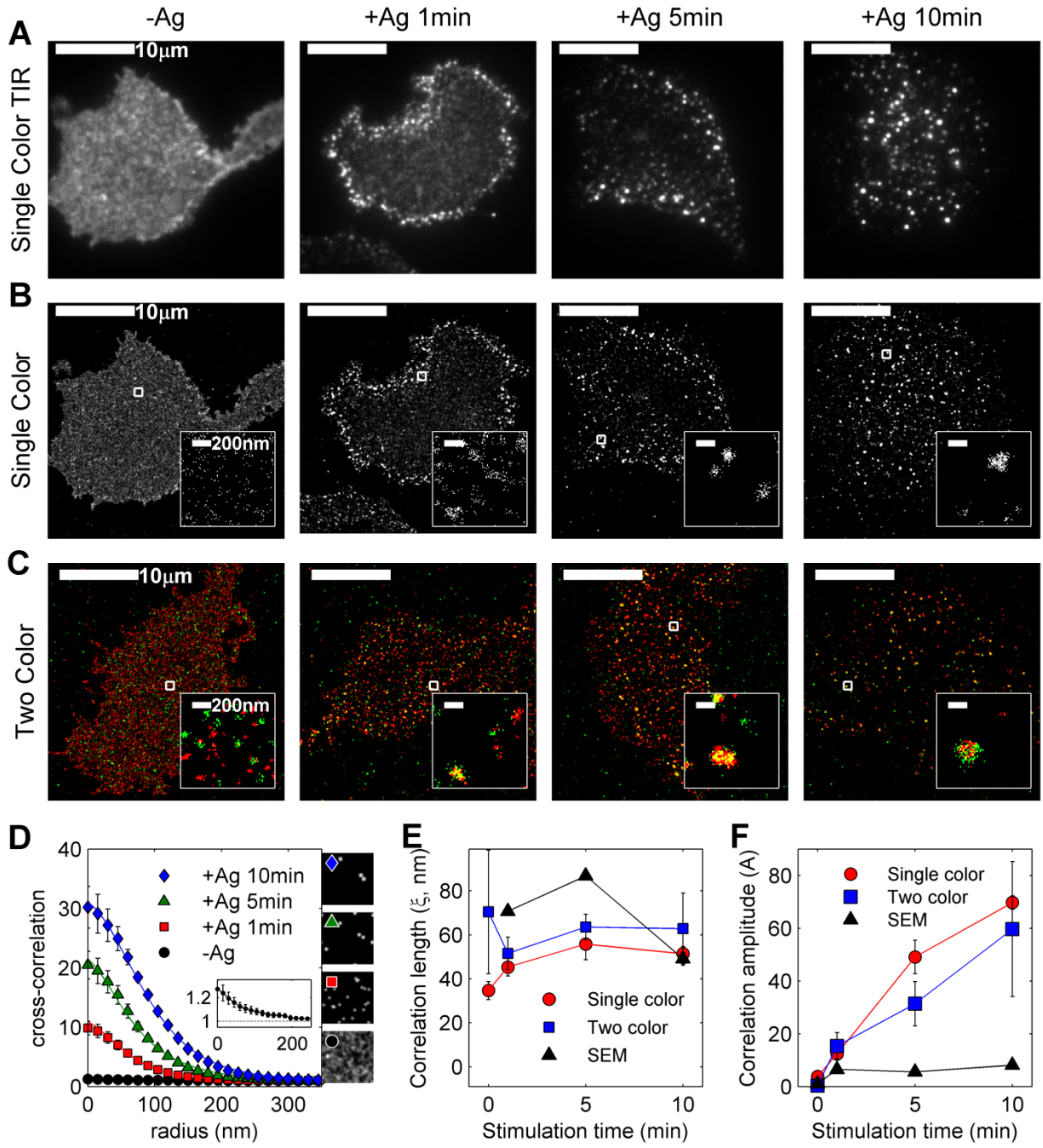
RESULTS AND DISCUSSION

Redistribution of IgE-Fc ϵ RI after antigen addition as imaged in chemically fixed cells.

Super-resolution fluorescence localization imaging of IgE-Fc ϵ RI at the ventral (bottom) surface of chemically fixed RBL-2H3 cells reveals time-dependent receptor clustering due to cross-linking by antigen (Fig. 2.1), in good agreement with previous electron microscopy studies (8). Cells were sensitized by incubating with IgE antibodies specific for DNP, stimulated with the multivalent antigen DNP-BSA, and then chemically fixed at specified time points after antigen addition, as described in Materials and Methods. IgE-Fc ϵ RI complexes were fluorescently labeled either by sensitizing with IgE directly conjugated to Alexa Fluor 647 (AF647) (Fig. 2.1 A and B), or by sensitizing cells with two distinct pools of IgE directly conjugated either to AF647 or to Alexa Fluor 532 (AF532) prior to antigen addition and fixation (Fig. 2.1 C). Conventional TIRF images of the single-color fixed cells (Fig. 2.1 A) were captured before single-color super-resolution images (Fig. 2.1 B) and are shown for comparison. For super-resolution images with both single- and two-color labeling, IgE-Fc ϵ RI appears weakly structured in unstimulated cells (-Ag) and exhibits a clustered appearance in cells after stimulation (+Ag). One minute after antigen addition, labeled IgE-Fc ϵ RI-rich patches become apparent around the periphery of the cell's ventral surface, likely because this is the

Fig. 2.1 Quantitative super-resolution localization microscopy TIRF imaging of IgE-FcεRI redistribution after antigen addition in chemically fixed cells.

Representative TIRF images of RBL-2H3 cells imaged using either (A) conventional TIRF microscopy, (B) single-color, or (C) two-color super-resolution fluorescence localization microscopy in unstimulated cells and cells treated with the multivalent antigen DNP-BSA (1 μg/ml) at 37°C for the time indicated before chemical fixation. Conventional TIRF and single color super-resolution images are shown for the same 4 cells in (A) and (B), respectively, for purposes of comparison between super-resolution and conventional images. Single-color cells in (A) and (B) are sensitized with IgE directly conjugated to AF647, while two-color measurements in (C) were conducted on cells sensitized with IgE directly conjugated to either AF647 (red) or AF532 (green) fluorophores. (D) Cross-correlation curves evaluated from two-color measurements averaged over at least 5 cells for each stimulation condition shown in (C). Error bars represent the standard error of the mean of values between cells. Lines are a fit to Eqn. 1 for radii between 0 and 500nm. Simulated receptor distributions over a 2μm by 2μm area which recapitulate observed correlation functions for each time point are shown at right. Extracted correlation lengths (E) and amplitudes (F) from super-resolution fluorescence localization imaging measurements are compared to previous scanning electron microscopy (SEM) measurements (8). Values reported for two-color measurements represent the average over multiple cells with error bounds denoting the standard error of the mean. For single-color measurements, values are obtained by correcting measured correlation functions for over-counting assuming a receptor density of 200/μm², and fitting the resulting curve to Eqn. 1 for radii between 40 and 300nm.



area accessed first by antigen. After incubation with antigen for 5 or 10 min, cells contain distinct IgE-FcεRI puncta on the ventral cell surface. Conventional TIRF imaging also shows large-scale receptor organization, including receptor puncta in stimulated cells, but structures under ~250nm cannot be resolved.

As with live cell experiments described below, we utilize spatial pair correlation functions to quantify clustering of IgE-FcεRI complexes in single-color reconstructed images of fixed cells. In single color experiments, multiple AF647 fluorophores can label each IgE antibody and each AF647 fluorophore can reversibly transition between fluorescent and non-fluorescent states within a single experiment. These phenomena result in apparent clustering on the size-scale of the localization precision in super-resolution images, such as those shown in Fig. 2.1 *B*, and corresponding artifacts in the quantification of images due to over-counting of single receptors (32). Pair cross-correlation functions are not subject to over-counting artifacts(32), are tabulated from two-color images, and measure the normalized probability of finding a localized fluorophore of one color a given distance, r , away from the average localized fluorophore of the second color. Average cross-correlation functions tabulated from unstimulated and stimulated cells are shown in Fig. 2.1 *D*.

Measured cross-correlation functions are fit to a single filtered exponential to extract information on average cluster size and density (32)

$$g_{\text{Fit}}(r) = g_{\text{PSF}}(r) * [1 + (A \exp(-r/\xi))]. \quad (1)$$

A is the amplitude of correlations, which is related to the increased density of receptors in clusters, ξ is the correlation length, which is approximately the average cluster radius, and $g_{\text{PSF}}(r)$ is a function that applies a Gaussian filter with width proportional to the

resolution of the image. Measured cross-correlation functions were fit for all radii $r < 500\text{nm}$. Details of the fitting methods and the determination of the resolution of the image are described in Materials and Methods. Simulated receptor density distributions which are reconstructed from our observed cross-correlation functions are shown in the right panels of Fig. 2.1 *D* and serve as a visual aid to represent receptor distributions in the absence of over-counting. We also fit autocorrelation functions tabulated from single color images to Eqn. 1 after first subtracting expected contributions from over-counting, assuming an average surface density of IgE-Fc ϵ RI complexes of $200/\mu\text{m}^2$ (32, 33). Summaries of extracted values for ξ and A from both single and two color images are shown in Fig. 2.1 *E* and *F* along with our past results applying a similar analytical methodology to scanning electron microscopy (SEM) images of IgE-Fc ϵ RI on the dorsal surface of RBL-2H3 cells labeled post fixation with primary and gold-conjugated secondary antibodies (8).

In unstimulated cells (-Ag), the cross-correlation of AF647 and AF532 probes is close to one at all radii, indicating that IgE-Fc ϵ RI complexes are nearly randomly distributed on the membrane (Fig. 2.1 *D*). Upon closer inspection, cross-correlation functions tabulated from images of cells indicate the presence of weak, long-range correlations in cells in the absence of antigen (inset of Fig. 2.1 *D*). The size of correlations in unstimulated cells is comparable to the size of clusters at long stimulation times, but the amplitude associated with these correlations is only 20% greater than a random distribution of receptors (Fig. 2.1 *D* inset), and two orders of magnitude less than the correlation amplitude 5 min following antigen stimulation. The simulated receptor distribution displayed in Fig. 2.1 *D* (lowest right panel) that corresponds to the

unstimulated correlation function is a visual representation of these weak correlations and is nearly indistinguishable from a random distribution. We previously proposed that weak, long-range, unstimulated clustering may arise from non-planar topology of the ventral membrane, from weak lipid-mediated organization in unstimulated cells (32), or through direct or indirect coupling to cortical actin (12, 36). We note that no equivalent correlations were observed in our previous SEM work in unstimulated cells, which selected for flat regions of the dorsal cell surface (8). Also, weak correlations are dominated by over-counting artifacts in autocorrelation functions tabulated from unstimulated cells labeled with a single color. Errors in the estimation of correlations from over-counting likely result in an underestimation of ξ and an over-estimation of A for single-color measurements.

Cross-correlation functions become larger than one at short radii in cells incubated with multivalent antigen prior to fixation, indicating that receptors become clustered. With increasing stimulation time, cross-correlations increase in magnitude at short radii. Cross-correlation functions, calculated from images of stimulated cells, remain larger than one out to radii of 200 nm, indicating that the largest clusters have approximately this radius. This quantitative treatment is consistent with the qualitative observation of clustering in representative images shown in Fig. 2.1, *B* and *C*. Variations in the size (ξ) and magnitude (A) of correlations as a function of stimulation time provide a quantitative measure of receptor redistribution with cross-linking. We observe a slight increase in the size of cross-linked receptor clusters (ξ) within 5 min after stimulation, similar to the modest increase we observe in live cells after stimulation (Fig. 1C). Values of ξ are in relatively good agreement with our past SEM data, which,

like our single-color experiments, are corrected for over-counting (Fig. 2.1 E) (8).

Observed differences between the dorsal cell surface imaged by SEM and the ventral cell surface imaged by super-resolution microscopy, could arise from different accessibility to antigen or differences arising from adhesion to the substrate.

The amplitude of correlations (A) also increases with stimulation time, corresponding to an increase in receptor density in clusters (Fig. 2.1 F). It is notable that the correlation amplitude is substantially larger in stimulated cells in super-resolution measurements when compared to our previous SEM studies (Fig. 2.1 F). This indicates that clustered fluorescent labels in these optical microscopy measurements are more densely packed than the gold particles observed by SEM. This could be accounted for if gold particles are precluded from labeling some IgE-Fc ϵ RI complexes in densely packed receptor clusters due to the large relative size of the primary and secondary antibodies and gold particles (10 nm diameter). Values of ξ and A extracted from single-color and two color images are in good general agreement aside from systematic reductions in ξ and elevation in A for single-color data. Again, these systematic errors are expected with underestimation of correlations due to over-counting in the single color measurements, since remaining contributions from over-counting would act to decrease ξ and increase A .

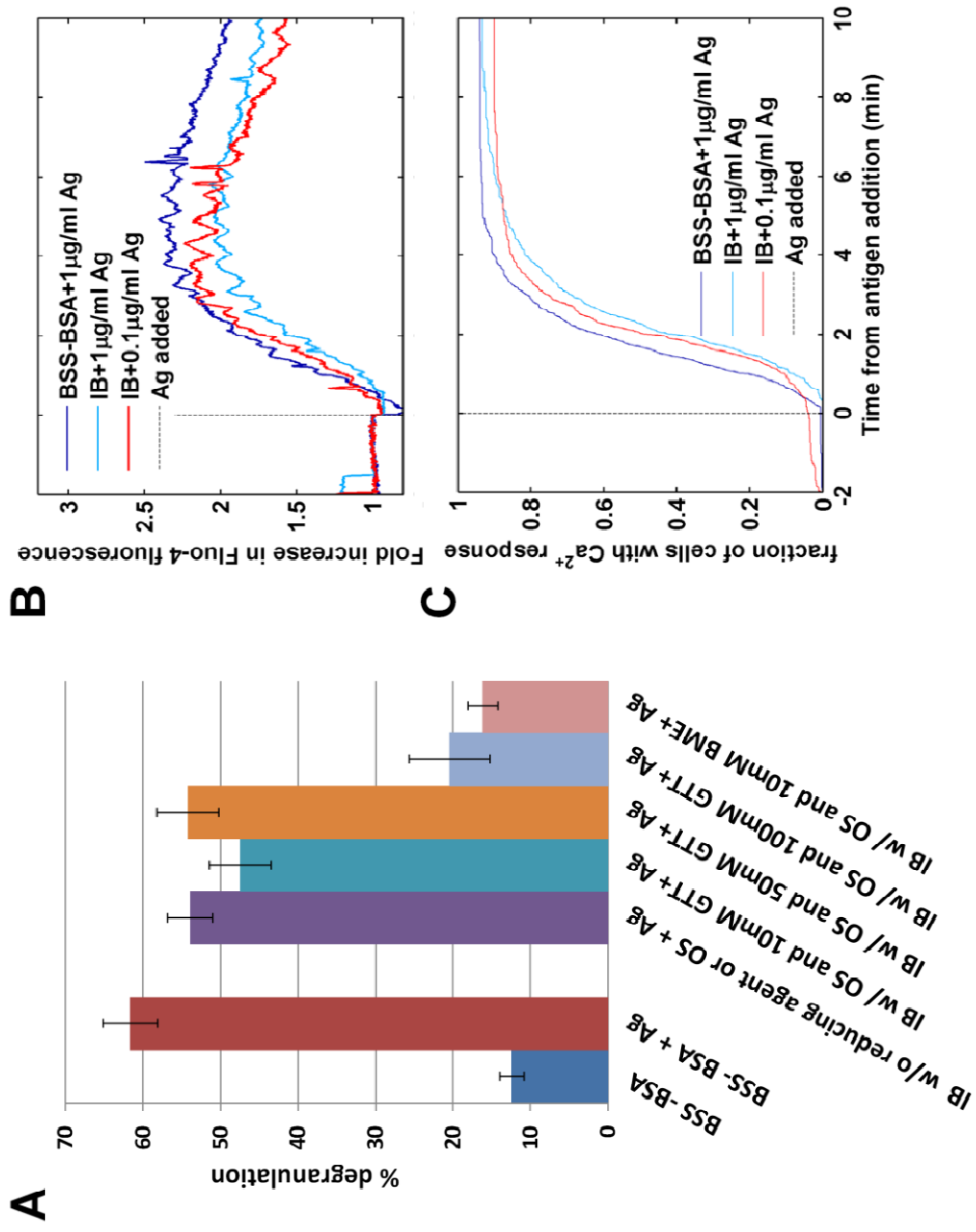
Live RBL-2H3 cells retain antigen-stimulated degranulation and Ca²⁺ responses under super-resolution imaging conditions.

To determine whether the buffer conditions required for dSTORM imaging affect the functional responses which result from IgE receptor cross-linking, a β -

hexosaminidase release assay was used to measure the levels of secretory granule release in adherent RBL-2H3 cells in response to antigen stimulation conditions similar to those used in our live cell super-resolution experiments. This assay utilizes a fluorogenic substrate for the enzyme β -hexosaminidase, a constituent of secretory granules, to measure its release as a consequence of degranulation and quantify the extent of degranulation in RBL-2H3 cells (35). Control samples were stimulated under conditions that are conducive to degranulation in balanced salt solution with 1 mg/ml BSA (BSS-BSA, 30mM HEPES, 135mM NaCl, 5mM KCl, 1mM MgCl₂, 1.8mM CaCl₂, 5mM glucose, and 1mg/ml BSA at pH 7.4) at 37°C. Our super-resolution imaging buffer is buffered with Tris and has a higher pH than BSS (pH 8), contains the reducing agents and oxygen scavenging enzymes necessary for dSTORM imaging of AlexaFluor 647, and also has a higher concentration of glucose (55mM), which is a substrate for the oxygen-scavenging enzyme glucose oxidase. To determine the effects of the various components of the imaging buffer on cellular degranulation, cells were stimulated in imaging buffer with or without 50mM of glutathione (GTT) and oxygen scavenging enzymes. These cells degranulate to a slightly lesser extent than cells stimulated in BSS-BSA (Fig. 2.2 A), although degranulation is still robust. Degranulation in the presence of this buffer is reduced to levels between 75 and 90% of degranulation measured in BSS-BSA according to data shown in Fig. 2.2 and Fig. 2.11. Cellular degranulation measured in cells in imaging buffer without a reducing agent or oxygen scavenging enzymes is not significantly different from degranulation of cells in imaging buffer that contains both 50mM glutathione and oxygen scavenging enzymes. The decreased degranulation of cells in imaging buffer that contains both 50mM glutathione

Fig. 2.2 RBL-2H3 cells retain the antigen-stimulated responses in super-resolution imaging buffer. (A) RBL-2H3 degranulation at 37°C was measured using a β -hexosaminidase release fluorogenic assay in which the effects of the oxygen scavenging enzymes (OS) and reducing agent used in the dSTORM imaging buffer (IB), including glutathione (GTT) or beta-mercaptoethanol (BME), were tested on antigen-stimulated degranulation. Cells in BSS-BSA in the presence or absence of DNP-BSA (1 μ g/ml) were used as standards for basal and stimulated degranulation, respectively. (B) Antigen-stimulated Ca^{2+} mobilization was measured in the presence of imaging buffer at room temperature using Fluo-4 intensity as a readout of intracellular Ca^{2+} concentration. Total fluorescence intensity is shown for populations of cells (at least 500) loaded with Fluo-4-AM and stimulated with 1 μ g/ml or 0.1 μ g/ml multivalent antigen (DNP₂₄-BSA) in BSS-BSA or in the presence of super-resolution imaging buffer as a function of time. The dotted gray line at 0 min indicates the addition of antigen. The signal is normalized to initial levels, and intensity is reported as a fold increase from initial levels. (C) Cumulative curves of Ca^{2+} mobilization initiation events of individual cells as a function of time. The number of cells which have initiated a Ca^{2+} response is plotted as the fraction of the total number of cells which displayed a Ca^{2+} response during the experiment.

Fig. 2.2



and oxygen scavenging enzymes compared to cells in BSS-BSA appears to be due to other components of the imaging buffer that differ from BSS-BSA, possibly the increased glucose concentration, Tris buffer, or increased pH. Stimulated cellular degranulation is substantially less when a higher concentration of glutathione is used or when β -mercaptoethanol is used as the imaging buffer reducing agent. For this reason a 50mM glutathione was chosen to minimize the impact of imaging buffer conditions on cellular responses, and the final formulation of the imaging buffer (IB) contains 30mM Tris, 135mM NaCl, 5mM KCl, 1mM MgCl₂, 1.8mM CaCl₂, 55mM glucose, 500 μ g/mL glucose-oxidase, 40 μ g/mL catalase, and 50mM glutathione at pH 8.

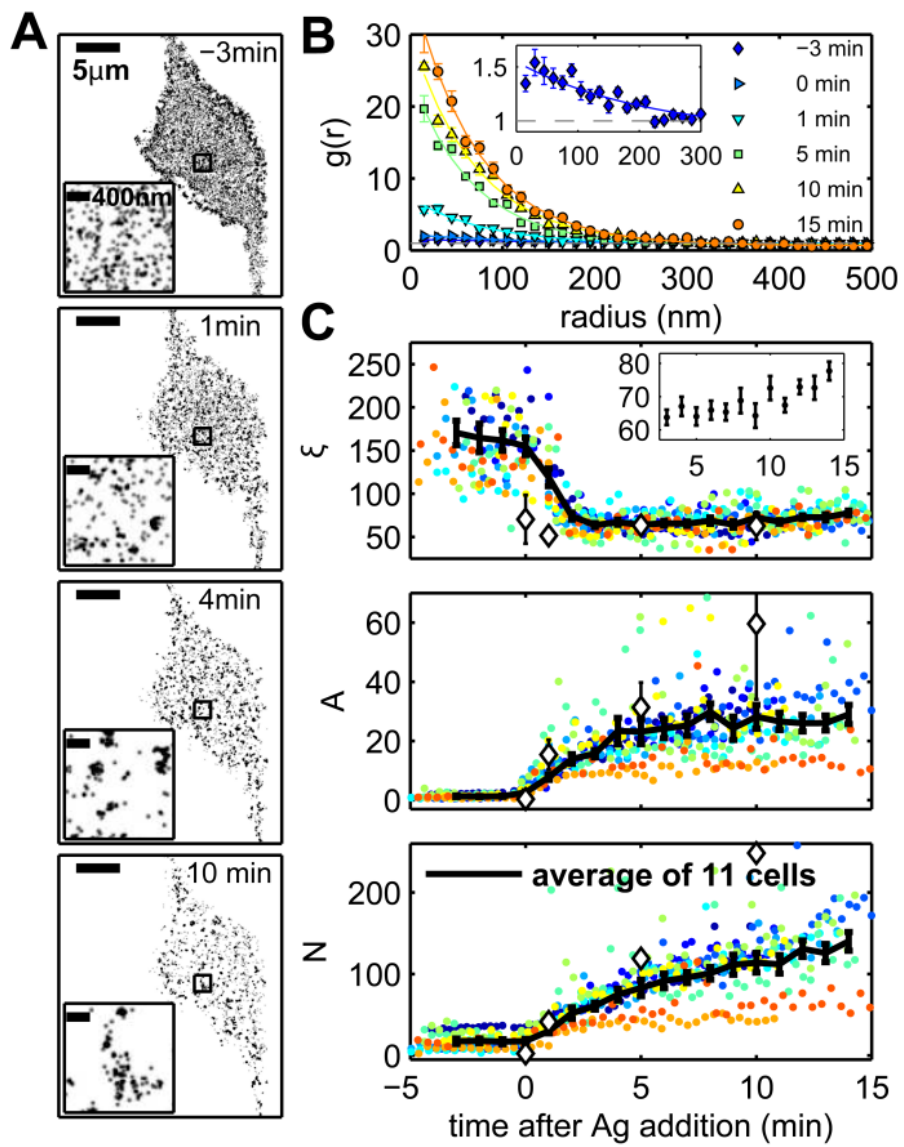
The effect of imaging buffer on Ca²⁺ mobilization was assessed through imaging experiments where sensitized RBL-2H3 cells are loaded with the Ca²⁺-sensitive dye Fluo-4 and stimulated with multivalent antigen (DNP-BSA) in the presence of imaging buffer at room temperature (Fig. 2.2, A and B). Fluorescence intensity is monitored across a field of several hundred cells as a function of stimulation time, as described in Materials and Methods. Cells produce a robust Ca²⁺ response in the presence of imaging buffer after stimulation by antigen compared to cells imaged and stimulated in the conventional live cell imaging buffer, BSS-BSA (Fig. 2.2 B). The cumulative distribution of cells with an initial Ca²⁺ response indicates that the onset of Ca²⁺ mobilization in the population of cells is not substantially delayed or otherwise affected by imaging buffer (Fig. 2.2 C).

Redistribution of IgE-Fc ϵ RI upon stimulation in live cells

Through super-resolution imaging of living cells, we simultaneously observe nanometer scale receptor organization and dynamics in real time. Fig. 1 A shows a representative live RBL cell that is imaged before and after the addition of multivalent antigen at room temperature under buffer conditions that both support super-resolution imaging and preserve downstream functional responses (Fig. 2.2). We chose to image at room temperature rather than 37°C because key signaling stages occur, although at a slower rate. These include receptor phosphorylation, Ca²⁺ mobilization, and endocytosis (11, 37). Cells were sensitized by incubation with IgE antibodies specific for dinitrophenyl (DNP) and stimulated with the multivalent antigen DNP-bovine serum albumin (DNP-BSA). IgE-FcεRI complexes were fluorescently labeled by sensitizing with IgE directly conjugated to an Alexa Fluor 647 (AF647), and imaged as described in Materials and Methods. Live cell images are produced by following single molecule trajectories in raw images, then reconstructing time averaged images using only the first localized position in each trajectory. Each reconstructed image in Fig. 2.3 A is compiled from 2000 raw image frames acquired over 68 s of imaging time at 31 frames per second. The relatively short imaging time produces a reconstructed image that is inherently under-sampled; only a fraction (estimated between 30 and 60 %) of individual IgE proteins are represented in each image. Despite this limitation, images clearly indicate that receptors are nearly randomly organized in unstimulated cells and become more clustered in response to cross-linking by multivalent antigen.

We utilize the spatial pair correlation function as a function of radius, $g(r)$, to quantify clustering of IgE-FcεRI complexes in reconstructed images. Pair auto-correlation functions measure the normalized probability of finding a second localized

Fig. 2.3 Quantitative super-resolution localization microscopy imaging of IgE-Fc ϵ RI redistribution after antigen addition in live cells. (A) Reconstructed super-resolution fluorescence localization images of an AF647-IgE-labeled living cell at various times in the stimulation sequence, where antigen (DNP-BSA, 1 μ g/ml) is added at 0 min. Each image is reconstructed from 68s of acquired data as described in Materials and Methods. Insets show magnified images of the regions outlined with black squares. A movie showing complete time-lapse imaging of this cell is supplied in the Supporting Material. (B) Auto-correlation functions, $g(r)$, are calculated from reconstructed single molecule centers acquired over 16s as described in Materials and Methods (solid shapes) and are fit to single exponentials (Eqn. 2; solid lines). The inset in (B) shows the correlation function from data recorded 3 min before antigen stimulation on an expanded scale. (C) Correlation function parameters from 11 live cell experiments, distinguished by different colors: the correlation length, ξ (top), the correlation amplitude, A (middle), and the average number of correlated proteins, N (bottom). Solid black lines indicate averages over 11 cells, and error bars represent standard error of the mean. The inset in (C, top) shows the average ξ for time points between 3 and 15 min after antigen addition on an expanded y axis scale. Fit parameters extracted from two-color fixed cell experiments are reproduced from Fig. 2.1, D and E and plotted for comparison in (C) as open black diamonds.



fluorophore a given distance, r , from the average localized fluorophore. These functions are tabulated as described previously (32) and summarized in Materials and Methods . For the resulting curves, a value of 1 indicates that receptors are randomly organized. Values greater than 1 indicate that receptors are clustered, and the range in r over which $g(r)$ is greater than 1 is a measure of cluster size. The $g(r)$ curves shown in Fig. 2.3 *B* were tabulated from images reconstructed using 500 frames of raw image data acquired over 16s. In agreement with visual observations, auto-correlation functions generated from time resolved images show that receptors are nearly randomly distributed prior to antigen addition, with $g(r)$ close to 1 at all radii, and become dramatically more densely clustered after stimulation. Correlation functions measured in live cells are in good quantitative agreement with those observed in cells chemically fixed at specific time-points after stimulation (Fig. 2.1). Although reconstructed images of live cells are undersampled compared to fixed cell images, as long as undersampling is random, its effects alone will not change the correlation function beyond decreasing signal to noise (32).

Measured auto-correlation functions are fit to a single exponential to extract information on average cluster size and density according to the equation:

$$g_{\text{Fit}}(r) = 1 + A \exp(-r/\xi) \quad (2)$$

for $r > 20$ nm, where A is the amplitude of correlations, which is proportional to the increased density of receptors in clusters, and ξ is the correlation length, which is approximately the average cluster radius. The average number of correlated proteins (N), or the number of correlated proteins within the average cluster, is the summation of

the measured $g(r)$ over r times the average surface density of receptors, defined by the equation:

$$N = \rho_{ave} \sum (2\pi r \Delta r (g(r)-1)), \quad (3)$$

where we assume that the overall average surface density of receptors (ρ_{ave}) is $200/\mu\text{m}^2$ (32, 33). When curves are well fit to the single exponential form given in Eqn. 2 in the limit of small Δr , this sum over values of r from zero to infinity can also be written as $N = \rho_{ave} 4 \pi A \xi^2$. In practice, we evaluate Eq. 2 for radii between 0 and 300nm, with $\Delta r = 15\text{nm}$.

This quantitative analysis, averaged over 11 cells, and a summary of extracted fit parameters is shown in Fig. 2.3 C. We observe dramatic redistribution of receptors into clusters after addition of multivalent antigen with weak, long-range correlations in unstimulated cells, and strong, shorter-range, correlations after antigen stimulation, consistent with previous reports in live cells (38). In unstimulated cells, we observe correlations with very low values of A and N and large values of ξ . This is further illustrated by the correlation function for unstimulated cells plotted in the inset of Fig. 2.3 B. ξ extends to almost 200nm in unstimulated live cells, whereas we observed $\xi \approx 80\text{nm}$ in chemically fixed cells (Fig. 2.1). The larger ξ observed in live cell images could arise from over-counting single molecules that are lost by our tracking algorithm, lateral motion of any correlated structures observed during data collection, or could be a consequence of live cells being imaged at room temperature whereas cells were chemically fixed after incubation at 37°C .

We observe time-dependent increases in A and N during the first 5 min following antigen addition. After this time, A remains constant, N continues to increase at a slower

rate, and ξ slowly increases (Fig. 2.3 C top, inset). The average ξ decreases within 3 min of antigen addition to about 70nm, in good agreement with ξ in stimulated fixed cells (Fig. 2.3 C, diamonds). The continuous decrease in ξ soon after antigen addition likely indicates the increasing presence of small and dense clusters in a background of larger more diffuse structure, as suggested by the image reconstructed from data acquired 1min after antigen addition in Fig. 2.3 A, although we do not attempt to resolve two distinct components in $g(r)$.

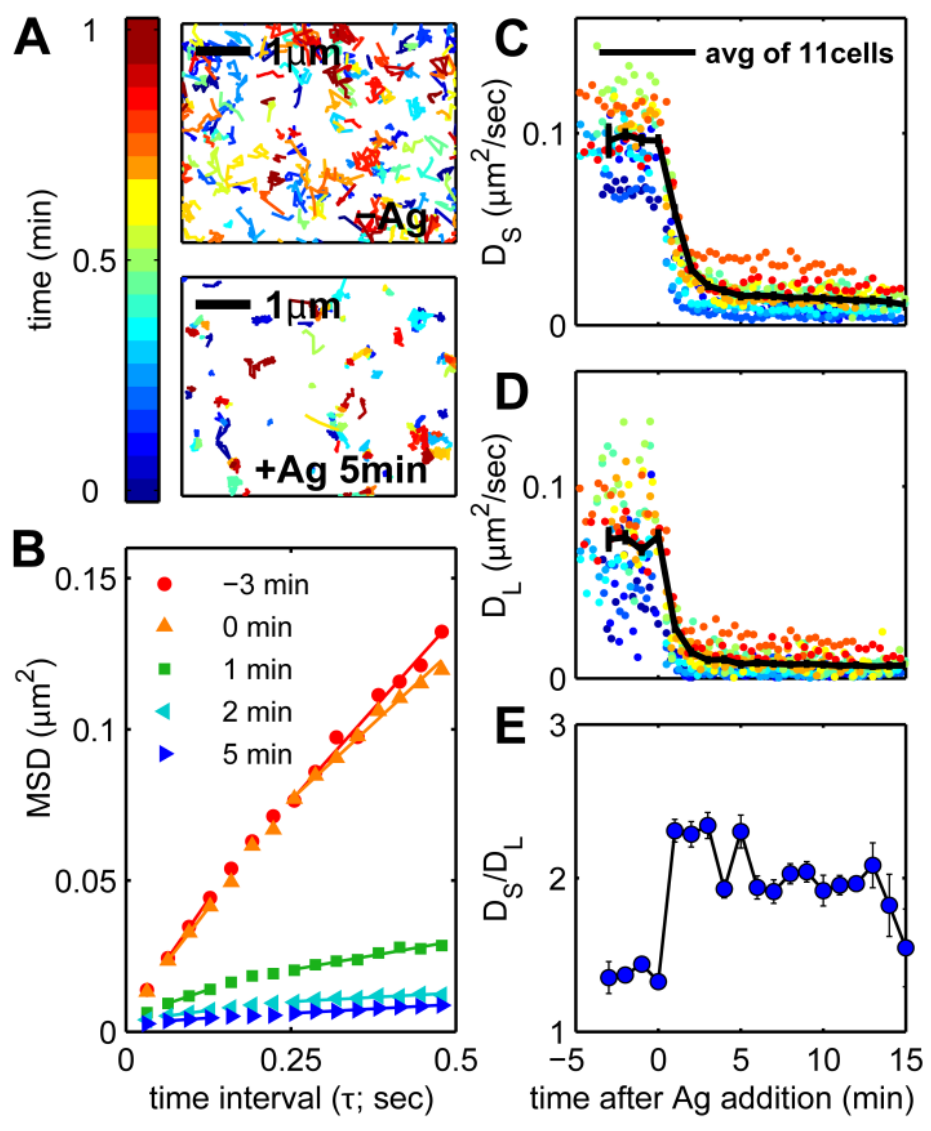
Our choice to quantify single color live cell images using auto-correlations relies on the assumption that live cell super-resolution images are not greatly affected by artifacts associated with over-counting single receptors. We expect this to be the case because individual fluorescently labeled receptors will typically diffuse over distances much larger than correlated structures with dimensions of several hundred nanometers or less during the time that a fluorescent molecule labeling an individual receptor remains in the dark state. This assumption may not be valid in stimulated cells, where receptors may become confined within densely cross-linked clusters, and the same receptor may be counted multiple times within a single cluster. If there is a contribution to correlation functions from over-counting, our reported results would lead to an overestimate of A . However, the values of A we observe from autocorrelation functions in live cells are systematically lower than values of A extracted from cross-correlation functions in fixed cells (Fig. 2.3 C black diamonds), which are not affected by over-counting artifacts. This supports the assumption that over-counting does not affect correlation functions throughout the time-course of imaging.

Our results using chemically fixed cells (Fig. 2.1) are consistent with and complementary to our live cell measurements in several regards. Agreement in A and N between fixed and live cells at early stimulation time points indicates that clustering occurs to approximately the same extent although at a somewhat slower rate in cells stimulated at room temperature vs. 37°C. Further, results from fixed cell experiments demonstrate that receptors are not clustered before stimulation. This result is important in the context of our live cell experiments because small and highly mobile clusters that diffuse much farther than their size over a typical image acquisition time would not be detected by our live cell quantification methods.

Mobility of IgE- FcεRI in live cell measurements.

The majority of individual fluorophores remain in a fluorescent state for multiple sequential frames, and we track these probes to form trajectories from localizations of the protein in time and space (see Materials and Methods). Visual inspection of trajectories obtained from 16 s of acquired data in unstimulated and stimulated cells suggests that IgE-FcεRI diffusion is relatively unconstrained prior to stimulation and that mobility decreases significantly after antigen addition (Fig. 2.4 A). Trajectories are quantified by tabulating the mean squared displacement (MSD) as a function of time interval (τ). Several representative curves are calculated by averaging MSD(τ) values over all trajectories acquired within 16s, as shown in Fig. 2.4 B. The magnitude of average MSD(τ) decreases after stimulation, indicating reduced receptor mobility. The representative data shown in Fig. 2.4, A and B, is acquired from the same cell shown in Fig. 2.3, A and B.

Fig. 2.4 Antigen stimulation leads to slower and more confined diffusion of IgE-Fc ϵ R1 receptor complexes. (A) Single molecule trajectories of IgE-Fc ϵ R1 complexes on the surface of cells under TIRF illumination before (-Ag) and after stimulation with 1 μ g/ml DNP-BSA for 5min (+Ag). Tracks shown are accumulated over 1min, only tracks observed for ≥ 5 frames (0.16s) are displayed, and coloring from blue to red indicates the relative time at which a single probe was observed within the 1 min time-frame. (B) Mean squared displacement (MSD) curves are generated by averaging over all tracks observed within a 500 frame (16s) time-period at the times during antigen stimulation indicated, as described in Materials and Methods. MSD curves are fit to Eqns. 4A and 4B to extract the short and long time diffusion coefficients D_S and D_L , respectively. (C,D) Summary of D_S (C) and D_L (D) extracted from MSD curves tabulated from single molecule trajectories acquired over 500 frames (approximately 20s and variable from cell to cell) for 11 distinct cells. Error bars represent standard error of the mean of the 11 live cell experiments. (E) Confinement as a function of stimulation time as measured by D_S/D_L from the same 11 live cell experiments. Error bars represent standard error of the mean.



In most cases we find that the slopes of $MSD(\tau)$ are not linear as expected for free diffusion, but instead are deflected to lower values at long τ , indicating that receptors are confined. We quantify both diffusion and confinement of IgE-Fc ϵ RI complexes as a function of stimulation time by fitting $MSD(\tau)$ to obtain both short and long time diffusion coefficients, D_S and D_L , which are obtained by fitting distinct time ranges of $MSD(\tau)$ curves to extract linear slopes. D_S is obtained by fitting the equation:

$$MSD(T_{2-4}) = 4D_S T_{2-4} + C_S, \quad (4A)$$

where T_{2-4} indicates the second, third, and fourth time intervals of the $MSD(\tau)$ curve, typically corresponding to roughly 50-100ms and C_S is the y-intercept of the fit that accounts for the finite localization precision of the single molecule data. D_L is obtained by fitting the MSD curve at time intervals between 250 and 500ms to the analogous equation:

$$MSD(T_{250-500ms}) = 4D_L T_{250-500ms} + C_L. \quad (4B)$$

Best fit lines to Eqns. 4A and 4B, whose slopes are proportional to the values of D_S and D_L , are shown for the representative $MSD(\tau)$ curves in Fig. 2.4 B. In addition, we quantify confinement by taking a ratio of these values, D_S/D_L . In the examples shown in Fig. 2.4 B, D_S/D_L is greater than 1, indicating that receptors are confined, and this ratio increases after antigen addition.

D_S , D_L , and their ratio for IgE-Fc ϵ RI in cells undergoing signaling responses are shown in Fig. 2.4, C-E, for the same 11 cells characterized in Fig. 2.3. Both D_S and D_L dramatically decrease within 5 min of antigen addition. After 5 min of stimulation, D_S decreases from 0.1 to 0.02 $\mu\text{m}^2/\text{s}$ and D_L decreases from 0.075 to 0.01 $\mu\text{m}^2/\text{s}$. We also observe changes in confinement with stimulation time as measured by D_S/D_L that

rapidly increases after stimulation before decreasing slightly at later stimulation time points.

Our measured values of D_S vs. stimulation time are in agreement with similar diffusion coefficient parameters measured previously using SPT (10, 12, 13, 38), FCS (11), and FPR (5, 9), ranging from 0.03 to 0.26 $\mu\text{m}^2/\text{s}$ before stimulation and 0.01 to 0.16 $\mu\text{m}^2/\text{s}$ after stimulation with a multivalent antigen. Previous measurements of receptor diffusion using SPT approaches similar to ours (10, 12, 13, 38) agree best with our observed values, where here reported values range from 0.07 to 0.1 $\mu\text{m}^2/\text{s}$ before stimulation and 0.01 to 0.05 $\mu\text{m}^2/\text{s}$ after. Our measurements of receptor confinement are also consistent with the observation of restricted or compartmentalized diffusion in previous SPT studies of Fc ϵ RI (10, 12, 38). In one of these past studies, the diffusion compartments of IgE-Fc ϵ RI were reported to shift to smaller sizes, together with a decrease in the diffusion coefficient for movement between compartments, upon antigen addition (38). This result is consistent with the antigen-induced increase in receptor confinement that we measure.

Correlating receptor mobility with receptor clustering

The data presented in Figs. 2.3 and 2.4 allow for direct comparison between changes in IgE-Fc ϵ RI receptor diffusion vs. spatial distribution. Taken together, the results indicate that IgE-Fc ϵ RI receptor complexes have decreased mobility (D_S , D_L) and increased confinement (D_S/D_L) that plateaus within 1-2 min after antigen addition. In contrast, the density of receptor clusters (A) increases more slowly, with amplitude of correlations plateauing after approximately 5 min (Fig. 2.3 C).

To explore more directly the relationship between cluster properties and receptor mobility, we plot in Fig. 2.5 A the average short time receptor diffusion coefficient D_S versus the average number of correlated proteins, N , for the stimulation time course averaged from 11 live cell experiments (average D_S and N as a function of time are shown independently in Figs. 2.4 C and 2.3 C, respectively). Interestingly, this representation suggests two distinct regimes of receptor mobility and clustering. In the first regime, D_S decreases dramatically without a large corresponding change in N . In the second regime, receptors become increasingly clustered without a large corresponding decrease in D_S . The cross-over between regimes occurs for N between 20 and 30, and D_S between 0.035 and 0.02 $\mu\text{m}^2/\text{s}$, which correspond to stimulation times between 1 and 1:45 min after antigen addition, respectively. For completeness, plots of A and Xi vs. D_S are also shown in Fig. 2.6.

Interestingly, the beginning of the cross-over between the two regimes shown in Fig. 2.5 A roughly coincides with the onset of Ca^{2+} signaling in RBL-2H3 cells imaged using the Ca^{2+} -sensitive dye Fluo-4 under nearly identical stimulation conditions (Fig. 2.5, B and C). Fluo-4 is loaded into sensitized RBL cells, and the fluorescence intensity is monitored across a field of several hundred cells as a function of stimulation time, as described in Materials and Methods. Soon after antigen addition, Fluo-4 intensity averaged over the population of cells begins rapidly increasing, with the bulk of the increase coming between 1 and 4 minutes (Fig. 2.5 B). There is a large cell-to-cell heterogeneity in the timing of the onset of the Ca^{2+} response, as indicated in the cumulative distribution shown in Fig. 2.5 C, with some cells initiating ~ 1 min after antigen addition under these imaging conditions. Approximately 50% of cells have

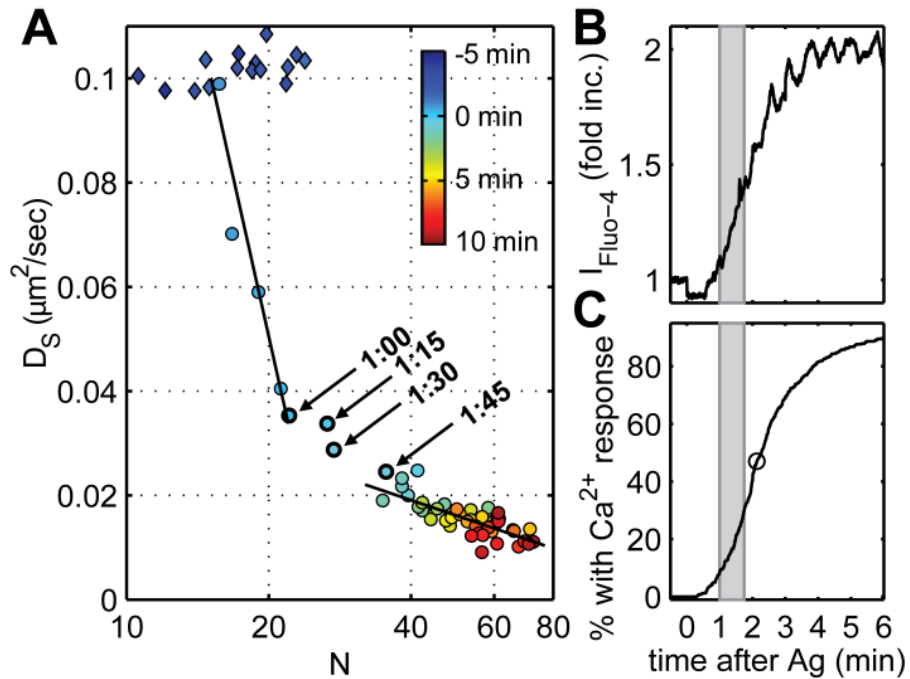


Fig. 2.5 Average receptor diffusion displays two different phases of dependence on the number of proteins in the average cluster. (A) Average D_S (as in Fig. 2.4 C) is shown as a function of average N from the same live cell experiments (as in Fig. 2.3 C). Each point corresponds to values of D_S and N at a given time before (diamonds) and after (circles) stimulation averaged over the 11 cells imaged, and data from individual cells are binned every 15 s to facilitate averaging. Time after the addition of antigen is indicated by the color bar. Antigen (1 $\mu\text{g/ml}$) is added after the cells were imaged for 5 min. The solid black lines represent linear fits of points between 0 and 1 min and between 1:45 and 15 min after antigen stimulation, weighted by the inverse of the standard error of the mean in D_S and N for each point. Points spanning these two regimes are indicated with arrows and labeled with the time after antigen addition. **(B)** Average intensity of the cytoplasmic Ca^{2+} indicator Fluo-4 over a population of cells imaged as described in Materials and Methods. The increase in Fluo-4 intensity after antigen stimulation indicates the onset of Ca^{2+} mobilization. The time period coinciding with the timing of the transition from the first regime to the second in A is highlighted by the shaded region. **(C)** The cumulative distribution of cells exhibiting an initial Ca^{2+} response indicates that the majority (>90%) of cells have initial Ca^{2+} responses between 1 and 4 min of antigen stimulation. The time point when 50% of the responding cells have exhibited a Ca^{2+} response is indicated by the open circle.

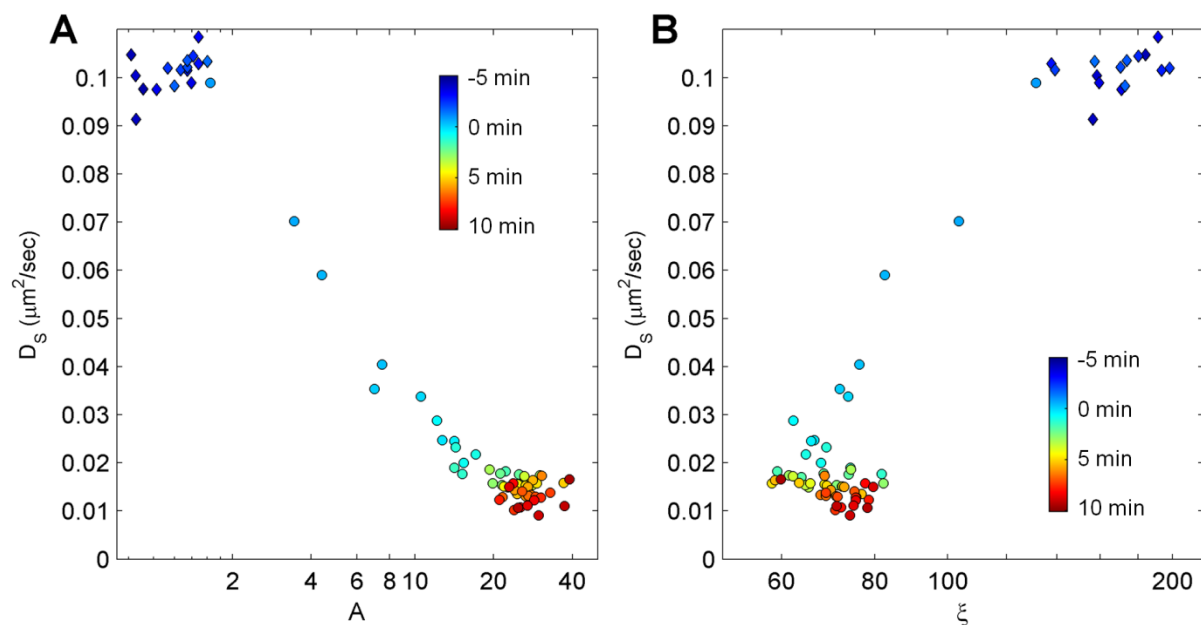


Fig. 2.6 Average receptor diffusion vs. correlation amplitude and correlation length. Average short time diffusion coefficient (as in Fig. 2.4 C) is shown as a function of the correlation function parameters, the correlation amplitude A (A) and the correlation length ξ (B) (as in Fig. 2.3 C). Each point corresponds to values of D_s and A or ξ at a given time before (diamonds) and after (circles) stimulation averaged over the 11 cells imaged, and data from individual cells are binned every 15 s to facilitate averaging. These plots are related to Fig. 2.5 A because the parameters N , A , and ξ are not independent. If correlation functions are well approximated by exponentials, then $N \approx 2A\xi^2\rho$, where ρ is the average receptor density which is assumed to be $200/\mu\text{m}^2$ (4). In Fig. 2.5 A, N is determined without fitting according to Eqn. 2. Time after the addition of antigen is indicated by the color bar. Antigen ($1 \mu\text{g}/\text{ml}$) is added at time = 0, after the cells were imaged for 5 min.

experienced a Ca^{2+} response within 2:15 min. Keeping in mind this large heterogeneity and the fact that we sample only a limited number of single cells in super-resolution experiments, we use the Ca^{2+} mobilization measurement as a rough indicator of the commencement of cellular signaling.

The results reported in Fig. 2.5 indicate that the initial, rapid decrease in D_S of IgE-Fc ϵ RI complexes is a consequence of interactions that precede Ca^{2+} mobilization, whereas the accumulation of receptors into densely packed clusters represents receptors after the onset of Ca^{2+} mobilization. This suggests that early signaling events which lead to the Ca^{2+} response do not require that receptors be densely clustered or fully immobilized. This interpretation of our results is consistent with previous studies that have reported that small IgE-Fc ϵ RI clusters that retain mobility can elicit a degranulation response (13), and that there is a high level of receptor tyrosine phosphorylation within the first few minutes of antigen stimulation, both at 37° and 15°C (39). In this past study (39), receptor tyrosine phosphorylation at 15°C occurs on a similar timescale as the Ca^{2+} response that we measure at room temperature, as we would expect since tyrosine phosphorylation precedes Ca^{2+} mobilization in the IgE receptor signaling cascade. This previous study also demonstrated that exposure of DNP haptens on the surface of DNP-BSA is transient, and that antigen binding is dominated by cross-linking of receptors after a minute of exposure to antigen(39). This is also consistent with the idea that the immobilization and Ca^{2+} responses we observe at early stimulation times occur concurrently with the formation of small clusters and that receptors become more heavily cross-linked at later times.

Because diffusion of cross-linked IgE-FcεRI decreases rapidly without a corresponding large increase in N, it likely occurs as a result of IgE-FcεRI coupling to downstream signaling partners. This could be due to receptor association with other freely diffusing membrane anchored proteins that are not labeled in these experiments. It is possible that receptor slowing is due to slower movement between corrals defined by cortical actin, either due to mechanical occlusion of the growing signaling platforms with actin anchored proteins (40, 41), or due to increased coupling of platforms to actin-stabilized, lipid-mediated heterogeneity (36). Alternatively, the reduced mobility of receptors at early signaling stages could be a consequence of direct or indirect tethering to an immobilized component such as actin. The actin cytoskeleton has been shown to be partially responsible for the immobilization of cross-linked IgE-FcεRI (12), and plays a role in the desensitization of receptors to antigen (42), and internalization (43). The increasing clustering of receptors that dominates later signaling stages could be a mechanism to down-regulate signaling by sequestering receptors, as occurs in B cell and T cell receptor activation (44–47). It is also possible that the observed receptor clusters represent an early stage of receptor internalization that has not progressed substantially under these conditions of stimulation time and temperature (11).

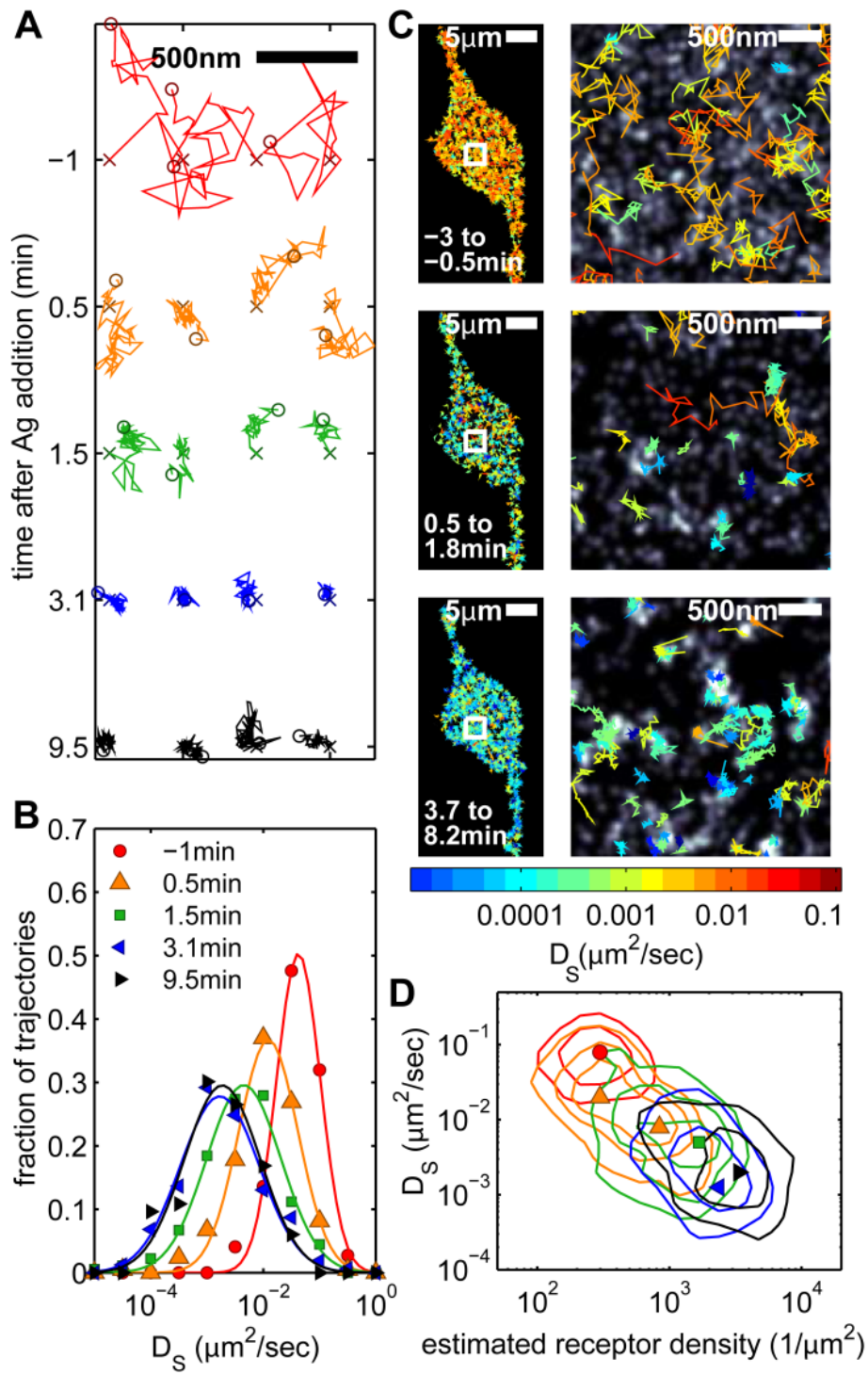
Ca²⁺ mobilization is used here as an approximate indication of the timing of the onset of cellular signaling, but consideration should be given to its direct comparison with super-resolution measurements. Clustering and immobilization of IgE receptors on the ventral surface of cells could begin more slowly than Ca²⁺ mobilization because the Ca²⁺ response may originate from receptors on the dorsal surface of cells, which are expected to be more accessible to antigen. This may lead to a time delay between the

initiation of the Ca^{2+} response and our observation via super-resolution measurements of immobilization and clustering. If this is the case, receptors on the dorsal surface may be somewhat more clustered at the onset of the Ca^{2+} response, but this would not change our conclusion that the first phase of clustering and immobilization occurs before Ca^{2+} mobilization, and the second phase occurs predominantly afterward. Ca^{2+} mobilization itself may be considered a downstream measure of the onset of signaling. Previous work has shown that receptor phosphorylation by Lyn kinase proceeds much more rapidly than Ca^{2+} mobilization (48), and thus Ca^{2+} mobilization represents membrane interactions that initiate a broader cellular response and occur subsequent to the initiation of signaling at the level of single receptors.

Single molecule analysis of receptor diffusion and clustering

Early and late signaling stages are also distinguished when receptors are examined as single molecules, and several representative trajectories are shown in Fig. 2.7 A. Single receptor trajectories in unstimulated cells traverse large areas. Soon after antigen is added, trajectories rapidly condense and some receptors appear to sample multiple confined areas in single trajectories, lasting approximately 1 s each. After a few minutes of antigen stimulation, trajectories are compact and appear highly confined. The ensemble of single molecule trajectories is quantified by assembling histograms of D_s . Fig. 2.7 B shows histograms assembled using 16 s of data acquired in a single cell, which are representative of histograms obtained from other cells examined. Histograms are well-described as single log-normal distributions for all time points, indicating that a single population of diffusers is resolved in these measurements. Distributions of D_s

Fig. 2.7 Slower and more confined diffusion of single receptors correlates with regions of high receptor density. (A) Example single molecule trajectories are shown from the same cell in Fig. 2.3, *A* and *B*, Fig. 2.4, *A* and *B*, and Fig. 2.7 *C* recorded before and after antigen stimulation. Tracks shown persist for at least 0.5 s for the -1 min (unstimulated) time point and 1 s for other time points. (B) Short time diffusion coefficients (D_S) are evaluated from MSD curves tabulated from single molecule trajectories lasting at least 0.5 s within a 16 s time-period, and are assembled into histograms. Histograms are normalized by the total number of tracks collected to generate each histogram (C) Single molecule trajectories persisting for at least 0.5 s are superimposed on a super-resolution images reconstructed from unstimulated data (top), from data acquired within 1min of antigen addition (middle), and data acquired after several minutes of stimulation. Track coloring indicates D_S for each track on a log scale from $10^{-5} \mu\text{m}^2/\text{s}$ (blue) to $1 \mu\text{m}^2/\text{s}$ (red). The inset on the right is an enlarged image of the boxed region at the left. (D) 3-dimensional histograms of D_S vs. average receptor density along trajectories lasting at least 0.5 s. Average receptor density for each trajectory is determined by averaging the pixelated grayscale values from the time-averaged reconstructed image over all positions of the trajectory and then normalizing assuming $\rho_{\text{ave}}=200/\mu\text{m}^2$, as described in the Materials and Methods.

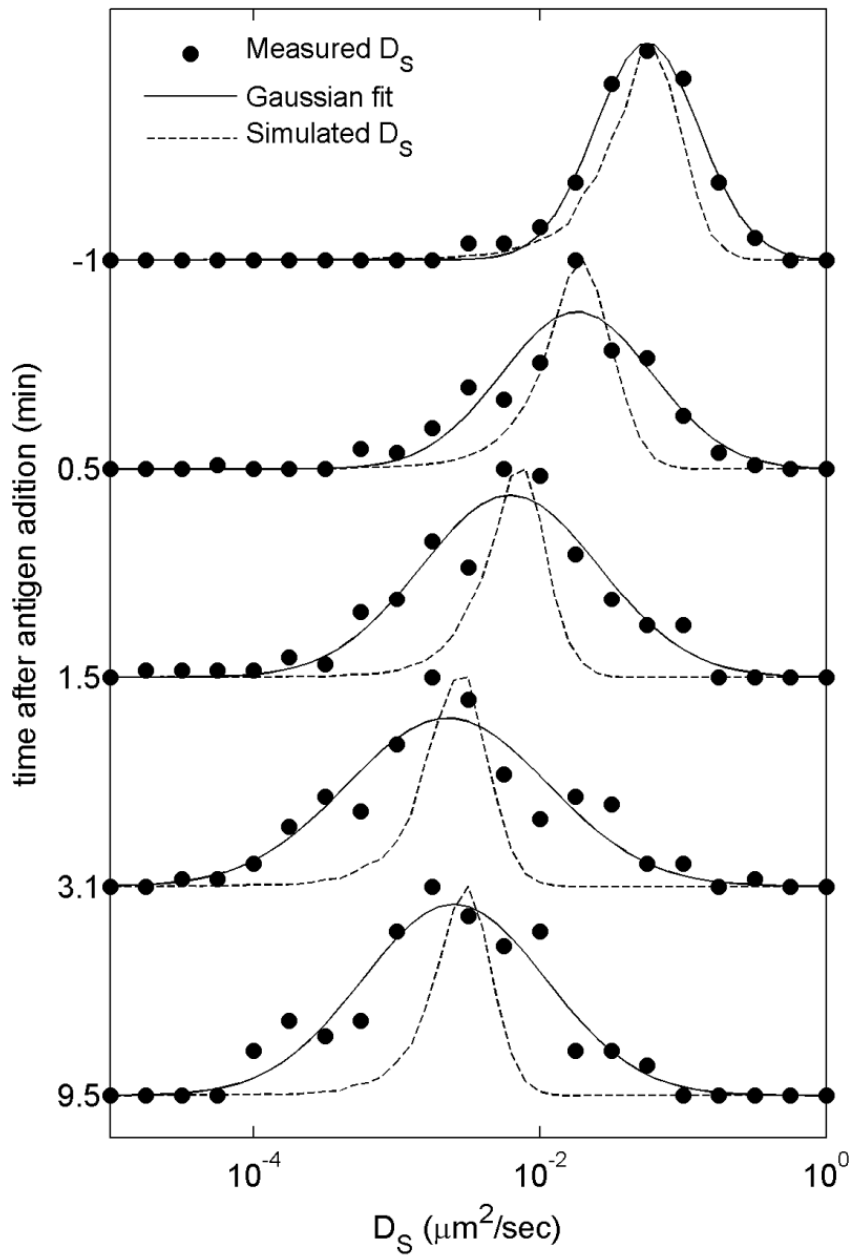


rapidly shift to lower values and broaden soon after antigen is added, stabilizing after 3 min of stimulation time. These distributions are broad, in part because diffusion coefficients are not well defined when obtained from short trajectories (49). To separate this effect from real heterogeneity, we compare measured distributions of D_S to those obtained by simulating Brownian trajectories with 16 frame (0.5 s) track-length (Fig. 2.8). In unstimulated cells, the width of measured D_S histograms is comparable those of simulated trajectories. In contrast, measured histograms for receptors after antigen addition are significantly broader than the simulated distributions, indicating that the membrane environment sampled by IgE-Fc ϵ RI is heterogeneous.

We also investigated how receptor diffusion correlates with the local surface density of receptors in reconstructed images. To accomplish this, we reconstructed super-resolution fluorescence images as described in Materials and Methods. Representative grayscale images for a single cell at various stimulation stages are shown in Fig. 2.7 C. In these images, pixel intensity is proportional to the observed receptor density, and trajectories that persist for greater than 0.5 s are superimposed onto this image. In the unstimulated cell (top panel of Fig. 2.7 C), individual receptors diffuse over large areas and their mobility is not visually correlated with roughly random receptor density. Soon after antigen addition (< 1 min), individual receptors appear more confined even though the spatial distribution of receptors remains largely random (middle panel). At longer times, (> 5 minutes after antigen addition), diffusing receptors are confined to regions where receptors are densely packed (bottom panel).

These visual observations are quantified by calculating the average pixel intensity over the length of single molecule trajectories persisting greater than 0.5 s.

Fig. 2.8 Distributions of single-trajectory diffusion constant are broader than expected for Brownian diffusion post-stimulation. Histograms showing the distribution of single molecule diffusion coefficients (D_S) are repeated from Fig. 2.7 *B* (solid points) and compared with histograms generated by extracting D_S from simulated Brownian trajectories with the same distribution of track lengths observed in experiments (dashed lines). The width and asymmetric shape of simulated histogram arises from their being finite track lengths (at least 16 segments). Before the addition of antigen (top), the widths of diffusion coefficient histograms are well approximated by the Brownian simulation, suggesting a homogenous population of receptors is resolved in these measurements. After stimulation, measured histograms shift to lower values of D_S , and broaden when compared to the Brownian simulations.



Three dimensional histograms are displayed as contour plots in Fig. 2.7 *D* for several stimulation times. In unstimulated cells, receptor diffusion appears relatively unconstrained, and the ensemble of single molecules experiences roughly the same local environment at the frame rates used in these experiments (~30/s). This is not surprising given that receptors typically move hundreds of nanometers between observations, and over several square microns in a typical trajectory. Lipid-mediated and/or actin-generated obstacles to diffusion are expected to occur on smaller length-scales in unstimulated cells, and so single receptors are expected to sample a large number of local environments in a single trajectory. At long times, we observe a homogeneous but broad distribution in the D_S vs. receptor density histogram in Fig. 2.7 *D*. This is a result of both a distribution of receptor densities in puncta and individual receptors confined to sample the local environment of single puncta over their recorded trajectories.

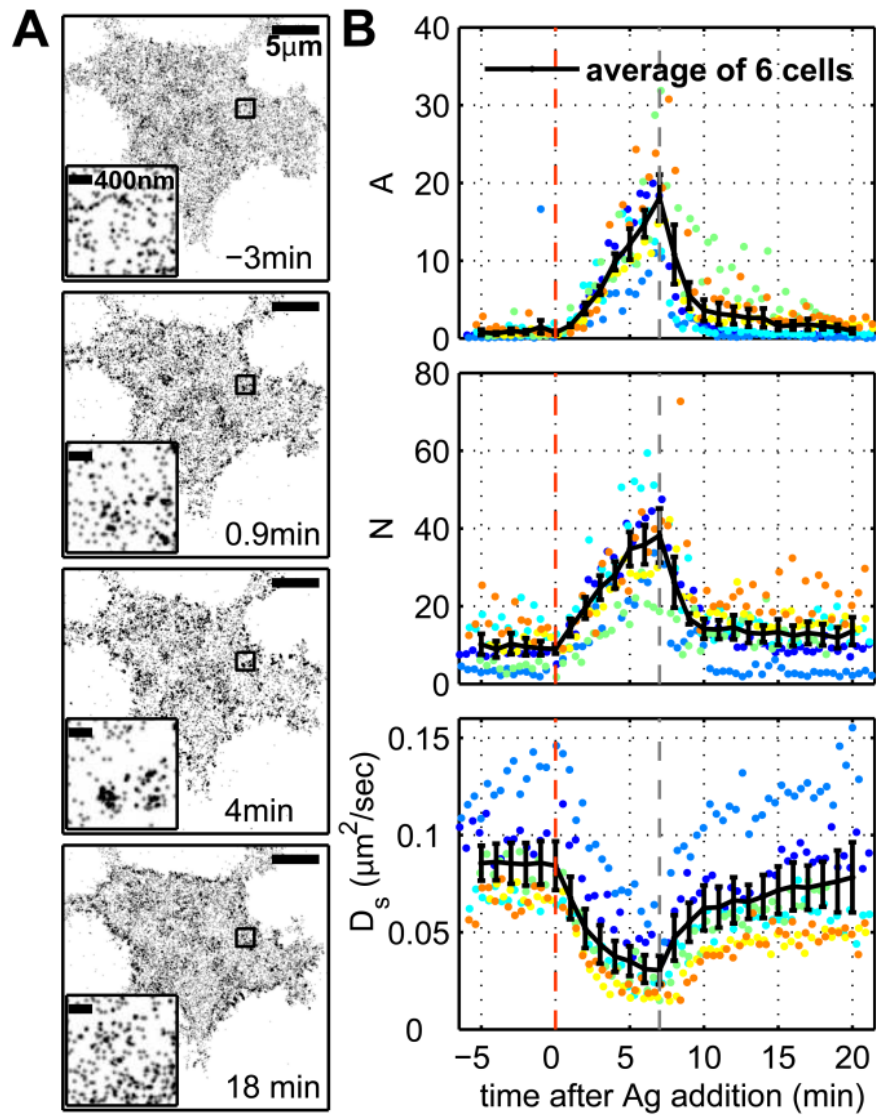
Soon after stimulation with antigen, histograms are elongated, extending between faster moving receptors in a low density local environment to slower moving receptors in a higher density local environment. In some cases, two peaks are observed as indicated by the orange triangles in Fig. 2.7 *D*. This elongated distribution could arise from receptors sampling a heterogeneous membrane environment. We think it is more likely that this elongated distribution arises from receptors slowly exchanging between a more mobile, less aggregated state and a less mobile, cluster-associated state over the length of the trajectory, as appears to be the case from visual inspection of single trajectories (Fig. 2.7 *A*).

Elongated distributions in Fig. 2.7 D occur are observed before the onset of Ca^{2+} mobilization, and transient associations of individual receptors could represent interactions that result in signaling. This also suggests that receptor aggregation is dynamic, at least in early signaling stages. Consistent with this interpretation, it has been shown previously that readily dissociable cross-linked receptors are primarily responsible for generating downstream signaling responses (42). Previous work has also shown that initial binding of DNP-BSA to IgE is primarily monovalent, and that cross-linking occurs slowly as DNP haptens on the receptor-bound antigen subsequently become available for binding (34). This is in good agreement with our current observations suggesting transient association of receptors with receptor clusters soon after antigen addition.

Receptor clustering, immobilization, and confinement is reversible in live cells

A monovalent DNP hapten, DNP-aminocaproyl-L-tyrosine (DCT), competes with multivalent DNP-BSA for binding to anti-DNP IgE (42). The addition of an excess of DCT following antigen stimulation reverses antigen-induced cross-linking and results in the cessation of signaling (42, 50, 51). The representative live cell super-resolution images in Fig. 2.9 A show uniform distribution of AF647-IgE bound to Fc ϵ RI before antigen addition, clustered IgE-Fc ϵ RI distribution after 7 min of antigen stimulation, and uniform distribution of receptors after DCT incubation for 10min. The average time-dependence of A, N, and D_s from 6 live cell experiments quantify the reversal of clustering and immobilization upon DCT exposure (Fig. 2.9 B). IgE-Fc ϵ RI clusters are dispersed on the time scale of several minutes, as shown by a decrease in A. Likewise,

Fig. 2.9 Antigen-induced changes in receptor clustering and mobility are reversible. (A) Reconstructed images of an AF647-IgE-labeled living cell before and after stimulation and subsequent addition of DCT. Each image is reconstructed from 80 s of acquired data. Insets show magnified images of the regions outlined with black squares. DNP-BSA (0.1 $\mu\text{g/ml}$) was added at 0 min, and DCT (200 μM) was added at 7 min. (B) The parameters A, N, and D_s are calculated as in Fig. 2.3 C and Fig. 2.4 C. The average A, N, and D_s , indicated by black lines, for 6 live cell experiments distinguished by different colors, over the time course of stimulation and DCT addition are shown. Antigen addition is indicated by the orange dashed line at 0 min, and DCT addition is indicated by the grey dashed line at 7 min.

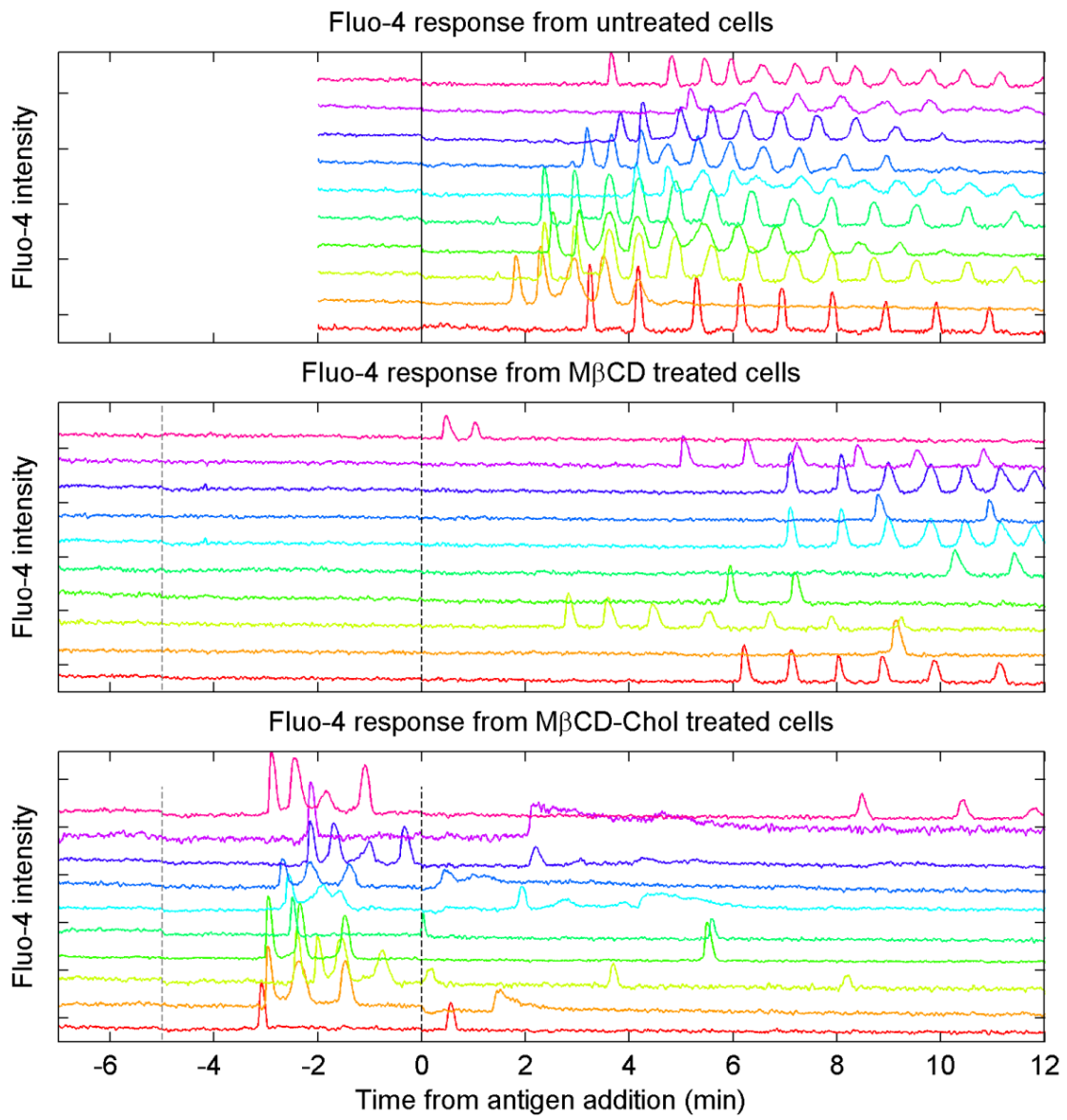


N and D_S recover close to pre-stimulation levels within 10 min of DCT addition. These data indicate that receptor immobilization is reversible and dependent on receptor cross-linking, as has been shown previously by FPR measurements that used DCT to reverse receptor immobilization (5). This reversibility demonstrates that the densely-packed and immobile receptor clusters formed within 7 min of antigen addition are not stabilized solely through interactions with other cellular components or that these interactions are insufficient to stabilize clusters in the absence of antigen cross-linking.

Cholesterol perturbations affect antigen-stimulated degranulation and Ca^{2+} responses in live cells.

To probe the effects of cholesterol perturbations on signaling downstream of initial receptor clustering, we observed the Ca^{2+} responses of cells subjected to cholesterol depletion using methyl-beta-cyclodextrin (M β CD) or cholesterol enrichment using M β CD pre-complexed to cholesterol (M β CD+chol). Cytoplasmic Ca^{2+} concentrations were imaged using the Ca^{2+} -sensitive dye Fluo-4 for large fields of cells treated with M β CD or M β CD+chol (or neither in the case of control cells) followed by stimulation with antigen as described in the Materials and Methods. We observe perturbation-dependent differences in the shape, duration, and frequency of oscillations in the Fluo-4 intensity traces for individual cells (Fig. 2.10). Compared to untreated cells, Ca^{2+} oscillations due to the addition of antigen are delayed in individual M β CD-treated cells, and oscillations are less frequent (Fig. 2.10, top), consistent with the attenuated total intensity and delayed onset of initial Ca^{2+} responses we observe for the population of cells (Fig. 2.13, B and C). M β CD+chol treated cells begin to display Ca^{2+} oscillations

Fig. 2.10 The shape, frequency, and duration of Ca²⁺ oscillations are severely affected by changes in cellular cholesterol. Cytoplasmic Ca²⁺ concentrations were imaged for large fields of Fluo-4-AM loaded cells treated with MβCD (top), MβCD+chol (bottom), or neither in the case of control cells (middle), followed by stimulation with antigen as described in the Materials and Methods. Fluo-4 intensity traces are shown for representative individual cells, where intensity traces are displaced on the y axis and the y axis also delineates Fluo-4 intensity for individual cells. Traces are shown in different colors for clarity. The dotted gray line at -5 min indicates the addition of MβCD or MβCD+chol, and the dotted black line indicates the addition of 0.1 μg/ml DNP-BSA.



upon the addition of M β CD+chol. These oscillations are robust for ~2 min but decrease in amplitude quickly after that time. Upon antigen addition, M β CD+chol-treated cells exhibit solitary, low-amplitude increases in cytoplasmic Ca²⁺ but do not display regular oscillations as in the case of untreated cells.

The β -hexosaminidase release assay was used to measure the levels of degranulation in adherent RBL-2H3 cells in response to cholesterol perturbation and antigen stimulation. Cholesterol reduction results in a slight increase in spontaneous degranulation in the absence of antigen and a decrease in antigen-stimulated degranulation compared to cells in the presence or absence of antigen which are not subjected to cholesterol perturbation (Fig. 2.11). Similar experiments have previously been reported in the literature and have shown mixed results for the effect of cholesterol reduction on degranulation, where some report enhanced degranulation without stimulation and/or inhibited degranulation in the presence of antigen, and others do not observe significant changes (52–56). However, these previous experiments were conducted under varying conditions of cholesterol reduction, stimulation, etc, which may have significant effects on degranulation measurements. Cholesterol enrichment strongly inhibits degranulation either in the presence or absence of antigen.

Receptor organization and mobility in response to cholesterol perturbation in unstimulated cells

To examine the role of lipid-mediated membrane heterogeneity on early and later stages of antigen stimulation, we investigated the impact of membrane cholesterol levels on receptor organization and mobility. Receptor diffusion (D_s) and clustering (N)

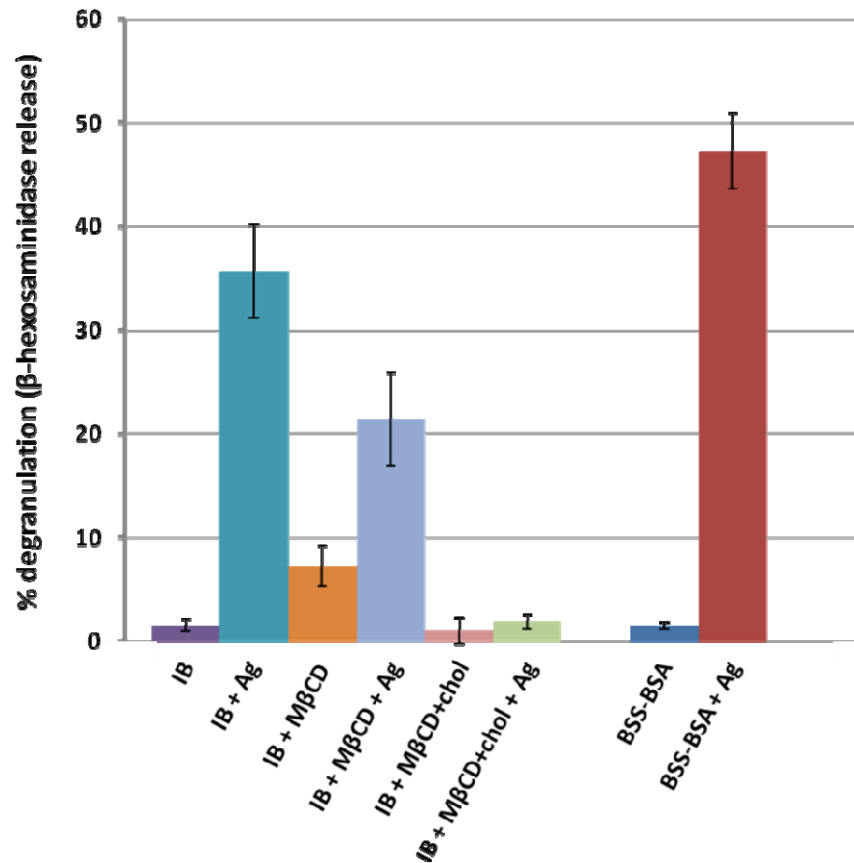


Fig. 2.11 Cholesterol perturbations affect the extent of antigen-stimulated degranulation as measured by β -hexosaminidase release. RBL-2H3 degranulation was measured using a β -hexosaminidase release fluorogenic assay in super-resolution imaging buffer (IB) at 37°C, with and without addition of 0.1 μ g/ml DNP-BSA (Ag), and in the presence or absence of 10mM M β CD or M β CD+chol. β -hexosaminidase signal has been normalized using samples of cells lysed with TritonX-100 (TX-100) as a measure of total β -hexosaminidase content. Error bars represent standard error of the mean of multiple samples measured for each condition. Additional control samples were made in BSS + 1mg/ml BSA to test for the effect of the imaging buffer.

upon cross-linking with antigen are measured for multiple live cells exposed to either M β CD to reduce, or M β CD+chol to enrich plasma membrane cholesterol (Figs. 2.12 through 2.14). Under our conditions, we expect approximately 20% decrease in the total cellular cholesterol content after 5 minutes of M β CD addition and ~50% decrease after 15 minutes (53).

In the absence of cross-linking by antigen, local receptor density changes due to variations in membrane cholesterol concentration. Fig. 2.12 shows representative super-resolution images of AF647-IgE/Fc ϵ RI with and without antigen treatment for individual cells with M β CD or M β CD+chol. IgE-Fc ϵ RI remains largely randomly distributed in unstimulated cells with reduced cholesterol levels, but becomes tightly clustered in unstimulated cells with elevated cholesterol levels. This visual observation is quantified in Fig. 2.13 and 2.14 in plots of D_S , A , and N as a function of time and treatment with M β CD or M β CD+chol. However, although we observe clustering in super-resolution experiments and transient increases in cytoplasmic Ca²⁺ upon treatment of cells with M β CD+chol, these responses to cholesterol loading do not result in signaling sufficient for degranulation (Fig. 2.10-2.12, 2.14).

It is likely that other cellular processes contribute to the organization and mobility of receptors in cholesterol-loaded cells. For example, we observe robust antigen-independent activation of transient Ca²⁺ oscillations after cells are incubated with M β CD+chol for 2 minutes that persists until approximately 5 minutes after M β CD+chol is added (Fig. 2.10 and 2.13, *B* and *C*). This indicates that the cellular environment changes dramatically in response to M β CD+chol in ways that may not be directly related to cholesterol's effects on lipid-mediated membrane organization. Modulating

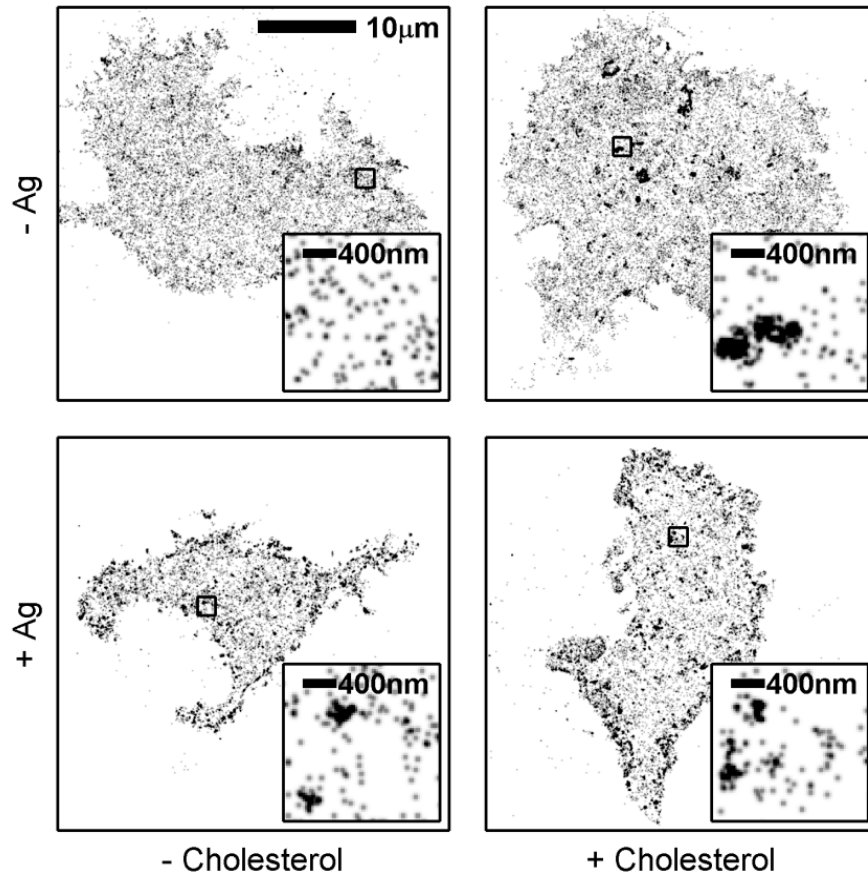
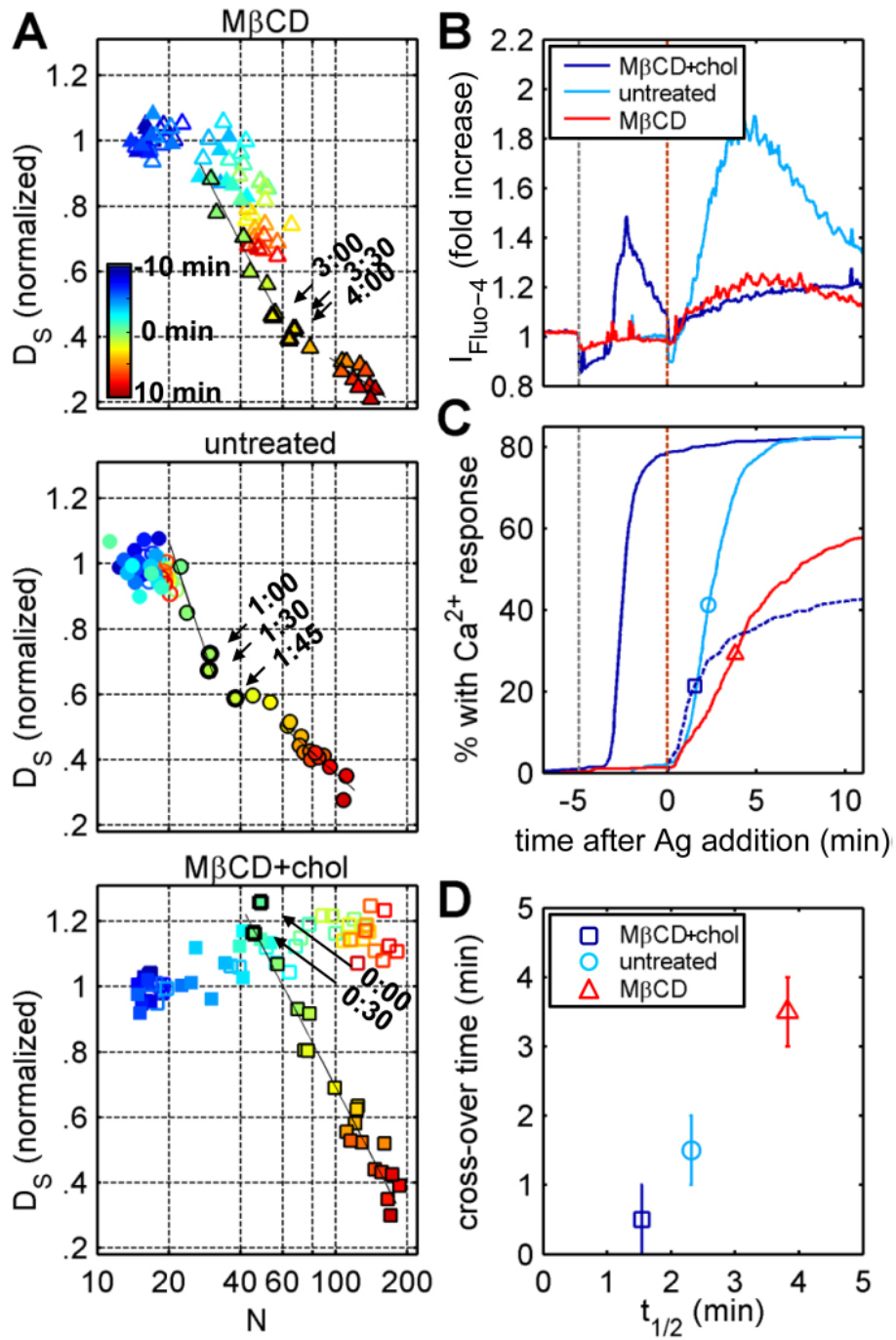


Fig. 2.12 Perturbations of membrane cholesterol alter receptor clustering.

Representative images of live cells after 15 min of 10mM M β CD (left) or M β CD+chol(right) in the absence (top) or presence (bottom) of incubation with 0.1 μ g/ml antigen for 10 min. Images are reconstructed from 80 s of acquired data. Insets show magnified images of the regions outlined with black squares.

Fig. 2.13 Perturbations of membrane cholesterol have corresponding effects on receptor diffusion, receptor clustering, and cellular Ca^{2+} responses. (A) Average D_S and N from 5 live cells for each of six treatments: M β CD+chol (top), no perturbation (middle), or M β CD (bottom), in the presence (solid symbols) and absence (open symbols) of antigen stimulation (0.1 $\mu\text{g}/\text{ml}$). Changing color from blue to red indicates advancement in time by 30 s for each time point from -10 to 10 min after the addition of antigen for or a blank addition of buffer for unstimulated cells. Cholesterol perturbations are added, where applicable, at -5 min. For stimulated time points (solid symbols outlined in black), fit lines are shown in black and represent linear fits of the time points belonging to the two regimes of D_S dependence on N , weighted by the inverse of the standard error of the mean in D_S and N . Stimulated time points near the cross-over are indicated by arrows and labeled with time after antigen addition. (B) Total fluorescence intensity is shown for populations of cells (at least 500) loaded with Fluo-4-AM and treated with M β CD, M β CD+chol, or no perturbation as a function of time. The dotted gray line at -5 min indicates the addition of M β CD or M β CD+chol and the dotted orange line indicates the addition of antigen. (C) The cumulative distribution in time of cells with an initial Ca^{2+} response as monitored by Fluo-4 fluorescence. The dark blue dotted line indicates the cumulative distribution of cells treated with M β CD+chol that exhibit an additional Ca^{2+} response following the addition of antigen. The half-maximum times ($t_{1/2}$) of cumulative curves are denoted by open symbols. (D) The estimated midpoints of the cross-over times are plotted vs. $t_{1/2}$ for each cholesterol treatment. Error bars represent uncertainty in determining the midpoint of the cross-over time by plus or minus 30 s.

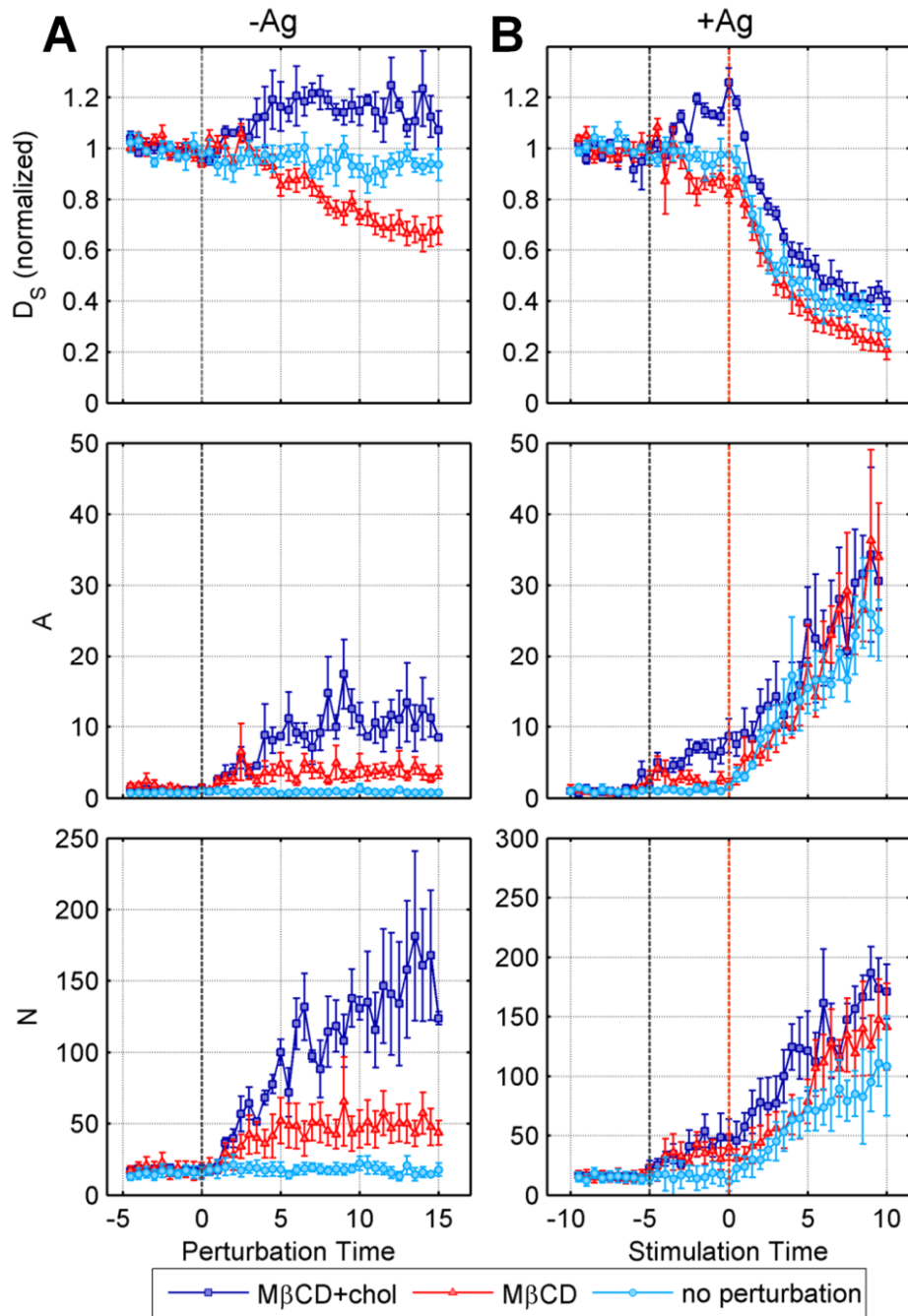


cellular cholesterol levels also leads to changes in receptor diffusion in unstimulated cells. M β CD addition to unstimulated cells results in a time-dependent decline in D_S over 15 minutes, and incubation with M β CD+chol leads to slight increases in D_S (Fig. 2.14) despite the large increases in receptor clustering described above. These observations could be the result of changes in membrane surface area, changes in the surface density of immobile obstacles, or induction of solid phase domains (57).

Receptor organization and mobility in response to cholesterol perturbation in stimulated cells

Perturbations of membrane cholesterol also affect the organization and mobility of IgE-Fc ϵ RI complexes when receptors are subsequently cross-linked with multivalent antigen (Fig. 2.13 A, 2.14). For both cholesterol reduction and enrichment, receptor clustering increases and receptor diffusion decreases in response to antigen, qualitatively similar to trends in the absence of perturbation (Figs. 2.5 A and 2.13 A). We observe two distinct regimes in plots of D_S vs. N for points after antigen addition in cells pretreated with M β CD, as is also observed in cells in the absence of cholesterol modulation. The cross-over between these two regimes occurs at larger values of N in cells with reduced cholesterol levels ($N < 40$ for untreated vs. $N > 60$ for M β CD treated cells, Fig. 2.13 A, top), which also corresponds to longer stimulation times at the cross-over point (~ 1 min for untreated vs. ~ 3 min for M β CD treated cells). For cells pretreated with M β CD+chol (Fig. 2.13 A, bottom), only one regime is apparent in plots of D_S vs. N , and the N is larger prior to antigen addition.

Fig. 2.14 Cholesterol perturbation affects average parameter values in live cell experiments. The effects of methyl- β -cyclodextrin (M β CD, red) and cholesterol-complexed methyl- β -cyclodextrin (M β CD+chol, dark blue) on average values for AF647-IgE short-time diffusion constant D_S , correlation function amplitude (A), and average number of correlated proteins (N) are measured as a function of time after the addition of the perturbation (gray dashed line). These are compared to control experiments where no perturbation is added (light blue). In (A), cells are treated with M β CD or M β CD+chol alone (or no treatment for control cells), and in (B), cells are stimulated with antigen 5 min after M β CD or M β CD+chol is added (orange dashed line), or 10 min after the start of imaging for control cells. In (A) and (B), each time trace represents the average of 4-5 independent live cell experiments. Error bars represent standard error of the mean.



Antigen-induced functional responses are also affected in cells pretreated with M β CD or M β CD+chol. Antigen-induced signaling is less effective in cells with reduced cholesterol levels when stimulated degranulation is assessed (52, 54–56), (Fig. 2.11). When Ca²⁺ mobilization is again used as a rough measure of the onset of cellular signaling as in Fig. 2.5, pretreatment of cells with M β CD results in a Ca²⁺ response that is both reduced in magnitude (Fig. 2.13 *B*) and delayed (Fig. 2.13 *C*) compared to untreated cells. A fraction (~40%) of cells pretreated with M β CD fail to show Ca²⁺ responses within 10 min after antigen addition. We quantify the timing of antigen-induced Ca²⁺ mobilization by measuring the time taken for 50% of responding cells to show an initial Ca²⁺ response, $t_{1/2}$, as indicated by the symbols on the cumulative distributions shown in Fig. 2.13 *C*. Antigen-induced signaling is attenuated in cells pretreated with M β CD+chol when assayed by degranulation (Fig. 2.11) or measurements of Ca²⁺ mobilization (Fig. 2.13).

For the case of cholesterol enrichment, we observe an initial Ca²⁺ response after M β CD+chol is added as described above, followed by a second, weaker, Ca²⁺ signal in response to antigen (Fig. 2.13 *B*). A large fraction (~60%) of M β CD+chol-treated cells also fail to exhibit an antigen-induced Ca²⁺ response (Fig. 2.13 *C*), although cells that do respond do so with a minimal time lag after antigen addition. As a result, $t_{1/2}$ is shorter compared to either untreated or M β CD-treated cells (Fig 2.13 *D*). These differences in the nature of the antigen-dependent Ca²⁺ response may be influenced by the M β CD+chol-induced Ca²⁺ transient observed prior to antigen addition. As described above, the shape, frequency, and duration of Ca²⁺ oscillations are also severely affected by changes in cellular cholesterol (Fig. 2.10).

$t_{1/2}$ is correlated with the timing of the cross-over observed in plots of D_s vs. N for the three cholesterol treatments (Fig. 2.13 *D*). In spite of the uncertainty in relating the timing of Ca^{2+} mobilization to super-resolution measurements discussed above, we observe differences in the relative timing of the cross-over and $t_{1/2}$ that are both dependent on cholesterol perturbation. This observation supports our conclusion that the initial, rapid decrease in the diffusion coefficient of IgE-Fc ϵ RI receptors is a consequence of interactions that precede Ca^{2+} mobilization, whereas the accumulation of receptors into densely packed clusters represents receptors after the onset of signaling. For the case of cholesterol reduction, antigen-induced slowing of receptor diffusion occurs at a slower rate than in untreated or cholesterol enriched cells (Fig. 2.13A), suggesting that initial signaling steps occur over a longer time period. This is consistent with our observations of a slower Ca^{2+} response in M β CD-treated cells compared to untreated cells. The cross-over between regimes occurs at larger values of N in M β CD treated vs. untreated cells, suggesting that more receptors are needed to initiate downstream signaling events when cholesterol levels are reduced. Plots of D_s vs. N for cholesterol-enriched cells indicate only a single regime, and antigen-induced Ca^{2+} responses occur with a minimal time lag after antigen addition.

Previous work has demonstrated the importance of membrane lipid-mediated protein targeting for transmembrane signaling in the Fc ϵ RI cascade (58, 59). Cholesterol reduction inhibits stimulated receptor phosphorylation by Lyn, and productive signaling only occurs upon the redistribution of receptors, kinases, and phosphatases via changes in the local lipid environment surrounding cross-linked receptors (52, 60, 61). In our previous SEM work we found that cholesterol reduction

prior to antigen addition led to smaller IgE-FcεRI rich clusters and reduced Lyn partitioning into receptor-rich clusters when cells were chemically fixed 1 min after antigen addition at 37°C. While it is not possible to compare absolute numbers between these experiments due to the different labeling strategies employed, our current findings are consistent with these previous results. Specifically, we find that it takes longer for receptors to assemble into tight clusters when cells are pretreated with MβCD, so at a given time-point after stimulation, we would expect receptor-rich clusters to be smaller in MβCD-pretreated cells compared to untreated cells. Our observations of a delay in Ca²⁺ responses in MβCD-pretreated cells relative to untreated cells are consistent with our past observations of defects in Lyn recruitment under these conditions. These findings are consistent with an inhibitory role for cholesterol reduction in signaling that has been supported by previous observations (52, 55, 56). An alternative explanation for the changes in diffusion vs. clustering behavior and Ca²⁺ responses observed in MβCD- and MβCD+chol-treated cells are related to more global effects of cholesterol modulation, such as its perturbation of the actin cytoskeleton. Cholesterol reduction can disrupt cytoskeleton-membrane attachment through perturbation of plasma membrane PIP₂ (62), or because actin is frequently coupled to the plasma membrane via more ordered regions (63). Therefore, the changes in receptor clustering, receptor mobility, and Ca²⁺ responses caused by MβCD and by extension MβCD+chol may be indirect results of membrane cholesterol modulation via its effects on the actin cytoskeleton.

CONTRIBUTIONS AND ACKNOWLEDGEMENTS

Research designed by S. A. Shelby, D. A. Holowka, B. A. Baird and S. L. Veatch; S. A. Shelby performed super-resolution imaging experiments and degranulation experiments. S. A. Shelby and S. L. Veatch analyzed super resolution data. S. L. Veatch performed and analyzed calcium mobilization experiments. Paper written by S. A. Shelby, D. A. Holowka, B. A. Baird, and S. L. Veatch. Research was supported through grants from the NIH: R00GM087810 (S. L. Veatch), RO1 AI018306 (D. A. Holowka and B. A. Baird). S. A. Shelby acknowledges partial support from the Molecular Biophysics Training Grant (T32GM008267).

REFERENCES

1. Siraganian, R.P. 2003. Mast cell signal transduction from the high-affinity IgE receptor. *Curr. Opin. Immunol.* 15: 639–646.
2. Blank, U., and J. Rivera. 2004. The ins and outs of IgE-dependent mast-cell exocytosis. *Trends Immunol.* 25: 266–273.
3. Gilfillan, A.M., and J. Rivera. 2009. The tyrosine kinase network regulating mast cell activation. *Immunol. Rev.* 228: 149–169.
4. Schlessinger, J., W.W. Webb, E.L. Elson, and H. Metzger. 1976. Lateral motion and valence of Fc receptors on rat peritoneal mast cells. *Publ. Online* 09 Dec. 1976 Doi101038264550a0. 264: 550–552.
5. Menon, A.K., D.A. Holowka, W.W. Webb, and B.A. Baird. 1986. Cross-linking of receptor-bound IgE to aggregates larger than dimers leads to rapid immobilization. *J. Cell Biol.* 102: 541–550.
6. Stump, R.F., J.R. Pfeiffer, J. Seagrave, and J.M. Oliver. 1988. Mapping gold-labeled IgE receptors on mast cells by scanning electron microscopy: receptor distributions revealed by silver enhancement, backscattered electron imaging, and digital image analysis. *J. Histochem. Cytochem. Off. J. Histochem. Soc.* 36: 493–502.
7. Wilson, B.S., J.R. Pfeiffer, and J.M. Oliver. 2000. Observing Fc ϵ RI signaling from the inside of the mast cell membrane. *J. Cell Biol.* 149: 1131–1142.
8. Veatch, S.L., E.N. Chiang, P. Sengupta, D.A. Holowka, and B.A. Baird. 2012. Quantitative nanoscale analysis of IgE-Fc ϵ RI clustering and coupling to early signaling proteins. *J. Phys. Chem. B.* 116: 6923–6935.
9. Menon, A.K., D.A. Holowka, W.W. Webb, and B.A. Baird. 1986. Clustering, mobility, and triggering activity of small oligomers of immunoglobulin E on rat basophilic leukemia cells. *J. Cell Biol.* 102: 534–540.
10. Feder, T.J., I. Brust-Mascher, J.P. Slattery, B. Baird, and W.W. Webb. 1996. Constrained diffusion or immobile fraction on cell surfaces: a new interpretation. *Biophys. J.* 70: 2767–2773.
11. Larson, D.R., J.A. Gosse, D.A. Holowka, B.A. Baird, and W.W. Webb. 2005. Temporally resolved interactions between antigen-stimulated IgE receptors and Lyn kinase on living cells. *J. Cell Biol.* 171: 527–536.
12. Andrews, N.L., K.A. Lidke, J.R. Pfeiffer, A.R. Burns, B.S. Wilson, J.M. Oliver, and D.S. Lidke. 2008. Actin restricts Fc ϵ RI diffusion and facilitates antigen-induced receptor immobilisation. *Nat. Cell Biol.* 10: 955–963.

13. Andrews, N.L., J.R. Pfeiffer, A.M. Martinez, D.M. Haaland, R.W. Davis, T. Kawakami, J.M. Oliver, B.S. Wilson, and D.S. Lidke. 2009. Small, mobile Fc ϵ R1 aggregates are signaling competent. *Immunity*. 31: 469–479.
14. Spendier, K., K.A. Lidke, D.S. Lidke, and J.L. Thomas. 2012. Single-particle tracking of immunoglobulin E receptors (Fc γ RI) in micron-sized clusters and receptor patches. *FEBS Lett.* 586: 416–421.
15. Rust, M.J., M. Bates, and X. Zhuang. 2006. Stochastic optical reconstruction microscopy (STORM) provides sub-diffraction-limit image resolution. *Nat. Methods*. 3: 793–795.
16. Heilemann, M., S. van de Linde, M. Schüttpeitz, R. Kasper, B. Seefeldt, A. Mukherjee, P. Tinnefeld, and M. Sauer. 2008. Subdiffraction-Resolution Fluorescence Imaging with Conventional Fluorescent Probes. *Angew. Chem. Int. Ed.* 47: 6172–6176.
17. Betzig, E., G.H. Patterson, R. Sougrat, O.W. Lindwasser, S. Olenych, J.S. Bonifacino, M.W. Davidson, J. Lippincott-Schwartz, and H.F. Hess. 2006. Imaging Intracellular Fluorescent Proteins at Nanometer Resolution. *Science*. 313: 1642 – 1645.
18. Hess, S.T., T.P.K. Girirajan, and M.D. Mason. 2006. Ultra-High Resolution Imaging by Fluorescence Photoactivation Localization Microscopy. *Biophys. J.* 91: 4258–4272.
19. Greenfield, D., A.L. McEvoy, H. Shroff, G.E. Crooks, N.S. Wingreen, E. Betzig, and J. Liphardt. 2009. Self-Organization of the Escherichia coli Chemotaxis Network Imaged with Super-Resolution Light Microscopy. *PLoS Biol.* 7.
20. Lillemeier, B.F., M.A. Mortelmaier, M.B. Forstner, J.B. Huppa, J.T. Groves, and M.M. Davis. 2010. TCR and Lat are expressed on separate protein islands on T cell membranes and concatenate during activation. *Nat Immunol.* 11: 90–96.
21. Owen, D.M., C. Rentero, J. Rossy, A. Magenau, D. Williamson, M. Rodriguez, and K. Gaus. 2010. PALM imaging and cluster analysis of protein heterogeneity at the cell surface. *J. Biophotonics*. 3: 446–454.
22. Williamson, D.J., D.M. Owen, J. Rossy, A. Magenau, M. Wehrmann, J.J. Gooding, and K. Gaus. 2011. Pre-existing clusters of the adaptor Lat do not participate in early T cell signaling events. *Nat Immunol.* 12: 655–662.
23. Hsu, C.-J., and T. Baumgart. 2011. Spatial Association of Signaling Proteins and F-Actin Effects on Cluster Assembly Analyzed via Photoactivation Localization Microscopy in T Cells. *PLoS ONE*. 6.
24. Sherman, E., V. Barr, S. Manley, G. Patterson, L. Balagopalan, I. Akpan, C.K. Regan, R.K. Merrill, C.L. Sommers, J. Lippincott-Schwartz, and L.E. Samelson.

2011. Functional Nanoscale Organization of Signaling Molecules Downstream of the T Cell Antigen Receptor. *Immunity*. 35: 705–720.
25. Gunewardene, M.S., F.V. Subach, T.J. Gould, G.P. Penoncello, M.V. Gudheti, V.V. Verkhusha, and S.T. Hess. 2011. Superresolution imaging of multiple fluorescent proteins with highly overlapping emission spectra in living cells. *Biophys. J.* 101: 1522–1528.
 26. Jones, S.A., S.-H. Shim, J. He, and X. Zhuang. 2011. Fast, three-dimensional super-resolution imaging of live cells. *Nat. Methods*. 8: 499–508.
 27. Manley, S., J.M. Gillette, G.H. Patterson, H. Shroff, H.F. Hess, E. Betzig, and J. Lippincott-Schwartz. 2008. High-density mapping of single-molecule trajectories with photoactivated localization microscopy. *Nat Meth.* 5: 155–157.
 28. Manley, S., J.M. Gillette, and J. Lippincott-Schwartz. 2010. Single-particle tracking photoactivated localization microscopy for mapping single-molecule dynamics. *Methods Enzymol.* 475: 109–120.
 29. Giannone, G., E. Hosy, F. Levet, A. Constals, K. Schulze, A.I. Sobolevsky, M.P. Rosconi, E. Gouaux, R. Tampé, D. Choquet, and L. Cognet. 2010. Dynamic Superresolution Imaging of Endogenous Proteins on Living Cells at Ultra-High Density. *Biophys. J.* 99: 1303–1310.
 30. Gosse, J.A., A. Wagenknecht-Wiesner, D. Holowka, and B. Baird. 2005. Transmembrane Sequences Are Determinants of Immunoreceptor Signaling. *J. Immunol.* 175: 2123–2131.
 31. Hardy, R.R. 1986. *Handbook of Experimental Immunology*. 4th ed. Oxford, UK: Blackwell Scientific Publication.
 32. Veatch, S.L., B.B. Machta, S.A. Shelby, E.N. Chiang, D.A. Holowka, and B.A. Baird. 2012. Correlation functions quantify super-resolution images and estimate apparent clustering due to over-counting. *PLoS One*. 7: e31457.
 33. Erickson, J., B. Goldstein, D. Holowka, and B. Baird. 1987. The effect of receptor density on the forward rate constant for binding of ligands to cell surface receptors. *Biophys. J.* 52: 657–662.
 34. Jaqaman, K., D. Loerke, M. Mettlen, H. Kuwata, S. Grinstein, S.L. Schmid, and G. Danuser. 2008. Robust single-particle tracking in live-cell time-lapse sequences. *Nat. Methods*. 5: 695–702.
 35. Naal, R.M.Z.G., J. Tabb, D. Holowka, and B. Baird. 2004. In situ measurement of degranulation as a biosensor based on RBL-2H3 mast cells. *Biosens. Bioelectron.* 20: 791–796.

36. Machta, B.B., S. Papanikolaou, J.P. Sethna, and S.L. Veatch. 2011. Minimal Model of Plasma Membrane Heterogeneity Requires Coupling Cortical Actin to Criticality. *Biophys. J.* 100: 1668–1677.
37. Gadi, D., A. Wagenknecht-Wiesner, D. Holowka, and B. Baird. 2011. Sequestration of phosphoinositides by mutated MARCKS effector domain inhibits stimulated Ca(2+) mobilization and degranulation in mast cells. *Mol. Biol. Cell.* 22: 4908–4917.
38. Barisas, B.G., S.M. Smith, J. Liu, J. Song, G.M. Hagen, I. Pecht, and D.A. Roess. 2007. Compartmentalization of the Type I Fc epsilon receptor and MAFA on mast cell membranes. *Biophys. Chem.* 126: 209–217.
39. Xu, K., B. Goldstein, D. Holowka, and B. Baird. 1998. Kinetics of Multivalent Antigen DNP-BSA Binding to IgE-FcεRI in Relationship to the Stimulated Tyrosine Phosphorylation of FcεRI. *J. Immunol.* 160: 3225–3235.
40. Ritchie, K., R. Iino, T. Fujiwara, K. Murase, and A. Kusumi. 2003. The fence and picket structure of the plasma membrane of live cells as revealed by single molecule techniques (Review). *Mol. Membr. Biol.* 20: 13–18.
41. Murase, K., T. Fujiwara, Y. Umemura, K. Suzuki, R. Iino, H. Yamashita, M. Saito, H. Murakoshi, K. Ritchie, and A. Kusumi. 2004. Ultrafine Membrane Compartments for Molecular Diffusion as Revealed by Single Molecule Techniques. *Biophys. J.* 86: 4075–4093.
42. Pierini, L., N.T. Harris, D. Holowka, and B. Baird. 1997. Evidence Supporting a Role for Microfilaments in Regulating the Coupling between Poorly Dissociable IgE-FcεRI Aggregates and Downstream Signaling Pathways. *Biochemistry.* 36: 7447–7456.
43. Ra, C., K. Furuichi, J. Rivera, J.M. Mullins, C. Isersky, and K.N. White. 1989. Internalization of IgE receptors on rat basophilic leukemic cells by phorbol ester. Comparison with endocytosis induced by receptor aggregation. *Eur. J. Immunol.* 19: 1771–1777.
44. Liu, C., H. Miller, K.L. Hui, B. Grooman, S. Bolland, A. Upadhyaya, and W. Song. 2011. A balance of Bruton's tyrosine kinase and SHIP activation regulates B cell receptor cluster formation by controlling actin remodeling. *J. Immunol. Baltim. Md* 1950. 187: 230–239.
45. Lee, K.-H., A.R. Dinner, C. Tu, G. Campi, S. Raychaudhuri, R. Varma, T.N. Sims, W.R. Burack, H. Wu, J. Wang, O. Kanagawa, M. Markiewicz, P.M. Allen, M.L. Dustin, A.K. Chakraborty, and A.S. Shaw. 2003. The immunological synapse balances T cell receptor signaling and degradation. *Science.* 302: 1218–1222.
46. Varma, R., G. Campi, T. Yokosuka, T. Saito, and M.L. Dustin. 2006. T Cell Receptor-Proximal Signals Are Sustained in Peripheral Microclusters and

- Terminated in the Central Supramolecular Activation Cluster. *Immunity*. 25: 117–127.
47. Weetall, M., D. Holowka, and B. Baird. 1993. Heterologous desensitization of the high affinity receptor for IgE (Fc ϵ RI) on RBL cells. *J. Immunol.* 150: 4072–4083.
 48. Paolini, R., M.H. Jouvin, and J.P. Kinet. 1991. Phosphorylation and dephosphorylation of the high-affinity receptor for immunoglobulin E immediately after receptor engagement and disengagement. *Nature*. 353: 855–858.
 49. Saxton, M.J. 1997. Single-particle tracking: the distribution of diffusion coefficients. *Biophys. J.* 72: 1744–1753.
 50. Fewtrell, C. 1985. *Calcium in Biological Systems*. New York: Plenum Press.
 51. Seagrave, J.C., G.G. Deanin, J.C. Martin, B.H. Davis, and J.M. Oliver. 1987. DNP-phycobiliproteins, fluorescent antigens to study dynamic properties of antigen-IgE-receptor complexes on RBL-2H3 rat mast cells. *Cytometry*. 8: 287–295.
 52. Sheets, E.D., D. Holowka, and B. Baird. 1999. Critical Role for Cholesterol in Lyn-mediated Tyrosine Phosphorylation of Fc ϵ RI and Their Association with Detergent-resistant Membranes. *J. Cell Biol.* 145: 877–887.
 53. Surviladze, Z., L. Dráberová, M. Kovářová, M. Boubelík, and P. Dráber. 2001. Differential sensitivity to acute cholesterol lowering of activation mediated via the high-affinity IgE receptor and Thy-1 glycoprotein. *Eur. J. Immunol.* 31: 1–10.
 54. Yamashita, T., T. Yamaguchi, K. Murakami, and S. Nagasawa. 2001. Detergent-resistant membrane domains are required for mast cell activation but dispensable for tyrosine phosphorylation upon aggregation of the high affinity receptor for IgE. *J. Biochem. (Tokyo)*. 129: 861–868.
 55. Kato, N., M. Nakanishi, and N. Hirashima. 2003. Cholesterol depletion inhibits store-operated calcium currents and exocytotic membrane fusion in RBL-2H3 cells. *Biochemistry*. 42: 11808–11814.
 56. Silveira e Souza, A.M.M., V.M. Mazucato, R.O. de Castro, F. Matioli, P. Ciancaglini, T. de Paiva Paulino, M.C. Jamur, and C. Oliver. 2008. The α -galactosyl derivatives of ganglioside GD1b are essential for the organization of lipid rafts in RBL-2H3 mast cells. *Exp. Cell Res.* 314: 2515–2528.
 57. Nishimura, S.Y., M. Vrljic, L.O. Klein, H.M. McConnell, and W.E. Moerner. 2006. Cholesterol depletion induces solid-like regions in the plasma membrane. *Biophys. J.* 90: 927–938.
 58. Silveira e Souza, A.M.M., V.M. Mazucato, M.C. Jamur, and C. Oliver. 2011. *Lipid Rafts in Mast Cell Biology*. *J. Lipids*. 2011.

59. Holowka, D., J.A. Gosse, A.T. Hammond, X. Han, P. Sengupta, N.L. Smith, A. Wagenknecht-Wiesner, M. Wu, R.M. Young, and B. Baird. 2005. Lipid segregation and IgE receptor signaling: A decade of progress. *Biochim. Biophys. Acta BBA - Mol. Cell Res.* 1746: 252–259.
60. Field, K.A., D. Holowka, and B. Baird. 1997. Compartmentalized Activation of the High Affinity Immunoglobulin E Receptor within Membrane Domains. *J. Biol. Chem.* 272: 4276 –4280.
61. Young, R.M., D. Holowka, and B. Baird. 2003. A Lipid Raft Environment Enhances Lyn Kinase Activity by Protecting the Active Site Tyrosine from Dephosphorylation. *J. Biol. Chem.* 278: 20746 –20752.
62. Kwik, J., S. Boyle, D. Fooksman, L. Margolis, M.P. Sheetz, and M. Edidin. 2003. Membrane cholesterol, lateral mobility, and the phosphatidylinositol 4,5-bisphosphate-dependent organization of cell actin. *Proc. Natl. Acad. Sci. U. S. A.* 100: 13964–13969.
63. Holowka, D., E. D. Sheets, and B. Baird. 2000. Interactions between FcεRI and lipid raft components are regulated by the actin cytoskeleton. *J. Cell Sci.* 113: 1009 –1019.

CHAPTER THREE

ANTIGEN-STIMULATED NANOSCALE CO-LOCALIZATION OF IgE RECEPTOR WITH LYN KINASE IS REGULATED BY THE ACTIN CYTOSKELETON

SUMMARY

Allergic signaling in mast cells is initiated by phosphorylation of the receptor for immunoglobulin E (IgE), Fc ϵ RI, when IgE-Fc ϵ RI complexes are cross-linked by binding of multivalent antigen. Lyn tyrosine kinase is the Src family kinase that is chiefly responsible for this initiation of Fc ϵ RI signaling. Using two-color super-resolution localization microscopy, we measure the distributions of IgE-Fc ϵ RI and Lyn on the plasma membrane of fixed cells with 20-25 nm resolution. By applying quantitative pair-correlation analysis, we detect spatial co-localization of Lyn with IgE within 1 min following antigen stimulation. The resolution afforded by our imaging technique gives us access to early time points during the initiation of signaling, when stimulated changes in membrane organization occur on length scales too small to be detectable by other optical methods. With this improved sensitivity, we investigate the role of the actin cytoskeleton in regulating interactions of Lyn with Fc ϵ RI. Cells treated with agents that inhibit actin polymerization exhibit enhanced antigen-stimulated coupling to Lyn in mast cells. In fixed cell imaging experiments, inhibition of actin polymerization causes enhancement of Lyn co-localization with Fc ϵ RI at time points soon after antigen addition, accompanied by augmented tyrosine phosphorylation of receptor clusters. Based on comparison with differently anchored analogues, the lipid environment of Lyn

is implicated as a mediator of this regulation by F-actin. Our results are consistent with the idea that IgE receptor signaling is negatively regulated by the actin cytoskeleton via modulation of the spatial association of Lyn with FcεRI that is mediated by plasma membrane lipids. Implementation of super-resolution microscopy has allowed us to visualize this spatial regulation of Lyn coupling to FcεRI on the scale of molecular complexes.

INTRODUCTION

In mast cells, cellular signaling that results in the allergic immune response depends on the spatial rearrangement of signaling molecules on the plasma membrane. Cross-linking of immunoglobulin E (IgE) bound to its high-affinity receptor, FcεRI, by multivalent antigen causes the formation of receptor clusters at the plasma membrane. Receptor clustering promotes phosphorylation of immunoreceptor tyrosine-based activation motifs (ITAMs) on the β and γ₂ subunits by the Src family kinase Lyn, which is independently anchored to the plasma membrane, followed by recruitment and activation of Syk kinase. Through phosphorylation of multiple Syk substrates, downstream signaling responses are initiated, including Ca²⁺ mobilization and release from the cell of secretory granules containing pro-inflammatory molecules (1–3). Lyn-mediated phosphorylation of FcεRI is the first biochemical step in the signaling response following receptor cross-linking (4–6). The stimulated capacity of Lyn to spatially associate with clustered IgE-FcεRI, such as through a shared lipid environment in the plasma membrane, is likely to be a crucial factor in its capacity to phosphorylate FcεRI and produce a signaling response. The mechanisms by which receptor clustering

initiates co-localization of Lyn with FcεRI and how this association is dynamically regulated before and during signaling continue to be open questions in the field.

Lyn may weakly associate with FcεRI β in the absence of receptor cross-linking (2, 7, 8), and this association increases via protein-protein and lipid-mediated interactions when receptors are clustered (9). Mutation of FcεRI-binding domains or inhibition of Lyn kinase activity result in a partial loss of Lyn association with cross-linked FcεRI when antigen is presented on patterned substrates (10, 11). There is also a large body of evidence that a shared preference of cross-linked FcεRI and Lyn for association with ordered lipids is a mechanism of association of clustered FcεRI (12–16). The order-preferring N-terminal sequence of Lyn that contains its palmitoylation and myristoylation sites has been found to be sufficient for co-localization with cross-linked receptor (10, 17, 18). Conversely, disruption of ordered lipids through depletion of membrane cholesterol prevents stimulated co-localization (9, 15). Co-compartmentalization of FcεRI with Lyn in ordered regions of the plasma membrane has been shown to be not only important for localization of Lyn at receptor clusters, but is also crucial for positive regulation of receptor phosphorylation and Lyn activity through protection from transmembrane phosphatases (14, 19, 20).

The cortical actin cytoskeleton can influence the organization of cell membrane components in general and has been implicated as a regulator of FcεRI signaling. Receptor cross-linking causes a stimulated increase in actin polymerization (21). Inhibition of actin polymerization with drugs such as latrunculin A and cytochalasin D enhances stimulatory responses at both early and late stages of the signaling cascade (22–28), suggesting a negative regulatory role for the actin cytoskeleton. Of interest to

us, actin appears to influence even the initial steps following receptor cross-linking, including Lyn co-localization to clustered receptors (10, 26, 29) and receptor phosphorylation (25, 26, 28). The molecular mechanism of how actin might regulate signaling on the level of receptor clustering and association with Lyn is unknown, but in several cases a relationship has been established between the cytoskeleton and ordered membrane lipids. For example, inhibition of actin polymerization caused by either cytochalasin treatment or antigen stimulation causes changes in the lipid composition of ordered membranes (30). One hypothesis is that through regulation of ordered membrane domains or interaction with order-preferring species, actin modulates the co-localization of Lyn with receptors to suppress an inappropriate signaling response (25, 26). Based on this existing evidence, a theoretical framework has been developed that describes how the actin cytoskeleton might facilitate nanoscale compartmentalization of the plasma membrane through interaction with lipid phase heterogeneity (31, 32), and thereby regulate membrane signaling processes such as coupling of Lyn and FcεRI.

The ability to measure the co-localization of Lyn and IgE-FcεRI on the nanoscale at early stimulation timepoints would enable investigation the spatial regulation of Lyn/FcεRI interactions and how it contributes to the initiation of signaling and the dynamic regulation of the response. Lyn association with IgE receptors has been measured by a number of biochemical techniques (7, 8, 12), but these approaches are severely limited in capturing the spatial component of signaling. Thus, direct visualization of Lyn coupling to IgE receptor during the initiation of signaling has proven difficult. At the resolution obtainable in standard optical microscopy experiments, the

distribution of immunolabeled Lyn or a transiently transfected fluorescent Lyn construct appears relatively uniform, appears unaffected by receptor cross-linking at physiological or room temperatures, and does not exhibit robust co-localization with IgE-FcεRI aggregates (26). Lyn co-localization with IgE-FcεRI has been observed under somewhat specialized stimulation conditions that stabilize large patches of cross-linked receptor at the membrane and inhibit receptor internalization, such as cross-linking at 4°C or in the presence of cytochalasin (15, 17, 18, 26), or presentation of antigen on micron-scale patterned substrates (10, 33). More sensitive optical techniques such as multiphoton FCS have also detected Lyn interactions with IgE receptor in living cells at room temperature (29). Even in these cases, Lyn co-localization or co-diffusion with IgE receptor is only observed at micron length scales after relatively long periods of receptor cross-linking for many minutes at room temperature, while receptor phosphorylation is observable at shorter timescales within a few minutes of antigen stimulation.

Direct imaging of Lyn/FcεRI co-localization has posed a challenge likely due to the small length scales of antigen-stimulated co-redistribution of Lyn and IgE-FcεRI. The dimensions of IgE-FcεRI clusters at the earliest stages of signaling are well below the diffraction limit of light (34–36), and local Lyn enrichment in clusters less than 100nm in dimension could be too subtle to detect by conventional fluorescence microscopy. Additionally, Lyn coupling to IgE-FcεRI could be controlled within compartmentalized structures of plasma membrane lipids and the actin cytoskeleton, the dimensions of which are also sub-diffraction (31, 32).

To image the co-localization of Lyn with IgE-FcεRI that occurs within minutes of receptor cross-linking with sufficient sensitivity to simultaneously assess the potentially

subtle effects of the actin cytoskeleton, we require spatial resolution on the length scale of receptor clusters or smaller. This chapter describes our quantitative characterization of antigen-stimulated Lyn recruitment to IgE-FcεRI complexes and resulting phosphorylation of receptor clusters using two-color super-resolution localization microscopy. This recently developed fluorescence microscopy technique affords spatial resolution improved by an order of magnitude compared to conventional fluorescence imaging (37–39). We quantify the nanoscale co-redistribution of Lyn with clustered FcεRI and test for effects of actin cytoskeleton perturbation using the actin polymerization inhibitors latrunculin A and cytochalasin D. These experiments demonstrate a regulatory role for F-actin in the spatial coupling of Lyn to FcεRI during the first few minutes of stimulation, and they clarify the mechanism of signaling enhancement caused by inhibition of actin polymerization. Through our use of super-resolution localization microscopy, we are able to contribute a picture of Lyn-IgE-FcεRI coupling at sufficiently high resolution to characterize the interaction between these proteins by direct imaging in cells stimulated with soluble antigen at physiological temperature. These advances bring us closer our goal of uncovering the physical mechanisms that give rise to the spatial regulation of FcεRI signaling, including the role of the actin cytoskeleton in regulation of membrane organization.

MATERIALS AND METHODS

Chemicals and reagents

Cell culture reagents, including Minimum Essential Medium (MEM), Trypsin-EDTA, and gentamicin sulfate, were acquired from Life Technologies (Carlsbad, CA). Fetal bovine serum (FBS) was purchased from Atlanta Biologicals (Atlanta, GA). Cell culture dishes were purchased from MatTek (Ashland, MA) and 125nm Tetraspeck fluorescent beads were purchased from Life Technologies. The amine reactive fluorophore Dy654 was purchased from Dyomics GmbH (Jena, Germany). Dy654-IgE was prepared by conjugating purified mouse monoclonal anti-2,4-dinitrophenyl (DNP) IgE with AF532 Dy654, as previously described (29, 40). Dy654-IgE was measured to have a dye:protein ratio of 2.7:1. Multivalent antigen, dinitrophenyl-conjugated BSA (DNP-BSA), with an average of 15 DNP molecules per BSA was prepared as described previously (41). Latrunculin A was purchased from both Life Technologies and Sigma-Aldrich (St. Louis, MO), and cytochalasin D was purchased from Sigma-Aldrich. Glutaraldehyde (25% stock) was purchased from Ted Pella (Redding, CA). Para-formaldehyde was purchased from Electron Microscopy Services (Hatfield, PA). Fish gelatin was purchased from Sigma. Supplies for the super-resolution buffer including β -mercaptoethanol, glucose oxidase, catalase, and Tris-HCl were acquired from Sigma. Antiphosphotyrosine clone 4G10 antibody was obtained from Millipore (Billerica, MA), and the AlexaFluor 488-conjugated anti-mouse IgG2_b secondary antibody was purchased from Life Technologies.

Fluorescent constructs and variant RBL cell lines

Lyn-mEos3.2 and mEos3.2-LifeAct constructs were prepared through site-directed mutagenesis to incorporate I102N, H158E, and Y189A mutations into mEos2

(42). Lyn-mEos2 and mEos2-LifeAct constructs were generous gifts from Dr. Sarah Veatch (University of Michigan). PM-mEos3.2 and mEos3.2-GG constructs were prepared through restriction enzyme excision of EGFP from PM-EGFP and EGFP-GG constructs followed by insertion and ligation of the mEos3.2 sequence. PM-EGFP and EGFP-GG were described previously (17). RBL 1C1C8 and Syk-negative RBL TB1A2 cell lines were gifts from Dr. Reuben Siraganian (NIH).

Preparation of fixed RBL-2H3 samples for imaging

Cell culture and plating

MatTek culture dishes were prepared to receive cell samples with addition of fiduciary markers. Dishes were oxygen plasma-cleaned for 3-5 minutes. Immediately following plasma-cleaning, a dilute solution (2:100-5:1000 in phosphate-buffered saline (PBS)) of Tetraspeck fluorescent nanospheres was applied to the glass coverslip surface in each dish. The Tetraspeck solution was incubated in the dishes for 30 min before they were rinsed three times with cell culture medium. Rat basophilic leukemia-2H3 (RBL-2H3) cells were maintained in culture using medium containing MEM 20% FBS, and 10 µg/ml gentamicin sulfate at 37°C and 5% CO₂ as described previously (40). 1C1C8 and TB1A2 RBL cell lines were cultured under identical conditions. RBL-2H3, 1C1C8, and Syk-negative TB1A2 cells were harvested using Trypsin-EDTA and were either plated onto prepared MatTek coverslip dishes or transiently transfected (RBL-2H3 or 1C1C8 cells) with a fluorescent construct before plating as described below. When cells were plated immediately after harvesting, 0.15×10^6 cells were

added to the coverslip dishes to achieve a sparse distribution for imaging before incubation overnight at 37°C.

Transient transfection

RBL-2H3 or 1C1C8 cells were transiently transfected with Lyn-mEos3.2, mEos3.2-LifeAct, PM-mEos3.2, or mEos3.2-GG fluorescent constructs using an electroporation procedure. Approximately 1.0×10^7 cells were harvested using Trypsin-EDTA, pelleted and resuspended in 500 μ l cold electroporation buffer (137 mM NaCl, 2.7 mM KCl, 1 mM MgCl₂, 1 mg/ml glucose, and 20 mM HEPES, pH 7.4), and added to electroporation cuvettes on ice containing 10-30 μ g of DNA plasmid in solution. Cuvettes were then pulsed using a Bio-Rad GenePulser Xcell (exponential decay, 280 V, 90 μ F). Cells were immediately resuspended in medium and plated in MatTek dishes prepared with fiducial markers. Medium was exchanged after 1 hour, and the cells were left in the incubator overnight for recovery and expression of the construct.

Sensitization, stimulation, and fixation

Cells were sensitized with 3 μ g/ml Dy654-labeled IgE in HEPES-buffered RBL medium (80% MEM, 20% fetal bovine serum, 50 mg/L gentamicin, and 30 mM HEPES) for 45 min at room temperature. Following sensitization, IgE-containing medium was replaced with warm RBL medium and left at 37°C for 5 min. For experiments involving latrunculin A or cytochalasin D treatment, cells were then incubated with 1 μ g/ml latrunculin or cytochalasin in medium for 5 additional minutes. The cells were then stimulated with multivalent antigen (500 ng/ml DNP-BSA in medium or 500ng/ml DNP-

BSA with 1 µg/ml latrunculin or cytochalasin in medium for latrunculin/cytochalasin treatments) for 0, 1, 3, 6, or 12 minutes at 37°C. Dishes were then rinsed with warm PBS and chemically fixed (4% paraformaldehyde and 0.1% glutaraldehyde in PBS) for 10 minutes at room temperature. The fix was then quenched with blocking buffer (10 mg/ml BSA in PBS) for 10 minutes. Fixed samples were rinsed three more times in blocking buffer before imaging. When imaging did not directly follow sample preparation, the samples were stored in blocking buffer with azide (10mg/ml BSA, 0.03% sodium azide in PBS) at 4 °C.

Phosphotyrosine immunolabeling

Phosphotyrosine was labeled in RBL-2H3, 1C1C8, and TB1A2 fixed samples using an anti-phosphotyrosine mouse monoclonal (clone 4G10) antibody. Cells were plated, sensitized, stimulated, and fixed as described above. After fixation and repeated rinsing with blocking buffer, dishes were incubated with a solution of the 4G10 antibody with TritonX-100 for cell permeabilization in blocking buffer (5 µg/ml 4G10 antibody, 0.1% TritonX-100, and 10mg/ml BSA in PBS) for 1 hour at room temperature. Dishes were rinsed five times with blocking buffer and incubated with A488-conjugated anti-mouse IgG2_b (10 µg/ml A488 anti-mouse antibody, 0.1% TritonX-100, and 10 mg/ml BSA in PBS) for 1 hour. Dishes were rinsed five times with blocking buffer before imaging or storage in blocking buffer with azide.

Super-resolution imaging

Imaging setup

Labeled samples were imaged on an inverted microscope (Leica DM-IRB, Wetzlar, Germany) under illumination through a 1.42 numerical aperture 100X Leica TIRF objective lens. The microscope is equipped with epi-fluorescence illumination via a mercury arc lamp as well as 50mW 405, 100W 488, 100mW 561nm, and 100mW 642 diode-pumped solid state lasers (Coherent, Santa Clara, CA) for TIRF imaging. Lasers are outfitted with cleanup filters (Chroma Technology Inc., Burlington, VT) and are attenuated with neutral density filters (ThorLabs, Newton, NJ) as needed for the illumination requirements of the experiment. Multi-bandpass excitation, polychroic, and emission filters (Chroma Technology Inc.) admit excitation from all four lasers and simultaneously pass emission from multiple channels. The emission path is coupled through a two-channel Optosplit emission splitter (Cairn Optics, Faversham, UK), which separates the channels onto two distinct regions of the camera CCD, enabling simultaneous recording of two color channels on the same camera. Images are recorded with an Andor iXon 897 EM-CCD camera (Andor, Belfast, UK) using custom image acquisition code written in Matlab (The MathWorks, Natick, MA).

Data acquisition

Fixed cells were imaged in the presence of an oxygen-scavenging and reducing imaging buffer (100mM Tris, 10mM NaCl, 10% w/w glucose, 500 µg/mL glucose-oxidase, 40µg/mL catalase, and 1% β-mercaptoethanol at pH 8.5). For mEos3.2/Dy654 two-color imaging, epi-fluorescence illumination was used to locate cells expressing mEos3.2 constructs in the green emission channel. Cells were selected based on moderate expression of the fluorescent construct, while highly overexpressing cells

were avoided. Once a transfected cell was selected, the illumination was switched to TIRF mode using the 561nm and 642nm lasers. mEos3.2 and Dy654 emission were simultaneously monitored using the Optosplit outfitted with a dichroic mirror and emission filters to split and isolate the red and far-red channels. Laser powers were then increased to induce photoswitching of Dy654 and enable imaging of mEos3.2. TIRF illumination intensity by the 405 laser was initiated and slowly increased to produce mEos3.2 photoswitching. Lasers were attenuated as needed to modulate the density of activated fluorescent probes as well as the probe emission intensity. Data from Dy654/A488 samples was collected using a similar approach, with illumination from 488 and 642 lasers and imaging in the green and far-red channels. For both Dy654/mEos3.2 and Dy654/A488 imaging, data were acquired at 32 frames per second with an exposure time of 10ms, with variable EM-CCD gain settings and illumination intensity. Data were acquired in a series of 500-frame movies. A given super-resolution image was reconstructed from at least 15 of these movies, or 7500 individual frames.

Analysis of imaging data

Channel alignment

Before and after imaging of each cell in a two-color experiment, images of an alignment sample were collected to enable precise registration of the two channels. This sample was prepared by incubation of a solution of Tetraspeck fluorescent nanospheres on the glass coverslip surface of a plasma-cleaned MatTek dish to achieve a dense random array of Tetraspecks. Tetraspecks contain multiple fluorescent dyes and emit in the blue, green, red-orange, and far-red channels. The alignment sample was imaged

with TIRF illumination simultaneously in the two color channels used for the imaging experiment. Approximately 75-100 images were collected as the alignment sample was translated across the microscope field of view. The images were separated in two, corresponding to the two color channels, and the diffraction-limited Tetraspecks were localized in each channel through least-squares fitting of their emission to a two-dimensional Gaussian function as described below for super-resolution image reconstruction. Because the same set of fluorescent nanospheres is imaged simultaneously in two color channels, localizations in each color channel that correspond to the same nanosphere could be identified. The set of paired localizations was used as a set of control points to infer a transformation that could spatially map one channel onto the other, allowing for registration of the super-resolution images collected in each channel. This transformation was obtained using the built-in MatLab function *cp2tform()* with the "local weighted mean" option for transformation calculation. Details of two-color alignment procedure are described in Appendix B.

Super-resolution image reconstruction

Super-resolution data were analyzed using routines that have been previously described in detail in (34, 35) and Chapter 2. Single-molecule probe emission was localized in movies of Dy654, mEos3.2, or A488 photoswitching by least-squares fitting of diffraction-limited spots to a two-dimensional Gaussian function. Outliers in spot intensity, aspect ratio, width, and fitting error are culled from the population of localizations. Localization of the same probe in sequential frames (defined by sequential localization within a distance of twice the localization precision) results in merging of the

two localizations. For registration of the two-color image, probe localizations in one color channel are transformed using the spatial transformation generated from the Tetraspeck alignment sample following the culling step. Image misalignment due to stage drift is corrected using the fiducial marker Tetraspecks that are adhered to the coverslip before the cells are plated. During super-resolution imaging, several fiducial markers in the field of view are tracked to determine displacement due to stage drift during super-resolution. Probe localizations in both channels are then corrected to prevent image offset caused by these displacements. The localization precision was calculated from correlation functions as described in (35). Typical values for the calculated localization precision were approximately 20 nm for the Dy654 probe, 23 nm for mEos3.2, and 25 nm for A488. The map of localizations that is used for further image analysis is generated through incrementing the pixel value at the coordinates where a given probe is localized, where the pixel size is set to be comparable to the image resolution. This image is convolved with a Gaussian filter for display. The number of localizations used to reconstruct a given fixed cell image varies based on factors such as labeling density in the case of the 4G10 images or expression levels in the case of mEos3.2 images, and differs inherently between probes due to differences in probe photophysics. Dy654 super-resolution images of IgE-FcεRI are generated from approximately 300,000 to 600,000 localizations, mEos3.2 images of Lyn or LifeAct are generated from 350,000 to 500,000 localizations, and A488 images of 4G10 are generated from 100,000 to 700,000 localizations.

Correlation function analysis of super-resolution images:

The distribution of proteins imaged in a super-resolution experiment is quantified through statistical analysis of the spatial map of localizations generated by the experiment. Pair auto- and cross-correlation functions are used to measure the extent of protein clustering and co-localization in super-resolution images. The specifics of this analysis are described in detail in (34), (35), and Chapter 2. In short, reconstructed super-resolution images are masked using the MatLab function *roipoly()* to isolate the cell membrane for further analysis and exclude edge effects. The autocorrelation function $g(r)$ is calculated using the Fast Fourier transforms (FFT) of the localizations within the mask normalized by the FFT of the mask itself. Cross-correlation functions are calculated from the FFT of masked regions in both color channels, again normalized by the FFT of the mask. Auto- and cross-correlation functions are interpreted as described in the Results and Discussion section.

Auto-correlation functions for super-resolution images of Dy654 IgE-FcεRI are corrected for the effects of protein over-counting as described in (34, 35) and Chapter 2. IgE auto-correlations are fit to the form:

$$g_{\text{meas}}(r) = g_{\text{PSF}}(r) * (1/\rho) + g_{\text{PSF}}(r) * g(r>0) \quad (1)$$

where the first term represents the contribution to $g_{\text{meas}}(r)$ of over-counting. The over-counting term arises from the value at $r=0$ of the correlation function of single molecule centers associated with labeled proteins of interest, which is inversely proportional to the density of proteins of interest ρ . This value at $r=0$ is convolved with g_{PSF} , the contribution to the correlation function that arises from the point spread function (or finite resolution) of the measurement, which is assumed to have a Gaussian form

$$g_{\text{PSF}}(r) = \exp\{-r^2/4\sigma^2\}/(4\pi \sigma^2).$$

g_{PSF} is estimated by comparing the auto-correlation of images reconstructed from all identified single molecule centers to those of images where localizations of probes identified in multiple sequential frames are merged as described previously (35). g_{PSF} is then fit to a two-dimensional Gaussian function to determine σ . We assume a surface density (ρ) of FcεRI to be 200 molecules/ μm^2 (43). The measured correlation function is then fit to Eqn 1 to determine the correlation function due to the real distribution of labeled molecules at r greater than 0, $g(r>0)$. $g(r>0)$ is approximated by an exponential function, $1+A\exp(-r/\xi)$ (35), and Eqn. 1 becomes:

$$g_{\text{meas}}(r) \approx \exp\{-r^2/4\sigma^2\}/(4\pi \sigma^2 \rho) + \exp\{-r^2/4\sigma^2\}/(4\pi \sigma^2) * [1 + (A\exp(-r/\xi))].$$

A and ξ are extracted as fit parameters.

Auto-correlation functions of Lyn-mEos3.2 are not corrected for over-counting due to uncertainty in density (ρ) of the transfected fluorescent fusion protein on the membrane. Instead, reported auto-correlations include contributions from over-counting and are fit to a single filtered exponential function that does not include a correction term for over-counting:

$$g_{\text{Fit}}(r) = g_{\text{PSF}}(r) * [1 + (A\exp(-r/\xi))] \quad (2)$$

where $g_{\text{PSF}}(r)$ is determined as described above from the auto-correlation function of probes localized in consecutive frames. Cross-correlation functions generated from two-color images do not contain artifacts from over-counting and are also fit to the filtered exponential function, Eqn 2.

Absolute values of the cross-correlation amplitude are measurements of the relative co-enrichment of two species with respect to the average density of each species on the membrane. It is possible that overexpression of fluorescent constructs

such as Lyn-mEos3.2 could lead to a situation where the overall average density of Lyn is higher without a proportional increase in the amount of Lyn interacting with IgE-FcεRI. A similar effect could be generated by additional 4G10 labeling density caused by non-specific binding of the 4G10 primary or fluorescent secondary antibodies. If this is the case, then our measurements may underestimate cross-correlation amplitudes. We have attempted to mitigate these possible effects by selecting transfected cells with consistent, moderate expression levels and by choosing immunolabeling conditions that minimize non-specific antibody labeling. Additionally, we can make direct comparisons of correlation function amplitudes between samples that were labeled in the same way (e.g. either by 4G10 labeling or by Lyn-mEos3.2 transfection) because the effects of labeling on the correlation function are the same.

RESULTS AND DISCUSSION

Two-color super-resolution imaging measures spatial co-localization of IgE-FcεRI and Lyn kinase

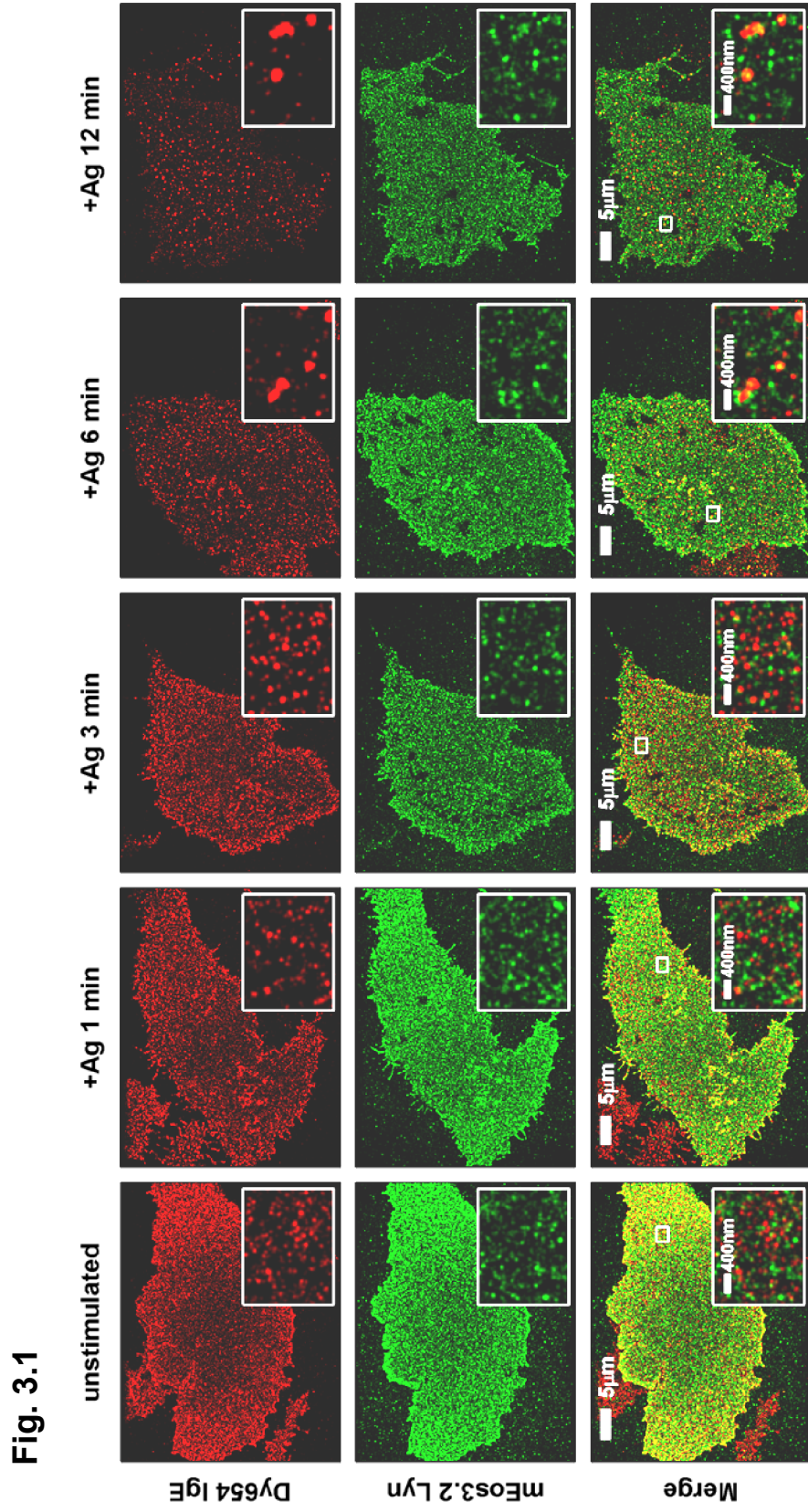
Using two-color super-resolution microscopy, we are able to characterize the nanoscale coupling of Lyn kinase with IgE-FcεRI receptor complexes as a function of receptor cross-linking with the multivalent antigen DNP-BSA. To label these two proteins of interest, we use a combination of an organic fluorophore and a transfectable fluorescent fusion protein. Dinitrophenyl (DNP)-specific IgE is directly conjugated with the far-red dye Dyomics 654 (Dy654) and used to sensitize RBL-2H3 cells that have been transiently transfected with a fluorescent construct consisting of mEos3.2 fused to

the C terminus of Lyn, which is expressed in addition to endogenous Lyn. Cells are stimulated with DNP-BSA for defined time intervals before chemical fixation and super-resolution imaging as described in the Materials and Methods. For these fixed-cell imaging experiments, we are able to achieve lateral resolution of approximately 20nm for Dy654 and 25nm for mEos3.2.

Fig. 3.1 shows super-resolution images of IgE-bound to Fc ϵ RI (shown in red) and Lyn (shown in green) in whole cells and magnified regions (insets) for representative cells stimulated for 0, 1, 3, 6, and 12 minutes. Examining the far-red Dy654-IgE channel alone, we see that the distribution of IgE-Fc ϵ RI clearly changes with stimulation time. IgE-Fc ϵ RI accumulates into clusters beginning at the 1 min stimulation time point that become more pronounced with continued exposure to antigen. After 12 minutes, the majority of receptors on the membrane are organized in dense clusters. Conversely, there is no obvious antigen-dependent rearrangement of Lyn observed in the mEos3.2 channel.

The distributions of IgE-Fc ϵ RI in unstimulated cells and Lyn at all stimulation timepoints appear weakly clustered in single color super-resolution images. Individual labeled proteins are over-counted in these experiments, leading to the visual impression of clusters in super-resolution images. This artifact arises whenever a single protein of interest can be labeled with multiple fluorescent molecules, either through direct conjugation of multiple dyes, binding of primary and secondary antibodies, or when single fluorescent molecules can be localized multiple times during data collection due to reversible photoswitching. In this case, IgE is labeled with an average of 2.7 Dy654 molecules during dye conjugation, and both Dy654 and mEos3.2 are known to blink

Fig. 3.1 Two-color super-resolution imaging measures distributions of IgE receptor and Lyn as a function of antigen stimulation. Cells expressing Lyn-mEos3.2 and sensitized with Dy654 IgE are stimulated with 500ng/ml DNP-BSA for 0, 1, 3, 6, or 12 min, fixed, and imaged as described in the Materials and Methods. Representative cell images are shown for each stimulation time point, including the Dy654 super-resolution image represented in red (top row), the mEos3.2 image in green (middle row), and the overlaid image (bottom row). Regions indicated by white boxes are magnified in the insets. The map of single-probe localizations obtained through super-resolution imaging is convolved with two-dimensional Gaussian functions with radii of 50nm in whole images and 20nm in insets for display.



reversibly. These effects are commonly encountered with most super-resolution localization techniques, and we expect some degree of artifactual clustering to appear in super-resolution images (35).

Alignment of the two color channels allows precise registration of protein distributions in each channel, and we determine typical registration errors to be approximately 10-15nm. The alignment procedure is described in the Materials and Methods and Appendix B. Merged images in Fig. 3.1 show the relative distributions of IgE-Fc ϵ RI and Lyn. We can identify fields of view in images of stimulated cells where receptor clusters co-localize with concentrated areas of Lyn, but overall the effect of antigen stimulation on Lyn/IgE-Fc ϵ RI co-localization is too subtle to interpret by eye.

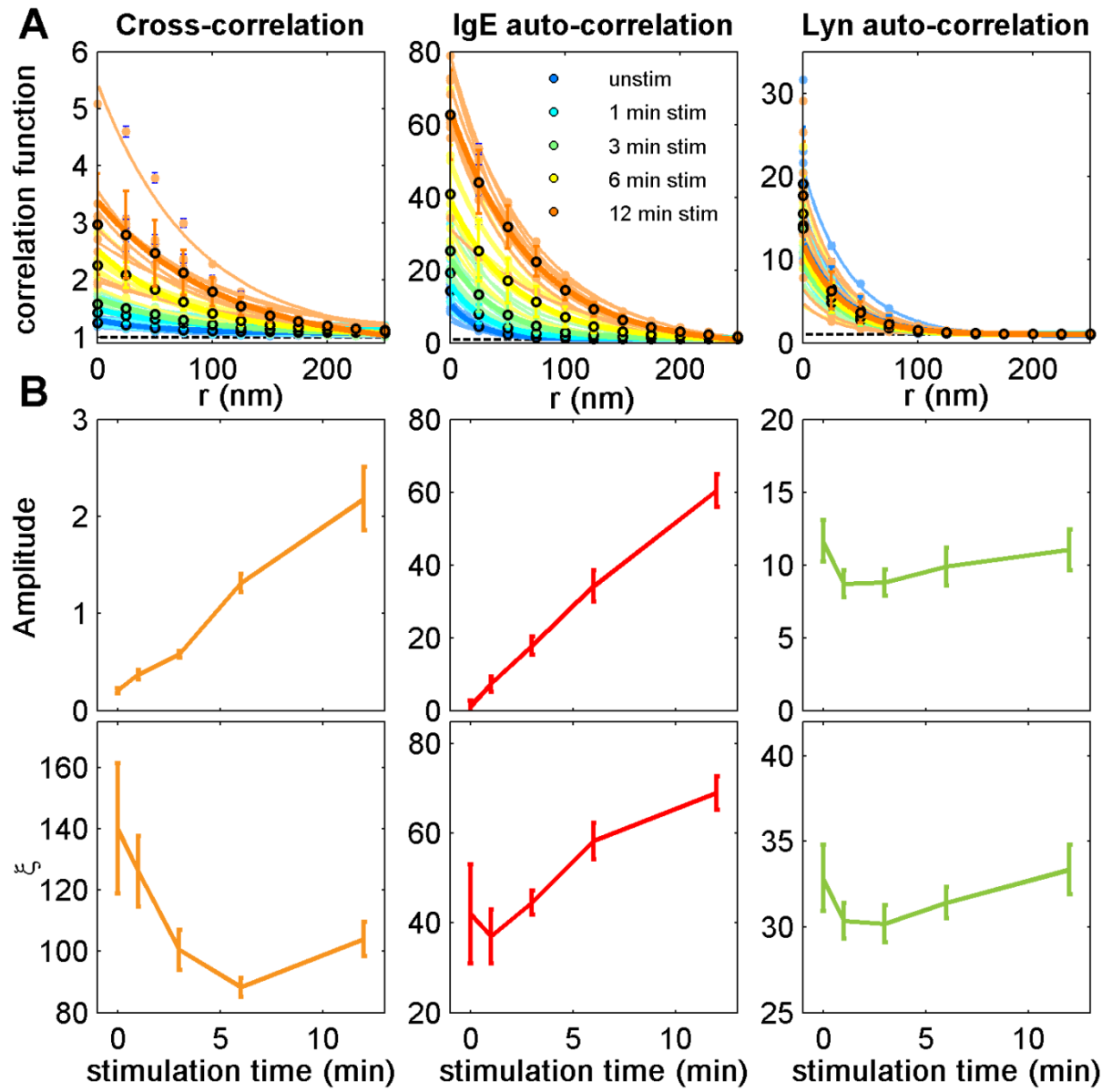
Instead, we turn to a quantitative method, pair-correlation analysis, to characterize the organization of IgE-Fc ϵ RI and Lyn and measure their co-localization. Pair-correlation functions are calculated from the spatial map of single-molecule localizations collected in super-resolution images. The pair-correlation function measures the normalized probability of finding another probe a radius r away from a given probe and is averaged over all probes. Pair auto-correlation functions measure this probability for two like probes, in this case two probes in the same color channel, whereas cross-correlation functions measure this probability for probes of two different colors in a two-color image. A random distribution of probes yields a correlation function equal to 1 at all radii. When probes are clustered, they are spatially correlated at short distances, and the correlation function takes on values larger than 1 at small radii. Likewise, when two distinguishable species are co-clustered, their cross-correlation function is larger than 1 at radii that correspond to size of correlated structures. We use

methodology for calculating and analyzing pair correlation functions that has been described in detail in past studies and was recently used to quantify single-color images of IgE-Fc ϵ RI (34, 35).

Cross-correlation functions calculated from multiple two-color images of IgE-Fc ϵ RI and Lyn at each of the stimulation timepoints are shown in Fig. 3.2 A. The value of cross-correlation functions at small radii are larger at longer stimulation times, indicating that co-localization of Lyn with IgE-Fc ϵ RI increases with stimulation time. Cross-correlation functions are fit to a single filtered exponential function (Eqn. 2) as described in the Materials and Methods. The amplitude and correlation length (ξ) of the exponential fit to the cross-correlation function of the exponential fit are extracted. The amplitude quantifies the co-enrichment of the two species in correlated structures relative to their average density on the membrane. It measures the increased probability of finding one species co-localized with the other in clusters compared to a random relative distribution. ξ , the correlation length, is a measurement of the average radius of correlated structures. Fits are shown with cross-correlations plotted in Fig. 3.2, A.

Auto-correlations are also tabulated to measure changes in IgE-Fc ϵ RI and Lyn distributions upon antigen addition (Fig. 3.2 B). When over-counting is present in super-resolution images, the auto-correlation function contains a contribution from over-counting on the length scale of the localization precision of the fluorescent probe (approximately 20 nm), unlike cross-correlations, which are unaffected by over-counting (35). IgE-Fc ϵ RI autocorrelations are fit to Eqn. 1, which includes terms that correct for over-counting as has been described previously (34, 35) and as outlined in the Materials and Methods. Lyn auto-correlations are not corrected due to inherent

Fig. 3.2 Pair-correlation analysis shows stimulation time-dependent nanoscale co-localization of IgE-FcεRI and Lyn. Individual and average pair-correlation functions (A) and average fit parameters (B) for the set of Lyn-mEos3.2 and Dy654 IgE images collected of cells stimulated for 0, 1, 3, 6, or 12 min as in Fig. 3.1. (A) Individual Lyn/IgE-FcεRI cross-correlation functions (left), IgE-FcεRI auto-correlation functions (middle), and Lyn auto-correlation functions (right) calculated from two-color images, Dy654 images, and mEos3.2 images, respectively, are plotted with fits. Individual Lyn/IgE-FcεRI cross-correlation functions and Lyn auto-correlation functions are fit to Eqn. 2, $g_{\text{fit}}(r) = g_{\text{PSF}}(r) * [1 + (A \exp(-r/\xi))]$, where g_{PSF} is determined from the resolution of the measurement as described in the Materials and Methods. The measured IgE-FcεRI autocorrelations shown are fit to Eqn. 1, $g_{\text{meas}}(r) = \exp\{-r^2/4\sigma^2\}/(4\pi \sigma^2 \rho) + g(r>0) * g_{\text{PSF}}(r)$. The first term includes contributions from over-counting. σ , ρ , and g_{PSF} are determined as described in the Materials and Methods, and $g(r>0)$ is approximated with the exponential function, $1 + A \exp(-r/\xi)$. Fits of these individual auto- and cross-correlation functions to Eqns. 1 or 2 are used to extract the fit parameters A (Amplitude) and ξ for each correlation function. Average correlation functions for the group of cells at each time point ($n=8$ or 9 for each time point) and are plotted in black-outlined circles. The fit of average correlation functions to Eqn. 1 or 2 for IgE auto-correlations or Lyn/IgE-FcεRI cross correlations and Lyn auto-correlations, respectively, are plotted in bold lines. (B) Fit parameters Amplitude and ξ generated by the fit of individual Lyn/IgE-FcεRI cross-correlation functions (left), IgE-FcεRI auto-correlation functions (middle), and Lyn auto-correlation functions (right) are averaged and plotted as a function of stimulation time. Error bars represent SEM.



uncertainties in the density of the transfected construct on the membrane and cannot be fit to Eqn. 1. Instead, Lyn auto-correlation functions are fit without over-counting correction to Eqn. 2 but are likely dominated by over-counting artifacts at radii less than approximately 30 nm, which leads to large overestimates of the value of the amplitude and underestimates of ξ when the data are fit. Nonetheless, we report Lyn auto-correlation function fit parameters to Eqn. 2 for comparison of values before and after antigen stimulation.

Cross- and auto-correlation functions are calculated for IgE-Fc ϵ RI and Lyn in multiple cells at each stimulation time point and fit parameters are extracted. The amplitude and ξ are averaged for each time point to generate mean values as a function of stimulation time. Average amplitude and ξ are shown for IgE-Fc ϵ RI/Lyn cross-correlation functions and for IgE-Fc ϵ RI and Lyn autocorrelation functions in Fig. 3.2. In unstimulated cells, IgE-Fc ϵ RI and Lyn appear weakly cross-correlated at relatively long distances, illustrated by small values of amplitude and large values of ξ . After stimulation, the amplitude of cross-correlations increases in a time-dependent manner and the correlation length falls, indicating that correlated structures of IgE-Fc ϵ RI and Lyn become smaller and denser. The increase in amplitude with stimulation time observed here by localization microscopy shows a similar trend as cross-correlation amplitudes obtained in a previous study using scanning electron microscopy, although in that case cross-correlation amplitudes are systematically larger (9). This could be due to differences in the dorsal membrane imaged in SEM studies and the ventral surface of the cell, in terms of the kinetics or extent of formation of large co-clusters of IgE-Fc ϵ RI and Lyn. The fact that different labeling schemes were used for these two experiments,

which include expression of non-endogenous Lyn in super-resolution imaging experiments, could also account for quantitative differences in the measured cross-correlation. The IgE-Fc ϵ RI auto-correlation amplitude increases with stimulation time, consistent with the visual impression of increased cluster density from super-resolution images of IgE-Fc ϵ RI and with previously published characterization of receptor clustering (34). ξ increases on average with stimulation time, similar to what we have seen previously in single-color fixed cell experiments (34). Lyn autocorrelation amplitude and ξ do not exhibit robust stimulation-dependent changes, possibly because Lyn auto-correlations are dominated by over-counting artifacts that are independent of cell stimulation, or because higher levels of Lyn expression obscure subtle differences in the distribution of Lyn associated with IgE-Fc ϵ RI. Together measurements of cross- and auto-correlation fit parameters describe a conversion from weak Lyn/IgE-Fc ϵ RI co-localization that occurs over long length scales before antigen addition to co-localization of a sub-population of Lyn with cross-linked IgE receptor that grows with stimulation time as antigen-stimulated receptor clusters become increasingly dense.

We observe a sustained increase in Lyn/Fc ϵ RI co-localization over 12 minutes of antigen stimulation. Previous immunoprecipitation-based biochemical experiments that measured the time course of antigen-stimulated association of Lyn with Fc ϵ RI and resulting changes in Lyn kinase activity showed a rapid increase in Lyn bound to Fc ϵ RI that peaks within one or two minutes of antigen stimulation, followed by a gradual decline (7, 44). On the other hand, studies that use standard confocal or multiphoton microscopy do not detect Lyn/Fc ϵ RI co-localization until after at least 10 minutes of antigen stimulation (10, 29). A possible explanation for this discrepancy is that these

optical methods are insensitive to Lyn/IgE co-localization that occurs on length scales well below the diffraction limit, whereas biochemical methods utilize chemical cross-linkers and immunoprecipitation that may not detect Lyn that is not directly or stably bound to FcεRI. Our improved resolution compared to other optical techniques enables detection of co-localization that takes place on length scales in the tens of nanometers. As a consequence, we are able to measure Lyn/IgE-FcεRI co-localization that occurs on the less than 5 min time scale of association reported by cross-linking and immunoprecipitation (7). Lyn coupling to clustered IgE-FcεRI at these short stimulation times has been shown by electron microscopy experiments (9, 36), but because of the sub-diffraction dimensions of these structures, detection of Lyn association at early times after stimulation has so far been a challenge for fluorescence imaging approaches. At the same time, we observe cross-correlations at longer stimulation times (12 min). The biochemical immunoprecipitation data indicates that Lyn is not directly associated with FcεRI at the plasma membrane at these longer stimulation times. Comparison to our results suggests that the association we observe is mediated by less specific interactions, possibly through lipid-mediated membrane domains.

The initiation of signaling correlates with Lyn/IgE-FcεRI spatial co-localization

Our results demonstrate that this approach using super-resolution imaging and cross-correlation function analysis are effective at measuring antigen-stimulated co-redistribution of Lyn with clustered IgE-FcεRI. To determine whether the Lyn/IgE-FcεRI cross-correlation that we observe is concurrent with a functional response, we extend our approach to measure tyrosine phosphorylation correlated with FcεRI before and

after cross-linking by antigen. Receptor phosphorylation is a consequence of Lyn association with cross-linked receptors and is an early step in the signaling cascade. Cells are sensitized with Dy654 IgE, stimulated, and fixed as in Lyn/IgE-Fc ϵ RI two-color experiments above. Phosphotyrosine on the plasma membrane is then labeled using the anti-phosphotyrosine antibody clone 4G10 followed by an AlexaFluor 488 (A488)-labeled secondary antibody. Fig. 3.3 A shows representative super-resolution images of Dy654 IgE and A488 anti-phosphotyrosine 4G10 in an unstimulated cell and a cell stimulated for 6 min. In unstimulated cells, 4G10 signal can be attributed to basal phosphorylation and non-specific background labeling. IgE and phosphotyrosine do not appear cross-correlated in unstimulated cells, but in stimulated cells, there is a clear concentration of 4G10 label in areas that spatially correspond with IgE-Fc ϵ RI clusters.

We quantify the labeling of IgE-Fc ϵ RI clusters with 4G10 by calculating their cross-correlation function. We interpret changes in 4G10/IgE-Fc ϵ RI cross-correlation amplitudes to reflect changes in the absolute amount of tyrosine phosphorylation localized to receptor clusters. 4G10/IgE-Fc ϵ RI cross-correlations follow similar trends as a function of stimulation time as Lyn/IgE-Fc ϵ RI cross-correlation functions (Fig. 3.3 B). Prior to antigen stimulation, cross-correlation functions fit to Eqn. 2 have very small amplitudes, close to 0, and long correlation lengths over 300nm, suggesting a nearly random relative distribution of 4G10 and IgE receptor. In stimulated cells, the amplitude increases steadily, with time dependence similar to that of the Lyn/IgE-Fc ϵ RI cross-correlation amplitude. ξ quickly drops with stimulation to values that match Lyn/IgE-Fc ϵ RI correlation lengths.

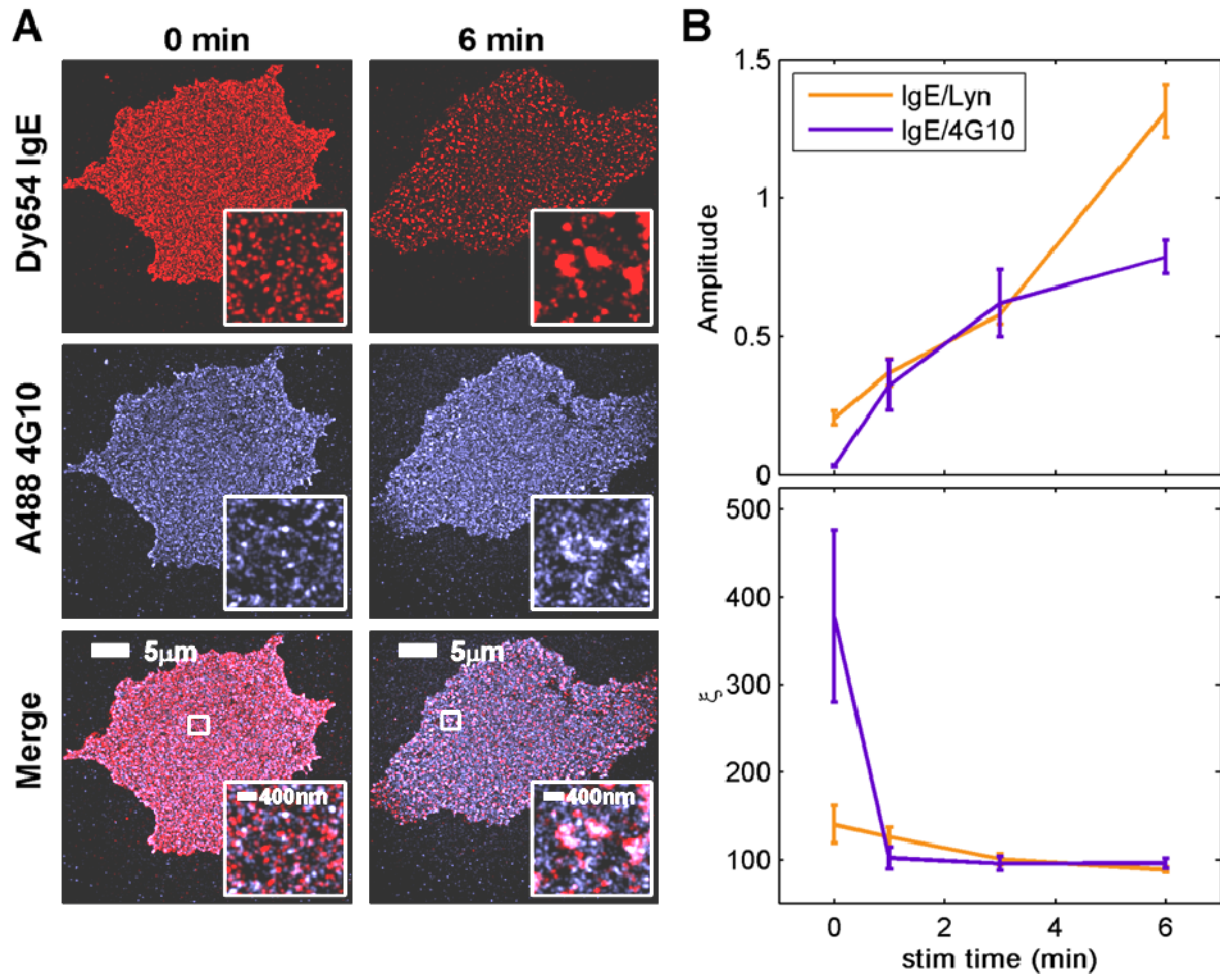


Fig. 3.3 4G10/IgE-Fc ϵ RI cross-correlation amplitude increases with stimulation time. (A) Two-color super-resolution fixed cell images of A488 4G10 immunolabeled phosphotyrosine and Dy654 IgE in cells stimulated for 0 min (left) or 6 min (right). Regions indicated by white boxes are magnified in the insets. The map of single-probe localizations obtained through super-resolution imaging is convolved with two-dimensional Gaussian functions with radii of 50nm in whole images and 20nm in insets for display purposes. (B) Cross-correlation fit parameters Amplitude and ξ as a function of stimulation time for A488 4G10/Dy654 IgE-labeled cells that were stimulated for 0, 1, 3, or 6 min. averaged over multiple cells for each timepoint (n = 6 cells per timepoint for A488 4G10/Dy654 IgE experiments and n=8 or 9 cells per timepoint for Lyn-mEos3.2/Dy654 IgE experiments). Lyn/IgE-Fc ϵ RI cross-correlation function fit parameters are also plotted and were reproduced from Fig. 3.2.

Thus, receptor-localized phosphotyrosine and receptor-localized Lyn are organized in structures that are both spatially correlated with IgE-FcεRI clusters, that have similar dimensions, and that form with similar time dependence after addition of antigen. Comparison of 4G10/IgE and Lyn/IgE cross-correlation function parameters as a function of stimulation time implies a positive correlation between the co-localization of Lyn with cross-linked IgE-FcεRI and phosphorylation of receptor clusters that we observe in separate imaging experiments. These results are consistent with the view that Lyn association with FcεRI precedes or occurs concurrently with the initiation of receptor phosphorylation, as was earlier suggested by immunoprecipitation experiments (7, 8). Moreover, our results show that increasing 4G10/IgE-FcεRI cross-correlation amplitudes can be interpreted as a functional consequence of Lyn/IgE-FcεRI co-localization. 4G10/IgE-FcεRI cross-correlation functions measure the catalytic activity of Lyn, whereas Lyn/IgE-FcεRI cross-correlation functions measure the stoichiometric accumulation of Lyn with FcεRI. However, we do note that, due to the ubiquity of tyrosine phosphorylation sites on signaling molecules, we do not measure receptor phosphorylation specifically in this experiment. Phosphotyrosines labeled by 4G10 could belong to ITAMs on FcεRI or to signaling molecules that co-redistribute with clustered receptors, including LAT, Syk, or Lyn itself (9). Thus, stimulation-induced increases in receptor-correlated phosphotyrosine consist of contributions from receptor phosphotyrosine as well as receptor-associated signaling molecules that are also phosphorylated in an antigen-dependent fashion. The fact that 4G10 is not specific to receptor phosphotyrosine may account for the differences that we observe in the time dependence of 4G10/IgE-FcεRI co-localization and past measurements of FcεRI β and

γ chain phosphorylation by Western blot, which have shown transient behavior where receptor phosphorylation peaks within a few minutes and decays (15, 26, 45, 46).

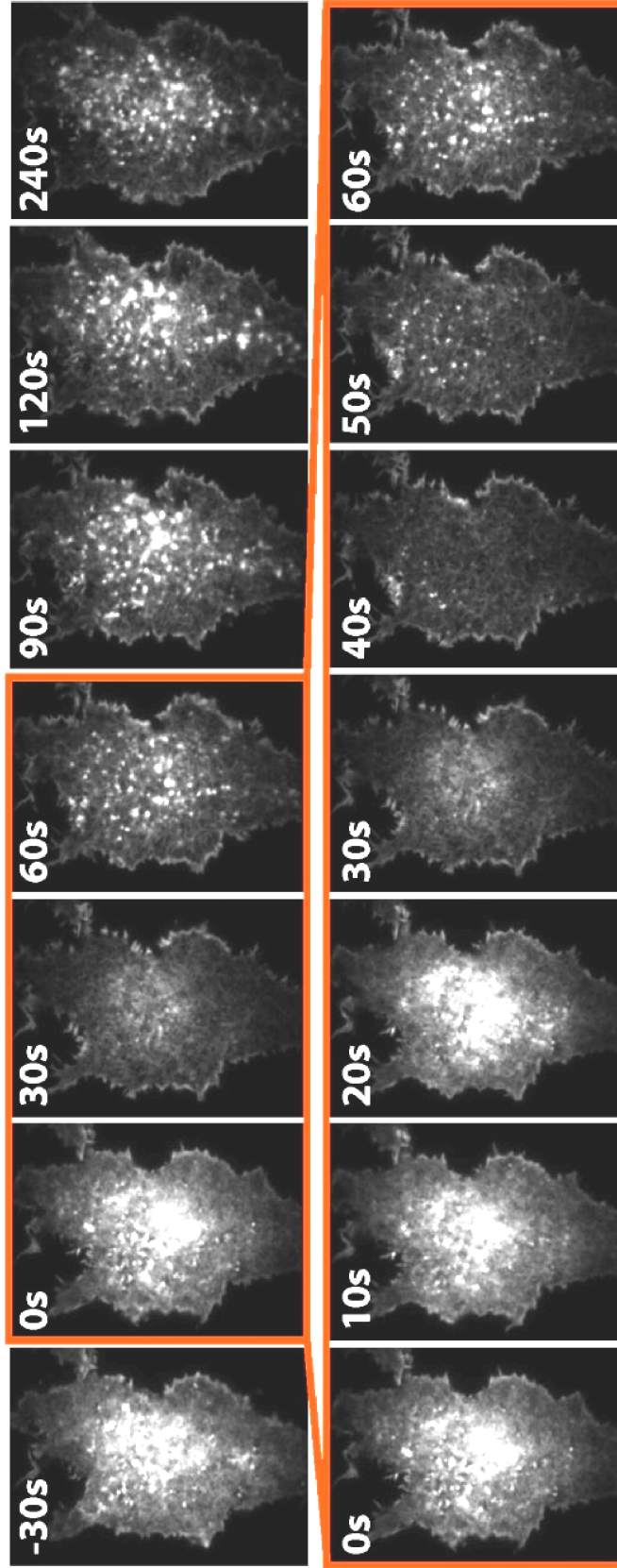
In principle the absolute values of cross-correlation amplitudes for 4G10/IgE-FcεRI and Lyn/ IgE-FcεRI can be compared directly to evaluate differences in the degree of co-enrichment of 4G10 and Lyn with clustered receptors. In doing so, it is important to keep in mind that correlation amplitudes represent a relative enrichment of 4G10 or Lyn with clustered receptors compared to the average surface density of these species. Any effect that increases the average density of label without necessarily increasing receptor-localized label, such as detection by 4G10 antibodies of other phosphorylation events accompanying signaling that are not co-localized with clustered receptors, could have the effect of decreasing the cross-correlation amplitude. With this in mind, we focus on comparison of the time dependence of stimulated changes in Lyn/ IgE-FcεRI and 4G10/ IgE-FcεRI cross-correlation amplitudes.

The actin cytoskeleton is dynamic during early stages of cell activation, but bulk association with IgE receptors does not detectably change with stimulation.

Numerous previously published studies have demonstrated a role for actin in the regulation of FcεRI signaling, and antigen-stimulated actin polymerization has been well documented (21, 25, 47, 48). Live cell TIRF imaging of cortical actin labeled through transient transfection with EGFP fused to LifeAct, an F-actin binding peptide, also shows that cortical actin undergoes dramatic remodeling at the ventral surface of RBL-2H3 cells shortly after antigen stimulation (Fig. 3.4). Prior to antigen addition, actin is distributed across the ventral surface with some areas of punctuate actin concentration.

Fig. 3.4 Cortical actin undergoes dynamic reorganization in the first minutes after antigen addition. Live cell TIRF imaging of an RBL-2H3 cell transfected with LifeAct GFP shows antigen-induced changes in the cortical actin cytoskeleton. Cells were imaged at approximately 35°C. The time in seconds after addition of 500ng/ml DNP-BSA is shown for each image, where antigen is added at $t = 0$ s. Before stimulation, actin fluorescence is distributed across the footprint of the cell, with some areas of higher concentration punctuate actin structures. Around 30sec after stimulation, the actin signal is depleted from the ventral surface across most of the cell footprint , however the cell periphery is relatively enriched in polymerized actin. Within 1 minute after antigen addition, punctate actin structures reappear and become more numerous over the course of the next several minutes. An expanded series of images depicting the first 60 seconds after antigen addition clearly shows the rapid depletion of cortical actin from the ventral membrane followed by the development of actin puncta.

Fig. 3.4

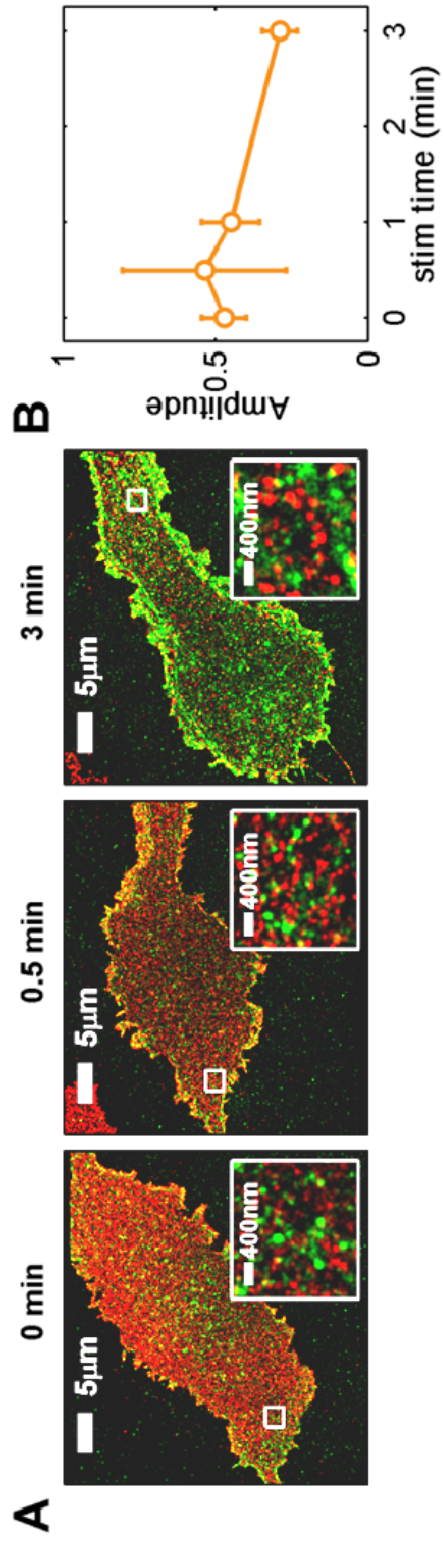


Approximately 30 seconds after antigen is added, actin fluorescence rapidly disappears from the ventral surface, leaving a weak, relatively uniform signal on the interior of the cell footprint with a slight concentration of actin around the periphery. Within 60 seconds, actin puncta begin to reappear. Puncta increase in number over the course of the next minute and form and vanish dynamically. Actin puncta continue to form and disappear over the course of the next few minutes as the cell spreads.

TIRF imaging is consistent with previous findings that the F-actin content of detergent-extracted membranes decreases during approximately the first 30 seconds after antigen addition, then increases beyond pre-stimulation levels (21). This striking antigen-stimulated actin remodeling that occurs soon after antigen addition may be involved in regulating signaling at these early stimulation times. However, we do not detect stimulated co-localization of labeled actin structures with IgE-Fc ϵ RI clusters by 2-color TIRF (data not shown) or super-resolution imaging (Fig. 3.5). IgE-Fc ϵ RI association with labeled actin is weak before antigen stimulation and remains weak at time points corresponding to depolymerization of actin at the ventral surface (30s) and formation of actin puncta (60s and 3 min). This could be because actin does not directly couple to clustered Fc ϵ RI after stimulation or because the fraction of actin that does so is small enough to be undetectable in our experiment. Although previous imaging studies show co-localization of F-actin with cross-linked IgE (10, 26, 49), in these cases large regions of cross-linked IgE-Fc ϵ RI were stabilized on the membrane and co-localization could be mediated through some other membrane species. Actin was shown to co-cluster with Lyn 2 minutes following antigen stimulation in electron microscopy experiments (36), although these studies have some limitations in their

Fig. 3.5 Antigen-stimulated coupling of IgE-Fc ϵ RI to actin is not readily detectable by two-color super-resolution imaging. (A) Representative two-color images of Dy654 IgE and mEos3.2 LifeAct in cells stimulated for 0 (left), .5 (middle), or 3 (right) min. Regions indicated by white boxes are magnified in the insets. The map of single-probe localizations obtained through super-resolution imaging is convolved with two-dimensional Gaussian functions with radii of 50nm in whole images and 20nm in insets for display purposes. (B) Average amplitude of the fit to Eqn. 2 of cross correlation functions of LifeAct/IgE-Fc ϵ RI images as a function of stimulation time (n = 4 or 5 cells for each time point). Error bars represent SEM.

Fig. 3.5



interpretation due to sample preparation using membrane sheets that are ripped from intact adherent cells, which may perturb cytoskeletal interactions. Further, receptor phosphorylation by Lyn, which also occurs during the first stages of the signaling response concurrent with actin remodeling, is sensitive to actin polymerization (25, 26, 28). Actin could regulate antigen-induced signaling via its direct or indirect interactions with Lyn by controlling the localization of Lyn on the membrane. We test this hypothesis in super-resolution imaging experiments.

The actin cytoskeleton regulates stimulated coupling of Lyn to IgE-FcεRI.

The regulation of antigen-stimulated degranulation by the actin cytoskeleton is likely to be mediated through a number of signaling molecules including Lyn. We evaluate the effects of the actin cytoskeleton on the regulation of Lyn/IgE-FcεRI coupling in super-resolution experiments where cells are treated with drugs that disrupt actin polymerization. Samples are prepared for Lyn-mEos3.2/ Dy654 IgE 2-color imaging as described above, with the addition of a 5-min incubation with 1 μM cytochalasin or latrunculin preceding antigen stimulation in the presence of the actin-disrupting drug. Two-color super-resolution images of cells stimulated for 6 min in the presence and absence of latrunculin or cytochalasin (Fig. 3.6, A) do not show obvious differences in Lyn/IgE-FcεRI co-localization. However, comparison of Lyn/IgE-FcεRI cross-correlations for the various treatment conditions as a function of stimulation time reveal that Lyn/IgE-FcεRI interactions are enhanced when actin polymerization is inhibited (Fig. 3.6, B). Latrunculin and cytochalasin inhibit actin polymerization by different mechanisms, latrunculin sequesters actin monomers while cytochalasin caps

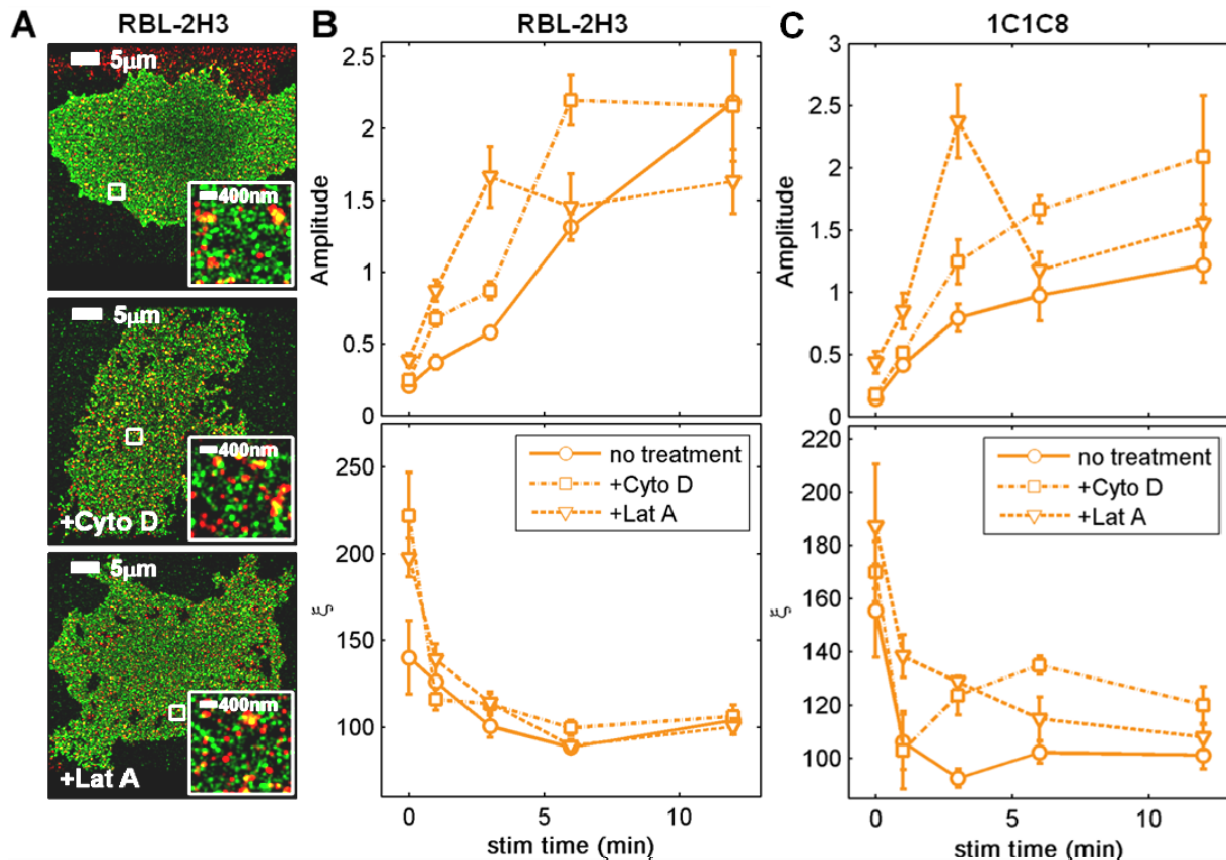


Fig. 3.6 Inhibition of actin polymerization enhances Lyn/IgE-Fc ϵ RI cross-correlation amplitude. Representative Lyn-mEos3.2/Dy654 IgE two-color super-resolution images (A) and average cross-correlation function fit parameters for fits to Eqn. 2 (B, C) for cells that were stimulated for 0, 1, 3, 6, or 12 min with and without pre-treatment with 1 μM latrunculin or cytochalasin and stimulation in the presence of the drug. (A) Representative images of cells stimulated for 6 min without (top) or with treatment with cytochalasin (middle) or latrunculin (bottom). (B) Lyn/IgE-Fc ϵ RI cross-correlation fit parameters Amplitude and ξ as a function of stimulation time for RBL-2H3 cells expressing Lyn-mEos3.2 and sensitized with Dy654 IgE that were stimulated for 0, 1, 3, 6, or 12 min with and without treatment with actin-disrupting drugs. Fit parameters are averaged over multiple cells for each timepoint ($n=8$ or 9 cells per timepoint for untreated cells, $n = 9$ cells per timepoint for cytochalasin-treated cells, and $n = 7$ cells per timepoint for latrunculin-treated cells). Lyn/IgE-Fc ϵ RI cross-correlation function fit parameters are also plotted and were reproduced from Fig. 3.2. Error bars denote SEM. (C) Average cross-correlation function fit parameters for 1C1C8 cells labeled, treated (or not) with cytochalasin or latrunculin, and stimulated under the same conditions as RBL-2H3 cells in (B). $n = 7$ cells per timepoint for all treatment conditions. Error bars denote SEM.

the barbed end of filaments, and these two drugs have slightly different effects on stimulated Lyn/IgE- Fc ϵ RI cross-correlations. Cytochalasin treatment causes a sustained enhancement of cross-correlation amplitudes for the first 6 minutes after stimulation. Enhancement due to latrunculin is more short-lived, extending through 3 min, but is also larger in magnitude at this time point. Interestingly, latrunculin also causes a small but significant increase in Lyn/IgE-Fc ϵ RI interaction in unstimulated cells as measured by the cross-correlation amplitude. Lyn and IgE-Fc ϵ RI are weakly correlated over longer distances in unstimulated cells for both cytochalasin and latrunculin treatments as indicated by ξ , which is increased compared to untreated cells. In stimulated cells, Lyn/IgE correlated structures have similar dimensions regardless of cytoskeletal perturbation, i.e., ξ is not significantly different in treated vs. untreated cells. Inhibition of actin polymerization does not seem to have robust effects on IgE-Fc ϵ RI or Lyn autocorrelations, except for a slight enhancement of IgE- Fc ϵ RI autocorrelations, which are shown in Fig. (3.7, A).

Evidence from ours and previous studies suggests that the modulation of the spatial distribution of Lyn can be a mechanism for actin regulation of stimulated responses in mast cells. Pervanadate is a pharmacological inhibitor of tyrosine phosphatases that stimulates degranulation responses which bypass receptor clustering by activating kinases, including Lyn. Latrunculin has no effect on pervanadate-stimulated degranulation (25), which shows that latrunculin acts upstream of receptor phosphorylation. Although cytochalasin does have some effects on downstream signaling evidenced by its enhancement of pervanadate stimulation, its effects on early signaling are similar to latrunculin (25, 28). Under the stimulation conditions used here,

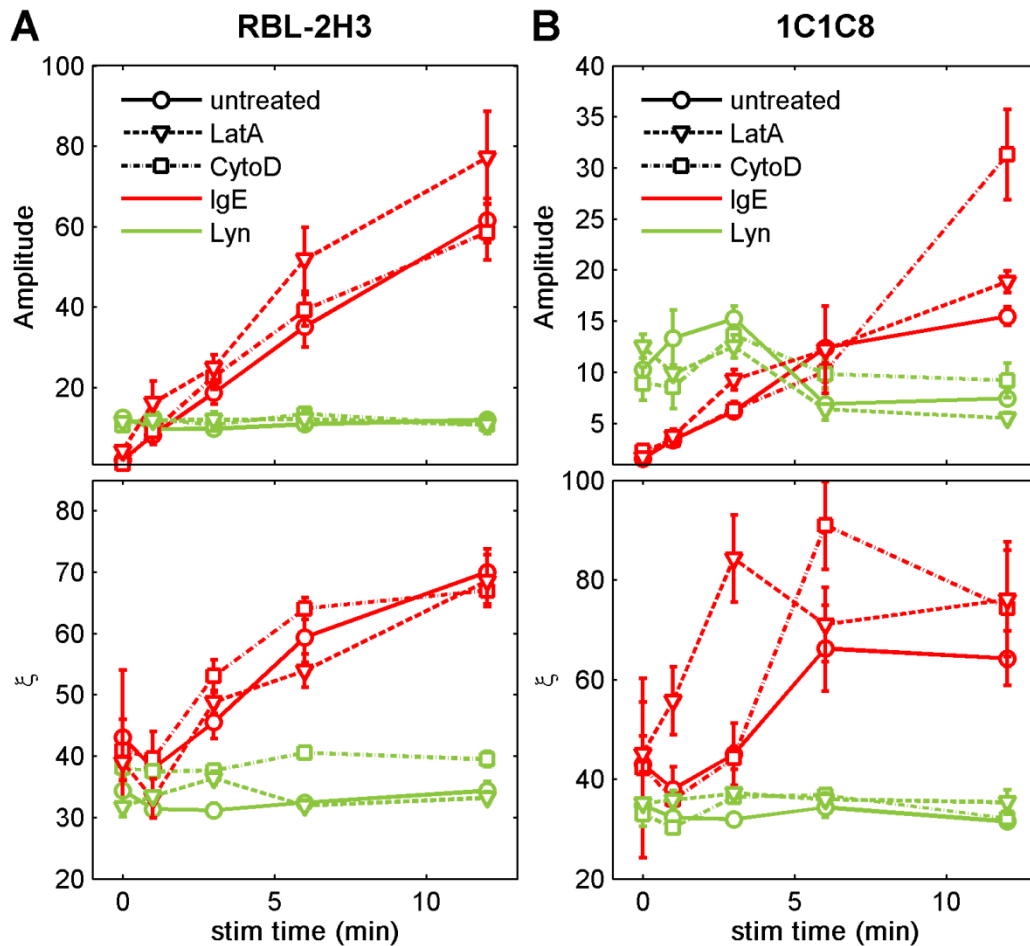


Fig. 3.7 Lyn mEos3.2 and Dy654 IgE auto-correlation fit parameters for cells treated with actin polymerization inhibitors. Average auto-correlation function fit parameters Amplitude and ξ extracted from fits to Eqn. 1 for IgE auto-correlation functions and Eqn. 2 for Lyn auto-correlation functions as a function of stimulation time for the cells whose average cross-correlation function fit parameters are shown in Fig. 3.6. (A) Average Lyn and IgE-Fc ϵ RI auto-correlation function fit parameters for RBL-2H3 cells expressing Lyn-mEos3.2 and sensitized with Dy654 IgE that were stimulated for 0, 1, 3, 6, or 12 min with and without treatment with actin-disrupting drugs. Fit parameters are averaged over multiple cells for each timepoint ($n=8$ or 9 cells per timepoint for untreated cells, $n = 9$ cells per timepoint for cytochalasin-treated cells, and $n = 7$ cells per timepoint for latrunculin-treated cells). Error bars denote SEM. (B) Average auto-correlation function fit parameters for 1C1C8 cells labeled, treated (or not) with cytochalasin or latrunculin, and stimulated under the same conditions as RBL-2H3 cells in (A). $n = 7$ cells per timepoint for all treatment conditions. Error bars denote SEM.

enhanced Lyn recruitment occurs in actin-disrupted RBL-2H3 cells without robust changes in IgE-Fc ϵ RI autocorrelations, indicating that latrunculin and cytochalasin do not affect receptor oligomerization caused by antigen stimulation under these conditions. Given that Lyn itself remains in an enzymatically active state in the presence of F-actin perturbation (25, 28, 50) enhanced access of Lyn to its substrate is a compelling hypothesis for the mechanism of increased signaling caused by F-actin perturbation and is supported by the enhanced spatial coupling to IgE-Fc ϵ RI that we observe at relatively early time points after stimulation. That latrunculin causes a more rapid but transient enhancement of Lyn recruitment to Fc ϵ RI is consistent with its intervention primarily in the initial steps of signaling and with the fact that it inhibits actin polymerization more effectively than cytochalasin for the first few minutes after antigen stimulation (25). Interestingly, latrunculin leads to depletion of actin from the Triton-insoluble, membrane associated pool of actin, while also causing weak phosphorylation of Fc ϵ RI β and Syk (25, 50). We observe a small but significant increase in the amplitude of Lyn/IgE-Fc ϵ RI cross-correlation in unstimulated latrunculin-treated cells, implying that Lyn recruitment to Fc ϵ RI could account for these effects.

For both latrunculin and cytochalasin treatment, enhancement of Lyn/IgE cross-correlation amplitudes occur transiently at time points soon after antigen stimulation. Amplitudes peak 3 and 6 min after stimulation for latrunculin and cytochalasin, respectively, before falling to levels that are not significantly different from untreated cells. The timing and direction of the effects of cytochalasin and latrunculin on Lyn/IgE-Fc ϵ RI co-localization are different than the behavior observed using antigen presented on patterned substrates (10) or recorded in FCS measurements (29). In those cases,

Lyn/IgE-FcεRI co-localization was only detectable after 10 min of antigen stimulation, well after peak receptor phosphorylation, and was inhibited by pretreatment with cytochalasin while phosphorylation was enhanced. It is possible that recruitment of Lyn to clustered IgE-FcεRI at relatively long (>10 min) stimulation times is related to a negative-regulatory pathway that limits the extent of the degranulation response, and such a negative regulatory role has been proposed for Lyn (44, 51, 52). If this is the case, the fact that cytochalasin prevents Lyn recruitment to FcεRI (10, 29) is evidence that the pathway is also actin-dependent. Consistent with this, cytochalasin converts transient phosphorylation of FcεRI β to a much more long-lived response (26).

In contrast, we record antigen-stimulated Lyn recruitment to IgE-FcεRI that is concomitant with the initiation of receptor-correlated phosphotyrosine (Fig. 3.3, Fig. 3.8) and, like receptor phosphorylation (Fig. 3.6), is enhanced by inhibition of actin polymerization (Fig. 3.8). Live cell super-resolution experiments have shown that DNP-BSA-induced IgE-FcεRI clustering sufficient for the initiation of Ca²⁺ mobilization occurs in the first few minutes after antigen addition (Chapter 2 and ref. (34), and enhancement of Lyn co-localization also occurs during this time frame. These data indicate that the cross-correlation we observe is related to the initiation of signaling and is negatively regulated by actin. In this situation, actin could act to physically segregate Lyn from receptor clusters, possibly via cytoskeletal interactions with ordered lipids that modulate the lipid environment of clustered receptors, to negatively regulate signaling. There is evidence for this segregation phenomenon from electron and fluorescence microscopy (26, 36) which has been supported by additional biochemical data (25, 28). It is possible that, using our imaging approach, we could measure Lyn recruitment at later stimulation

time points that is reduced by inhibition of actin polymerization. In fact, for latrunculin-treated cells, the cross-correlation amplitude begins to dip below that of untreated cells at the 12 min stimulation time point, but this difference is not significant. We do not examine stimulation time points in our experiments that are late enough to assess this question.

Consideration of our results along with previous reports (10, 29) suggests separate interpretations of Lyn/IgE-FcεRI co-localization and its regulation by actin at early vs. late times after antigen stimulation. At early stimulation times, Lyn co-localizes with cross-linked IgE-FcεRI as part of the initiation of signaling. This association is limited through an actin polymerization-dependent process. At later times, Lyn association with IgE-FcεRI is possibly related to a negative regulatory process and is promoted by actin. In both cases, actin polymerization would lead to negative regulation of signaling. Physical shuttling of Lyn to and away from receptor clusters could occur through direct interaction with actin or, more likely, through an adapter protein such as the focal adhesion protein paxillin or the Src-family regulatory kinase Cbp/PAG. Considerable evidence exists that implicates each of these proteins in negative regulation of signaling via Lyn and association with the cytoskeleton. Paxillin is bound and phosphorylated by Lyn upon antigen stimulation and has been shown to negatively regulate early steps in the signaling cascade (2, 49, 50, 53–57). It also spatially localizes to antigen patches on patterned surfaces in an actin-polymerization- and Lyn-dependent manner (49), and may provide a direct link to the cytoskeleton (58). Cbp/PAG is strongly associated with ordered lipids and is both activated by and negatively regulates Lyn through recruitment of Csk, providing a feedback loop for Lyn

signaling. Cpb/PAG can also interact with the cytoskeleton via linkage to Epb50 and ezrin. Lyn regulation by Cpb/PAG-Csk has been shown to be relevant in FcεRI signaling (52, 59), and in particular we note that Lyn association with immunoprecipitated FcεRI is decreased in stimulated cells over expressing Cpb/PAG (59). While there is currently no demonstrated role for ezrin for antigen-stimulated signaling in mast cells, ezrin is phosphorylated in an antigen- and actin polymerization-dependent manner (50). Ezrin does have a demonstrated role in coupling ordered membranes to the cytoskeleton via its attachment to Cpb/PAG as part of the regulation of B cell signaling (60).

Regulation by actin is evident in a signaling-defective variant RBL cell line.

We conducted two-color imaging experiments analogous to experiments shown in Fig. 3.7 A and B in a variant RBL cell line, 1C1C8 cells. In these cells, antigen-stimulated receptor phosphorylation, Ca²⁺ responses, and degranulation are significantly delayed compared to RBL-2H3 cells, but IgE-FcεRI ligand binding and expression of FcεRI and Lyn are normal (R.P. Siraganian personal communication). There is evidence that the mechanism of inhibition of signaling in these cells involves overactive actin polymerization; treatment with cytochalasin accelerates antigen-stimulated Ca²⁺ responses to become comparable to RBL-2H3 kinetics without altering antigen binding (D. Holowka unpublished data).

As in RBL-2H3 cells, the amplitude of Lyn/IgE-FcεRI cross-correlations in 1C1C8 cells increases with time after antigen stimulation (Fig. 3.6 C). The absolute value of the amplitude in 1C1C8 cells is significantly reduced for the later time points measured in the experiment compared to RBL-2H3 cells (Fig. 3.6 B). Cytoskeletal perturbation has

robust effects on the strength of Lyn co-localization with IgE-Fc ϵ RI that exhibit similar trends as latrunculin- and cytochalasin-induced changes we observe in RBL-2H3 cells. Both cytochalasin and latrunculin treatment cause enhancement of Lyn/IgE-Fc ϵ RI association. Cross-correlation amplitudes in cytochalasin-treated cells are larger for stimulated time points between 3 and 12 after antigen addition. Values of the cross-correlation amplitude for latrunculin-treated cells are enhanced in unstimulated cells and for time points 1 and 3 min after antigen addition, consistent with effects in RBL-2H3 cells. Unlike results from RBL-2H3 cells, the cross-correlation length ξ is also affected by cytoskeletal perturbation in 1C1C8 cells. ξ is not significantly different with and without cytochalasin or latrunculin in unstimulated cells, but latrunculin treatment delays the antigen-induced collapse of the size of Lyn/IgE-Fc ϵ RI correlated structures. ξ is significantly larger for cytochalasin-treated cells than untreated cells for time points following 1 min after stimulation. Overall, cytoskeletal perturbation appears to enhance coupling between Lyn and IgE-Fc ϵ RI in a more pronounced fashion in 1C1C8 cells compared to RBL-2H3 cells. Maximum differences in cross-correlation amplitude are larger in the case of latrunculin treatment and persist to longer stimulation times for cytochalasin-treated cells. Lyn/Fc ϵ RI cross-correlation lengths also appear to be sensitive to cytoskeletal perturbation in 1C1C8 cells.

For 1C1C8 cells, IgE-Fc ϵ RI autocorrelation amplitudes are largely unchanged, with the exception that cytochalasin-treated cells have larger values for the cross-correlation amplitude at the 12 minute stimulated timepoint compared to latrunculin-treated or untreated cells (Fig. 3.7 B). Autocorrelation amplitudes are smaller in general

for 1C1C8 cells compared to RBL-2H3 cells. ξ for IgE-Fc ϵ RI autocorrelations is also sensitive to cytoskeletal perturbation in 1C1C8 cells (Fig. 3.7 B).

Unlike the situation in RBL-2H3 cells, the size of IgE-Fc ϵ RI aggregates as measured by ξ is sensitive to actin depolymerization. Receptor clustering is also relatively weak compared to RBL-2H3 cells, and together these data suggest that mutations in these cells that suppress signaling may interfere with formation of large or dense clusters, or may lead to their rapid internalization. Inhibition of actin polymerization causes larger-magnitude cross-correlation amplitude enhancement in 1C1C8 cells mainly due to relatively low antigen-stimulated co-localization in untreated cells. Based on our interpretation of the data from RBL-2H3 cells, this is consistent with the hypothesis that overactive actin regulation of Lyn/IgE-Fc ϵ RI coupling contributes to suppressed signaling in these cells.

Inhibition of actin polymerization amplifies antigen-dependent tyrosine phosphorylation correlated with IgE-Fc ϵ RI.

In two-color phosphotyrosine/IgE-Fc ϵ RI imaging experiments, we measure a functional outcome of cytoskeletal perturbation. We stimulate Dy654-sensitized RBL-2H3 cells, fix, and label for phosphotyrosine using the same methodology described for the data presented in Fig. 3.3, where this time the cells are first treated with cytochalasin or latrunculin as in the experiments shown in Fig. 3.6. As with Lyn/ IgE-Fc ϵ RI two-color images of actin-disrupted cells (Fig. 3.6, A), the organization of 4G10 and IgE-Fc ϵ RI does not appear to be dramatically altered by cytochalasin or latrunculin treatment by visual inspection of 2-color super-resolution images (Fig. 3.8, A).

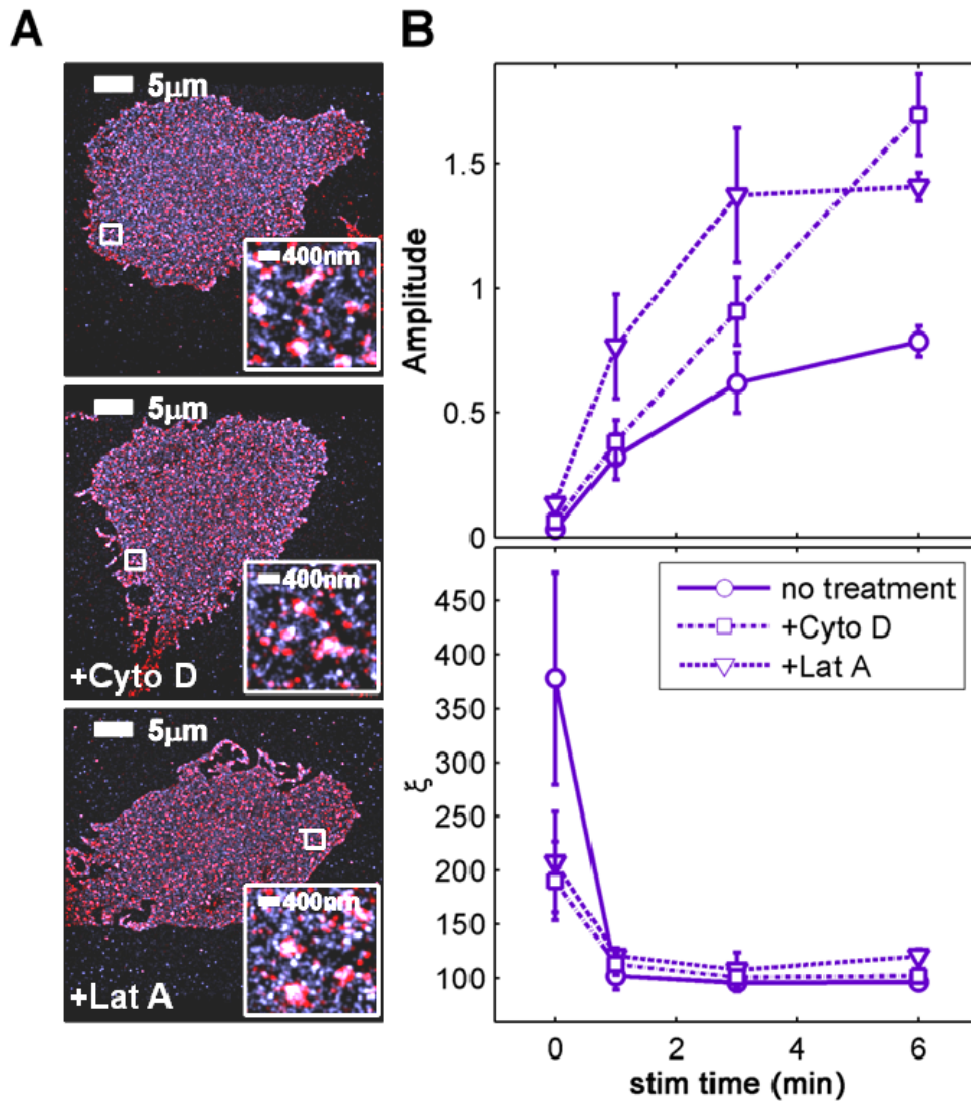


Fig. 3.8 Receptor-correlated phosphotyrosine is enhanced due to inhibition of actin polymerization. Representative A488 4G10/Dy654 IgE two-color super-resolution images (A) and average cross-correlation function parameters for fits to Eqn. 2 (B) for RBL-2H3 cells that were stimulated for 0, 1, 3, or 6 min with and without pre-treatment with 1 μ M latrunculin or cytochalasin. Treated cells were also stimulated in the presence of the drug. (A) Selected images of cells stimulated for 6 min without (top) or with treatment with cytochalasin (middle) or latrunculin (bottom). (B) 4G10/IgE-Fc ϵ RI cross-correlation fit parameters Amplitude and ξ as a function of stimulation time for RBL-2H3 cells sensitized with Dy654 IgE and immunolabeled with A488 4G10 anti-phosphotyrosine that were stimulated for 0, 1, 3, or 6 min with and without treatment with actin-disrupting drugs. Fit parameters are averaged over multiple cells for each timepoint (n=6 cells per timepoint for untreated cells, n = 7 cells per timepoint for cytochalasin and latrunculin-treated cells). 4G10/IgE-Fc ϵ RI cross-correlation function fit parameters are also plotted and were reproduced from Fig. 3.3. Error bars denote SEM.

Analysis of cross-correlation functions show that perturbation of the cytoskeleton leads to relative increases in receptor-correlated phosphotyrosine that are qualitatively similar to observed changes in Lyn/IgE co-localization under the same conditions of stimulation and latrunculin or cytochalasin treatment (Fig. 3.6 B). 4G10 label and IgE-FcεRI are more correlated in latrunculin and cytochalasin treated cells for all stimulated time points except for the 1 min time point in the case of cytochalasin treatment (Fig. 3.8, B). The effects of latrunculin are more prominent at earlier stimulated time points, whereas the differences between cytochalasin-treated and untreated cells are greater at the later stimulated time points measured in this experiment, consistent with trends observed for Lyn/IgE-FcεRI cross-correlations (Fig. 3.6, B).

To further clarify whether cytochalasin- and latrunculin-induced enhancement of stimulated IgE-FcεRI-localized phosphorylation depend on Lyn, we measure 4G10/IgE-FcεRI cross-correlation functions in a Syk-negative variant of the RBL-2H3 cell line. These cells do not express Syk kinase at a detectable level and do not exhibit antigen-stimulated Ca^{2+} or degranulation responses. IgE-FcεRI aggregation elicits receptor phosphorylation in Syk-negative cells, albeit at slightly lower levels. This difference is possibly due to protection of γ chains from de-phosphorylation by Syk binding in normal cells (61). Cells are stimulated with antigen for 6 min with and without pre-treatment with latrunculin or cytochalasin and labeled for phosphotyrosine. Super-resolution images of stimulated Syk-negative cells that are treated with latrunculin or cytochalasin look qualitatively similar to untreated cells (Fig. 3.9, A), but cross-correlation functions computed from these images have larger amplitudes (Fig. 3.9, B). ξ is slightly larger in cytochalasin-treated cells compared to the other treatment conditions but is equivalent

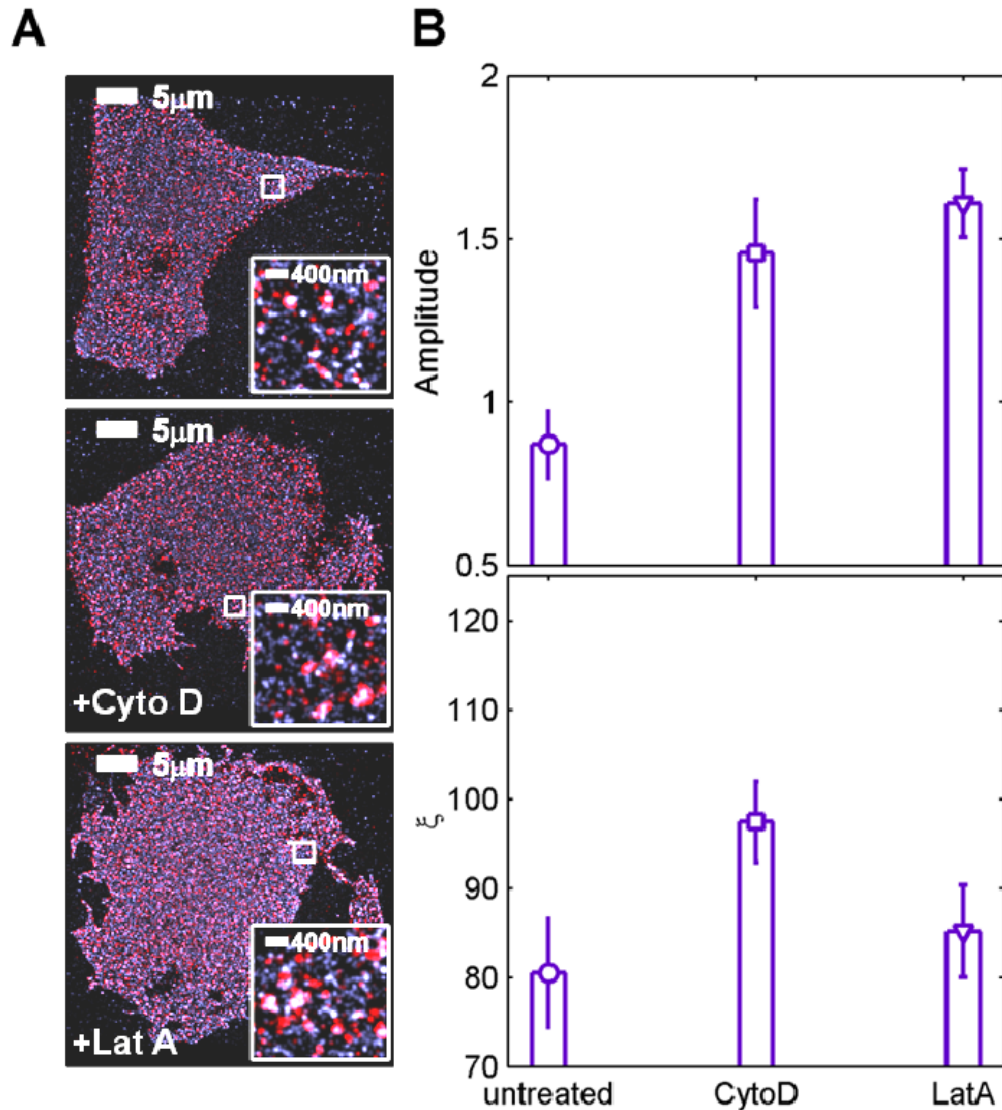


Fig. 3.9 Increased receptor phosphorylation due to cytochalasin and latrunculin is mediated by Lyn. Representative A488 4G10/Dy654 IgE two-color super-resolution images (A) and average cross-correlation function parameters for fits to Eqn. 2 (B) for Syk-negative TB1A2 cells that were stimulated for 6 min with and without pre-treatment with 1 μ M latrunculin or cytochalasin. Treated cells were stimulated in the presence of the drug. (A) Selected images of cells stimulated for 6 min without (top) or with treatment with cytochalasin (middle) or latrunculin (bottom). (B) Average 4G10/IgE-Fc ϵ R1 cross-correlation fit parameters Amplitude and ξ at for A488 4G10/Dy654 IgE two-color images of Syk-negative cells that were stimulated for 6 min with and without treatment with actin-disrupting drugs. Fit parameters are averaged over multiple cells for each treatment condition (n=4 cells for all treatment conditions). Error bars denote SEM.

for latrunculin-treated and untreated cells. Data shown in Fig. 3.9 was collected in an initial experiment and will need to be reproduced in order to confirm these results.

Although these data are preliminary, they indicate that the difference we observe in IgE-Fc ϵ RI-correlated phosphotyrosine is present in the absence of signaling that depends on Syk activation and cannot be attributed to feedback inhibition caused by Syk-dependent processes. In Syk-negative cells, antigen-stimulated phosphorylation localized to IgE-Fc ϵ RI clusters depends on Lyn signaling, and so inhibition of actin polymerization enhances phosphorylation through a net decrease in the negative regulation of Lyn. This suggests that in normal RBL-2H3 signaling, at least one component of regulation by actin is negative regulation of Lyn.

Measurements of 4G10/IgE-Fc ϵ RI cross-correlations in cells treated with cytochalasin and latrunculin show that receptor-correlated phosphorylation is enhanced, with time dependence that matches Lyn/IgE-Fc ϵ RI co-localization enhancement for each drug (Figs. 3.6 B and 3.8 B). This correlative result supports the hypothesis that the latrunculin and cytochalasin-dependent increase in coupling of Lyn to clustered receptors observed at early stimulation times is associated with the initiation of signaling and can be responsible for the amplification of downstream signaling responses caused by treatment with these drugs. It also provides evidence that F-actin perturbation leads to an elevated response to antigen even in the first steps of IgE receptor signaling, in agreement with experiments that have demonstrated enhanced phosphorylation of Fc ϵ RI and other downstream signaling proteins such as Syk and LAT when actin polymerization is inhibited (10, 25, 26, 28, 50). Here we are additionally able to show

this enhancement of signaling through direct, high-resolution imaging of signaling moieties in situ on the plasma membrane.

Our preliminary finding that receptor-correlated phosphotyrosine is also elevated in stimulated Syk-negative cells is consistent with the idea that cytoskeletal perturbation causes enhanced receptor-correlated phosphotyrosine in RBL-2H3 cells through removal of negative regulation of Lyn coupling to IgE-Fc ϵ RI by actin. It has been demonstrated that while total phosphorylation is dramatically reduced in Syk-negative cells, phosphorylation of the Fc ϵ RI β , and to lesser extent γ , is still observed, confirming that Lyn causes antigen-stimulated receptor phosphorylation in the absence of Syk (61).

Whereas Lyn recruitment to IgE-Fc ϵ RI in actin-disrupted cells is enhanced compared to untreated cells for only the first few minutes after stimulation, the effects of actin depolymerization on elevation of receptor-correlated phosphotyrosine are more long-lived, extending through the longest stimulation timepoint measured in this experiment (6 min) for both latrunculin and cytochalasin treatment. This indicates that either the increase in phosphorylation induced at earlier stimulation times is long-lived and/or dephosphorylation by phosphatases is inhibited by F-actin perturbation. In relation to Lyn/IgE-Fc ϵ RI cross-correlation in the presence and absence of actin perturbation (Fig. 3.6), we have discussed the possibility that the continued accumulation of Lyn with clustered receptors at later stimulation times is somehow related to negative regulation of signaling. If this is the case, enhanced phosphorylation of receptor clusters at these later time points for cells where actin polymerization is inhibited compared to untreated cells would be consistent with similar or lower levels of Lyn co-localization. For example, phosphorylation is enhanced over receptor clusters on

patterned substrates even when cytochalasin prevents the accumulation of Lyn in these regions (10).

Lipid anchor type plays a role in the magnitude and actin-dependence of stimulated co-localization of lipid-anchored proteins with IgE-FcεRI.

Localization of Lyn with ordered lipids mediated by its order-preferring lipid anchorage is thought to be important for its phosphorylation of IgE-FcεRI upon receptor cross-linking (14, 16), and has been shown to partially mediate co-localization with FcεRI on patterned substrates (10) and cells cross-linked at 4°C (17). To test the hypothesis that the lipid anchorage of Lyn can be a structural factor that participates in actin-based regulation of Lyn-receptor interaction, we used the fluorescent construct PM-mEos3.2. PM-mEos3.2 consists of mEos3.2 and the N-terminal tail of Lyn that includes its palmitoylation and myristoylation sites, but does not retain its kinase or protein-binding domains. We imaged stimulated cells transfected with this construct in conjunction with Dy654-IgE (Fig. 3.10). From two-color images, we observe a distribution of PM-mEos3.2 that is qualitatively similar to that of Lyn with respect to Dy654 IgE in stimulated cells (Fig. 3.10, A). Also like Lyn, PM-mEos3.2 becomes increasingly correlated with IgE receptors with increasing stimulation time as measured by the cross-correlation amplitude (Fig. 3.10, B), and PM-mEos3.2 association with IgE receptor is enhanced by treatment with latrunculin. Trends in the stimulation time-dependent increase of PM/IgE-FcεRI cross-correlation and the effect of latrunculin treatment match the behavior observed for Lyn/IgE-FcεRI cross-correlations, except that PM/IgE-FcεRI co-localization grows at a slower rate than Lyn/IgE-FcεRI with

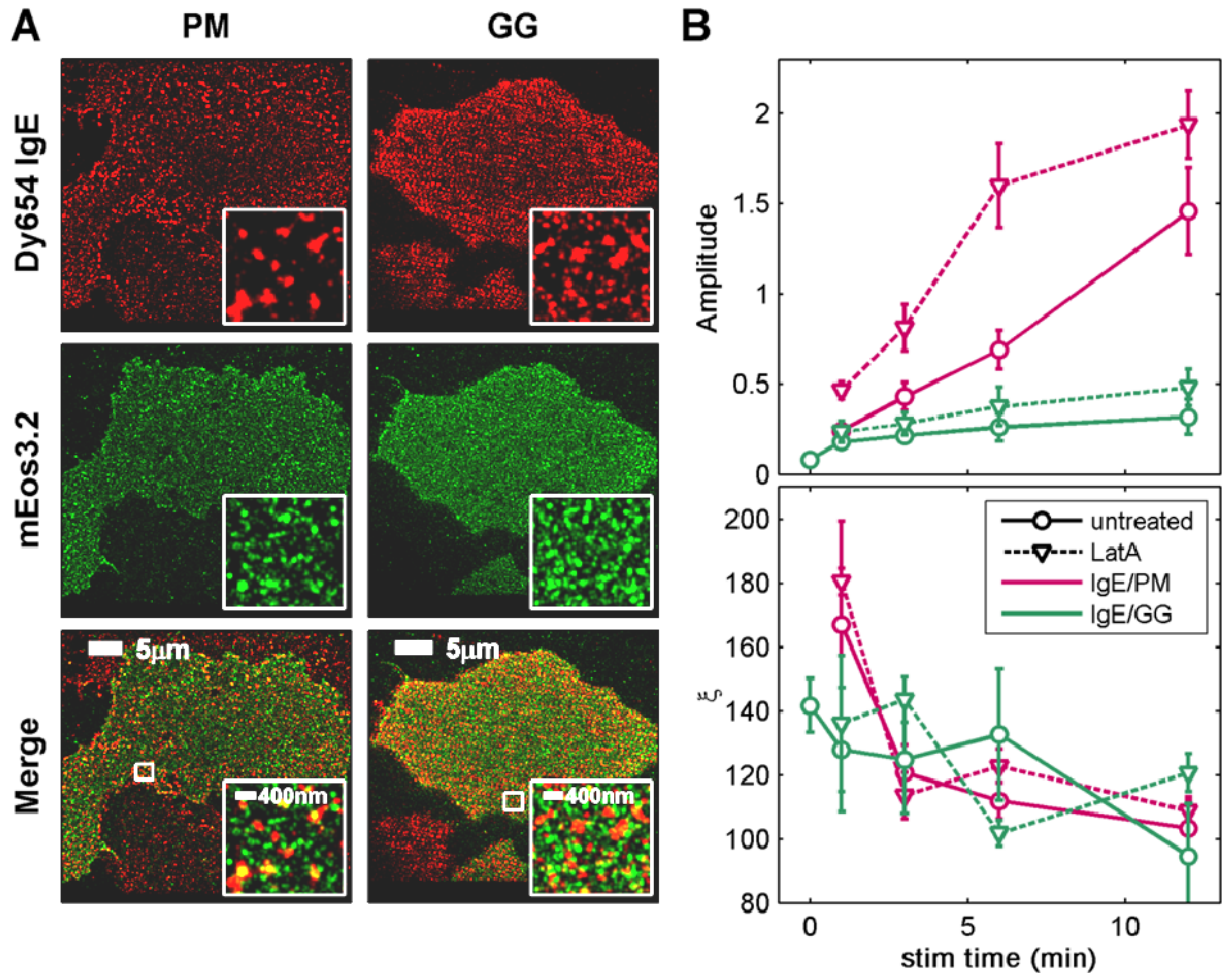


Fig. 3.10 Lipid anchorage of mEos3.2 constructs determines antigen-induced recruitment to IgE/Fc ϵ RI and the effects of cytoskeletal perturbation. Representative two-color super-resolution images (A) and average cross-correlation function fit parameters for fits to Eqn. 2 (B) for cells expressing PM-mEos3.2 or mEos3.2-GG sensitized with Dy654 IgE. (A) Representative images of Dy654 IgE (top), PM-mEos3.2 (middle, left) or mEos3.2-GG (middle, right), and merged images (bottom) in cells stimulated for 6 min. (B) Average PM/IgE-Fc ϵ RI and GG/IgE-Fc ϵ RI cross-correlation fit parameters Amplitude and ξ as a function of stimulation time in RBL-2H3 cells. Cells were stimulated for 1, 3, 6, or 12 min for PM-mEos3.2-expressing cells or 0, 1, 3, 6, or 12 min for GG-mEos3.2-expressing cells with and without pre-treatment with and stimulation in the presence of 1 μ M latrunculin. Fit parameters are averaged over multiple cells for each timepoint ($n=7$ cells per timepoint for cells expressing both constructs and for both treatment conditions). Error bars denote SEM.

respect to stimulation time in both untreated and latrunculin-treated cells. PM/IgE-Fc ϵ RI correlation lengths also decrease with stimulation time. Values of ξ are slightly larger than for Lyn/IgE-Fc ϵ RI cross-correlations, but this difference is not significant for several stimulated time points.

For comparison to the PM lipid anchor, we measured the co-localization of IgE-Fc ϵ RI with a second lipid-anchored mEos3.2 construct, mEos3.2-GG. Here, mEos3.2 is associated with the plasma membrane via the lipid anchorage of K-Ras, which consists of a geranylgeranyl modification and a polybasic sequence. In two-color images, mEos3.2-GG seems to form structures that are correlated with IgE-Fc ϵ RI clusters less frequently than PM-mEos3.2 (Fig. 3.10, A). There is a small antigen-induced increase in GG/IgE-Fc ϵ RI interaction after 1 min of antigen stimulation, but the cross-correlation amplitude quickly plateaus and does not reach levels comparable to PM/IgE-Fc ϵ RI or Lyn/IgE-Fc ϵ RI cross-correlations during the stimulation times measured (Fig. 3.10, B). GG/IgE-Fc ϵ RI coupling is not significantly affected by latrunculin treatment. GG and IgE-Fc ϵ RI are correlated over fairly consistent distances before and after stimulation that are not affected by latrunculin treatment as measured by ξ .

From these data, it appears that the PM anchor is sufficient to cause nanoscale co-localization of PM-mEos3.2 with clustered IgE-Fc ϵ RI. This co-localization is consistent with previous reports of PM co-localization with receptor in cells cross-linked at 4°C (17, 18) and stimulated on antigen-patterned surfaces (10), and here we also observe PM recruitment at high spatial resolution, at early stimulation times relevant to the initiation of signaling, and with stimulation at physiological temperature. We also show that targeting to ordered lipids is relevant for actin destabilization-dependent

enhancement of co-localization which has been suggested by fluorescence imaging experiments (26). The kinetics of PM recruitment to IgE-Fc ϵ RI are slowed compared to Lyn, as they are for recruitment of PM to patterned antigen (10). This suggests a joint contribution of Lyn binding to Fc ϵ RI via its SH2 domain (11, 62) and Lyn association with ordered lipids to its co-localization with cross-linked IgE-Fc ϵ RI (9, 10, 63) .

In contrast to PM-mEos3.2, mEos3.2-GG co-redistribution with clustered receptors is much more modest and is not significantly affected by inhibition of actin polymerization. The GG lipid anchor associates with ordered lipids to a lesser extent than PM (64). When RBL-2H3 are subjected to receptor cross-linking at low temperatures GG co-localizes more weakly than PM to receptor patches (17). Comparison of GG and PM diffusion in this situation suggests that GG does not strongly interact with components within the receptor patch, whereas PM becomes substantially confined (18) .

The cytoskeleton itself can cause dramatic changes in the ordered lipid environment of the membrane through the antigen-stimulated actin remodeling exemplified in the TIRF images shown in Fig. 3.4 (30). These changes are apparently caused by the initial antigen-stimulated depolymerization of actin that is evident in these TIRF images, and accordingly also occurs with cytochalasin or latrunculin treatment (30). This is a compelling reason to think that actin regulation of antigen-stimulated processes can occur through membrane lipids, and in this context, our data is suggestive of negative regulation of signaling by actin via Lyn is mediated through association of Lyn with ordered lipids. Super-resolution fluorescence localization microscopy allows us to assess these questions at high resolution through direct

imaging of the plasma membrane. With this tool in hand, we are in a position to test models of actin cytoskeleton-induced organization of plasma membrane lipids.

CONTRIBUTIONS AND ACKNOWLEDGEMENTS

Research was designed by S. A. Shelby, D. A. Holowka, and B. A. Baird. S. A. Shelby performed super-resolution imaging and TIRF experiments and analyzed super-resolution data. A. Wageknecht-Wiesner, J. D. Wilson, and S. A. Shelby cloned mEos3.2 fluorescent constructs. Data analysis code was written by S. L. Veatch, M. B. Stone (University of Michigan), and S. A. Shelby. This chapter was written by S. A. Shelby, D. A. Holowka, and B. A. Baird. This research was supported through NIH RO1 AI018306 (D. A. Holowka and B. A. Baird). S. A. Shelby acknowledges partial support from the Molecular Biophysics Training Grant (T32GM008267).

We additionally thank Eshan Mitra for assistance with super-resolution experiments and preparation of reagents, and Dr. Sarah Veatch and Matthew Stone for helpful discussions concerning data analysis and fluorescent constructs.

REFERENCES

1. Barsumian, E.L., C. Isersky, M.G. Petrino, and R.P. Siraganian. 1981. IgE-induced histamine release from rat basophilic leukemia cell lines: isolation of releasing and nonreleasing clones. *Eur. J. Immunol.* 11: 317–323.
2. Hamawy, M.M., W.D. Swaim, K. Minoguchi, A.W. de Feijter, S.E. Mergenhagen, and R.P. Siraganian. 1994. The aggregation of the high affinity IgE receptor induces tyrosine phosphorylation of paxillin, a focal adhesion protein. *J. Immunol.* 153: 4655–4662.
3. Siraganian, R.P. 2003. Mast cell signal transduction from the high-affinity IgE receptor. *Curr. Opin. Immunol.* 15: 639–646.
4. Paolini, R., M.H. Jouvin, and J.P. Kinet. 1991. Phosphorylation and dephosphorylation of the high-affinity receptor for immunoglobulin E immediately after receptor engagement and disengagement. *Nature.* 353: 855–858.
5. Jouvin, M.H., M. Adamczewski, R. Numerof, O. Letourneur, A. Vallé, and J.P. Kinet. 1994. Differential control of the tyrosine kinases Lyn and Syk by the two signaling chains of the high affinity immunoglobulin E receptor. *J. Biol. Chem.* 269: 5918–5925.
6. Sheets, E.D., D. Holowka, and B. Baird. 1999. Membrane organization in immunoglobulin E receptor signaling. *Curr. Opin. Chem. Biol.* 3: 95–99.
7. Yamashita, T., S.Y. Mao, and H. Metzger. 1994. Aggregation of the high-affinity IgE receptor and enhanced activity of p53/56lyn protein-tyrosine kinase. *Proc. Natl. Acad. Sci.* 91: 11251–11255.
8. Pribluda, V.S., C. Pribluda, and H. Metzger. 1994. Transphosphorylation as the mechanism by which the high-affinity receptor for IgE is phosphorylated upon aggregation. *Proc. Natl. Acad. Sci.* 91: 11246–11250.
9. Veatch, S.L., E.N. Chiang, P. Sengupta, D.A. Holowka, and B.A. Baird. 2012. Quantitative nanoscale analysis of IgE-FcεRI clustering and coupling to early signaling proteins. *J. Phys. Chem. B.* 116: 6923–6935.
10. Wu, M., D. Holowka, H.G. Craighead, and B. Baird. 2004. Visualization of plasma membrane compartmentalization with patterned lipid bilayers. *Proc. Natl. Acad. Sci. U. S. A.* 101: 13798–13803.
11. Hammond, S., A. Wagenknecht-Wiesner, S.L. Veatch, D. Holowka, and B. Baird. 2009. Roles for SH2 and SH3 Domains in Lyn Kinase Association with Activated FcεRI in RBL Mast Cells Revealed by Patterned Surface Analysis. *J. Struct. Biol.* 168: 161–167.

12. Field, K.A., D. Holowka, and B. Baird. 1997. Compartmentalized Activation of the High Affinity Immunoglobulin E Receptor within Membrane Domains. *J. Biol. Chem.* 272: 4276–4280.
13. Field, K.A., D. Holowka, and B. Baird. 1995. FcεRI-mediated recruitment of p53/56lyn to detergent-resistant membrane domains accompanies cellular signaling. *Proc. Natl. Acad. Sci.* 92: 9201–9205.
14. Young, R.M., D. Holowka, and B. Baird. 2003. A Lipid Raft Environment Enhances Lyn Kinase Activity by Protecting the Active Site Tyrosine from Dephosphorylation. *J. Biol. Chem.* 278: 20746–20752.
15. Sheets, E.D., D. Holowka, and B. Baird. 1999. Critical Role for Cholesterol in Lyn-mediated Tyrosine Phosphorylation of FcεRI and Their Association with Detergent-resistant Membranes. *J. Cell Biol.* 145: 877–887.
16. Holowka, D., J.A. Gosse, A.T. Hammond, X. Han, P. Sengupta, N.L. Smith, A. Wagenknecht-Wiesner, M. Wu, R.M. Young, and B. Baird. 2005. Lipid segregation and IgE receptor signaling: A decade of progress. *Biochim. Biophys. Acta BBA - Mol. Cell Res.* 1746: 252–259.
17. Pyenta, P.S., D. Holowka, and B. Baird. 2001. Cross-correlation analysis of inner-leaflet-anchored green fluorescent protein co-redistributed with IgE receptors and outer leaflet lipid raft components. *Biophys. J.* 80: 2120–2132.
18. Pyenta, P.S., P. Schwille, W.W. Webb, D. Holowka, and B. Baird. 2003. Lateral Diffusion of Membrane Lipid-Anchored Probes before and after Aggregation of Cell Surface IgE-Receptors†. *J. Phys. Chem. A.* 107: 8310–8318.
19. Young, R.M., X. Zheng, D. Holowka, and B. Baird. 2005. Reconstitution of Regulated Phosphorylation of FcεRI by a Lipid Raft-excluded Protein-tyrosine Phosphatase. *J. Biol. Chem.* 280: 1230–1235.
20. Heneberg, P., L. Dráberová, M. Bambousková, P. Pompach, and P. Dráber. 2010. Down-regulation of protein-tyrosine phosphatases activates an immune receptor in the absence of its translocation into lipid rafts. *J. Biol. Chem.* 285: 12787–12802.
21. Pfeiffer, J.R., J.C. Seagrave, B.H. Davis, G.G. Deanin, and J.M. Oliver. 1985. Membrane and cytoskeletal changes associated with IgE-mediated serotonin release from rat basophilic leukemia cells. *J. Cell Biol.* 101: 2145–2155.
22. Urata, C., and R.P. Siraganian. 1985. Pharmacologic modulation of the IgE or Ca²⁺ ionophore A23187 mediated Ca²⁺ influx, phospholipase activation, and histamine release in rat basophilic leukemia cells. *Int. Arch. Allergy Appl. Immunol.* 78: 92–100.

23. Narasimhan, V., D. Holowka, and B. Baird. 1990. Microfilaments regulate the rate of exocytosis in rat basophilic leukemia cells. *Biochem. Biophys. Res. Commun.* 171: 222–229.
24. Seagrave, J., and J.M. Oliver. 1990. Antigen-dependent transition of IgE to a detergent-insoluble form is associated with reduced IgE receptor-dependent secretion from RBL-2H3 mast cells. *J. Cell. Physiol.* 144: 128–136.
25. Frigeri, L., and J.R. Apgar. 1999. The Role of Actin Microfilaments in the Down-Regulation of the Degranulation Response in RBL-2H3 Mast Cells. *J. Immunol.* 162: 2243–2250.
26. Holowka, D., E. d. Sheets, and B. Baird. 2000. Interactions between FcεRI and lipid raft components are regulated by the actin cytoskeleton. *J. Cell Sci.* 113: 1009 – 1019.
27. Pierini, L., N.T. Harris, D. Holowka, and B. Baird. 1997. Evidence Supporting a Role for Microfilaments in Regulating the Coupling between Poorly Dissociable IgE–FcεRI Aggregates and Downstream Signaling Pathways. *Biochemistry.* 36: 7447–7456.
28. Torigoe, C., J. Song, B.G. Barisas, and H. Metzger. 2004. The influence of actin microfilaments on signaling by the receptor with high-affinity for IgE. *Mol. Immunol.* 41: 817–829.
29. Larson, D.R., J.A. Gosse, D.A. Holowka, B.A. Baird, and W.W. Webb. 2005. Temporally resolved interactions between antigen-stimulated IgE receptors and Lyn kinase on living cells. *J. Cell Biol.* 171: 527–536.
30. Han, X., N.L. Smith, D. Sil, D.A. Holowka, F.W. McLafferty, and B.A. Baird. 2009. IgE receptor-mediated alteration of membrane-cytoskeletal interactions revealed by mass spectrometric analysis of detergent-resistant membranes. *Biochemistry.* 48: 6540–6550.
31. Machta, B.B., S. Papanikolaou, J.P. Sethna, and S.L. Veatch. 2011. Minimal Model of Plasma Membrane Heterogeneity Requires Coupling Cortical Actin to Criticality. *Biophys. J.* 100: 1668–1677.
32. Ehrig, J., E.P. Petrov, and P. Schwille. 2011. Near-critical fluctuations and cytoskeleton-assisted phase separation lead to subdiffusion in cell membranes. *Biophys. J.* 100: 80–89.
33. Torres, A.J., M. Wu, D. Holowka, and B. Baird. 2008. Nanobiotechnology and Cell Biology: Micro- and Nanofabricated Surfaces to Investigate Receptor-Mediated Signaling. *Annu. Rev. Biophys.* 37: 265–288.

34. Shelby, S.A., D. Holowka, B. Baird, and S.L. Veatch. 2013. Distinct stages of stimulated FcεRI receptor clustering and immobilization are identified through superresolution imaging. *Biophys. J.* 105: 2343–2354.
35. Veatch, S.L., B.B. Machta, S.A. Shelby, E.N. Chiang, D.A. Holowka, and B.A. Baird. 2012. Correlation functions quantify super-resolution images and estimate apparent clustering due to over-counting. *PLoS One.* 7: e31457.
36. Wilson, B.S., J.R. Pfeiffer, and J.M. Oliver. 2000. Observing FcεRI Signaling from the Inside of the Mast Cell Membrane. *J. Cell Biol.* 149: 1131–1142.
37. Betzig, E., G.H. Patterson, R. Sougrat, O.W. Lindwasser, S. Olenych, J.S. Bonifacino, M.W. Davidson, J. Lippincott-Schwartz, and H.F. Hess. 2006. Imaging Intracellular Fluorescent Proteins at Nanometer Resolution. *Science.* 313: 1642 – 1645.
38. Rust, M.J., M. Bates, and X. Zhuang. 2006. Stochastic optical reconstruction microscopy (STORM) provides sub-diffraction-limit image resolution. *Nat. Methods.* 3: 793–795.
39. Hess, S.T., T.P.K. Girirajan, and M.D. Mason. 2006. Ultra-High Resolution Imaging by Fluorescence Photoactivation Localization Microscopy. *Biophys. J.* 91: 4258–4272.
40. Gosse, J.A., A. Wagenknecht-Wiesner, D. Holowka, and B. Baird. 2005. Transmembrane Sequences Are Determinants of Immunoreceptor Signaling. *J. Immunol.* 175: 2123 –2131.
41. Hardy, R.R. 1986. *Handbook of Experimental Immunology*. 4th ed. Oxford, UK: Blackwell Scientific Publication.
42. Zhang, M., H. Chang, Y. Zhang, J. Yu, L. Wu, W. Ji, J. Chen, B. Liu, J. Lu, Y. Liu, J. Zhang, P. Xu, and T. Xu. 2012. Rational design of true monomeric and bright photoactivatable fluorescent proteins. *Nat. Methods.* 9: 727–729.
43. Erickson, J., B. Goldstein, D. Holowka, and B. Baird. 1987. The effect of receptor density on the forward rate constant for binding of ligands to cell surface receptors. *Biophys. J.* 52: 657–662.
44. Honda, Z., T. Suzuki, N. Hirose, M. Aihara, T. Shimizu, S. Nada, M. Okada, C. Ra, Y. Morita, and K. Ito. 1997. Roles of C-terminal Src Kinase in the Initiation and the Termination of the High Affinity IgE Receptor-mediated Signaling. *J. Biol. Chem.* 272: 25753–25760.
45. Pribluda, V.S., and H. Metzger. 1992. Transmembrane signaling by the high-affinity IgE receptor on membrane preparations. *Proc. Natl. Acad. Sci. U. S. A.* 89: 11446–11450.

46. Xu, K., B. Goldstein, D. Holowka, and B. Baird. 1998. Kinetics of Multivalent Antigen DNP-BSA Binding to IgE-Fc ϵ RI in Relationship to the Stimulated Tyrosine Phosphorylation of Fc ϵ RI. *J. Immunol.* 160: 3225–3235.
47. Wollman, R., and T. Meyer. 2012. Coordinated oscillations in cortical actin and Ca²⁺ correlate with cycles of vesicle secretion. *Nat. Cell Biol.* 14: 1261–1269.
48. Norman, J.C., L.S. Price, A.J. Ridley, A. Hall, and A. Koffer. 1994. Actin filament organization in activated mast cells is regulated by heterotrimeric and small GTP-binding proteins. *J. Cell Biol.* 126: 1005–1015.
49. Torres, A.J., L. Vasudevan, D. Holowka, and B.A. Baird. 2008. Focal adhesion proteins connect IgE receptors to the cytoskeleton as revealed by micropatterned ligand arrays. *Proc. Natl. Acad. Sci. U. S. A.* 105: 17238–17244.
50. Tolarová, H., L. Dráberová, P. Heneberg, and P. Dráber. 2004. Involvement of filamentous actin in setting the threshold for degranulation in mast cells. *Eur. J. Immunol.* 34: 1627–1636.
51. Xiao, W., H. Nishimoto, H. Hong, J. Kitaura, S. Nunomura, M. Maeda-Yamamoto, Y. Kawakami, C.A. Lowell, C. Ra, and T. Kawakami. 2005. Positive and negative regulation of mast cell activation by Lyn via the Fc ϵ RI. *J. Immunol. Baltim. Md* 1950. 175: 6885–6892.
52. Odom, S., G. Gomez, M. Kovarova, Y. Furumoto, J.J. Ryan, H.V. Wright, C. Gonzalez-Espinosa, M.L. Hibbs, K.W. Harder, and J. Rivera. 2004. Negative Regulation of Immunoglobulin E–dependent Allergic Responses by Lyn Kinase. *J. Exp. Med.* 199: 1491–1502.
53. Minoguchi, K., H. Kihara, H. Nishikata, M.M. Hamawy, and R.P. Siraganian. 1994. Src family tyrosine kinase Lyn binds several proteins including paxillin in rat basophilic leukemia cells. *Mol. Immunol.* 31: 519–529.
54. Suzuki, T., S. Shoji, K. Yamamoto, S. Nada, M. Okada, T. Yamamoto, and Z. Honda. 1998. Essential roles of Lyn in fibronectin-mediated filamentous actin assembly and cell motility in mast cells. *J. Immunol. Baltim. Md* 1950. 161: 3694–3701.
55. Rathore, V.B., M. Okada, P.J. Newman, and D.K. Newman. 2007. Paxillin family members function as Csk-binding proteins that regulate Lyn activity in human and murine platelets. *Biochem. J.* 403: 275–281.
56. Chew, V., and K.-P. Lam. 2007. Leupaxin Negatively Regulates B Cell Receptor Signaling. *J. Biol. Chem.* 282: 27181–27191.
57. Tolar, P., L. Dráberová, H. Tolarová, and P. Dráber. 2004. Positive and negative regulation of Fc epsilon receptor I-mediated signaling events by Lyn kinase C-terminal tyrosine phosphorylation. *Eur. J. Immunol.* 34: 1136–1145.

58. Critchley, D.R. 2000. Focal adhesions – the cytoskeletal connection. *Curr. Opin. Cell Biol.* 12: 133–139.
59. Ohtake, H., N. Ichikawa, M. Okada, and T. Yamashita. 2002. Cutting Edge: Transmembrane Phosphoprotein Csk-Binding Protein/Phosphoprotein Associated With Glycosphingolipid-Enriched Microdomains as a Negative Feedback Regulator of Mast Cell Signaling Through the FcεRI. *J. Immunol.* 168: 2087–2090.
60. Gupta, N., B. Wollscheid, J.D. Watts, B. Scheer, R. Aebersold, and A.L. DeFranco. 2006. Quantitative proteomic analysis of B cell lipid rafts reveals that ezrin regulates antigen receptor-mediated lipid raft dynamics. *Nat. Immunol.* 7: 625–633.
61. Zhang, J., E.H. Berenstein, R.L. Evans, and R.P. Siraganian. 1996. Transfection of Syk protein tyrosine kinase reconstitutes high affinity IgE receptor-mediated degranulation in a Syk-negative variant of rat basophilic leukemia RBL-2H3 cells. *J. Exp. Med.* 184: 71–79.
62. Kovárová, M., P. Tolar, R. Arudchandran, L. Dráberová, J. Rivera, and P. Dráber. 2001. Structure-function analysis of Lyn kinase association with lipid rafts and initiation of early signaling events after FcεRI aggregation. *Mol. Cell. Biol.* 21: 8318–8328.
63. Honda, Z., T. Suzuki, H. Kono, M. Okada, T. Yamamoto, C. Ra, Y. Morita, and K. Yamamoto. 2000. Sequential Requirements of the N-Terminal Palmitoylation Site and SH2 Domain of Src Family Kinases in the Initiation and Progression of FcεRI Signaling. *Mol. Cell. Biol.* 20: 1759–1771.
64. Silvius, J.R. 2002. Mechanisms of Ras Protein Targeting in Mammalian Cells. *J. Membr. Biol.* 190: 83–92.

CHAPTER FOUR

CONCLUSIONS AND FUTURE DIRECTIONS

CONCLUSIONS

In conclusion, we demonstrate that super-resolution fluorescence localization imaging is a powerful method for quantifying the organization and mobility of immune receptors, as well as their association with downstream signaling partners, in cells undergoing stimulated responses. Although FcεRI signaling has been previously studied using a variety of biochemical methods and conventional microscopy approaches, high resolution imaging has brought a new level of detail to our investigations of the spatial regulation of signaling on the membrane.

In Chapter 2, we show that simultaneous measurements of clustering and diffusion enable the resolution of two distinct temporal phases of receptor clustering and immobilization. At early times after stimulation, receptor-rich clusters increase marginally in size and receptors slow dramatically when averaged over the population of receptors (Fig. 2.5). When examined as individual molecules, either as monomers or as members of clusters, single receptors appear to reversibly associate with small and slowly moving receptor clusters soon after the addition of antigen (Fig. 2.7). These behaviors are observed at stimulation times preceding Ca^{2+} mobilization, leading us to conclude that they arise from interactions associated with initial signaling steps. At later times, receptors in clusters become increasingly dense and are largely immobile. Since these behaviors occur at times following the initial Ca^{2+} response, we hypothesize that

receptor immobilization into densely packed clusters leads to subsequent cellular interactions related to down regulation of signaling. Prior to these terminating steps, dense receptor clusters are dispersed when the cross-linking antigen is displaced by a monovalent ligand, demonstrating dynamics and reversibility of interactions during initial steps of signaling (Fig. 2.9).

Receptor clustering and dynamics are also altered in cells with modulated cholesterol levels (Figs 2.10-2.14). Receptors cluster in cells with increased cholesterol levels even in the absence of antigen. Further, we observe changes in the duration of the initial phase of receptor clustering and immobilization in stimulated cells with modulated cholesterol levels, as well as corresponding changes in the timing of Ca^{2+} mobilization (Fig. 2.13).

The onset of Ca^{2+} mobilization requires association of activated receptors with multiple proteins including Lyn, Syk, LAT, and PLC γ , and this signaling complex formation appears to occur before or during the cross-over between the two regimes defined by our analysis. We observe differences in the timing of Ca^{2+} mobilization for cells with modulated cholesterol levels that correspond with changes in the timing of the initial phase of clustering. As a whole, these findings add significant detail to the current description of stimulated changes in receptor organization and mobility, and elucidate the relationship between these physical properties of receptors and functional responses in signaling.

In Chapter 3, we expand upon the results of our single-color imaging experiments shown in Chapter 2 and (1) by utilizing a second imaging channel to measure co-localization of IgE-Fc ϵ RI complexes with other signaling molecules during

the antigen-stimulated response. With the goal of investigating the mechanisms by which signaling is initiated by receptor cross-linking and regulated in the early stages of the response, we focus on Lyn, the first interaction partner for cross-linked IgE-FcεRI. This work builds on electron microscopy measurements of Lyn coupling to clustered IgE-FcεRI. The sub-diffraction spatial resolution provided by localization microscopy combined with quantification by pair-correlation analysis enables measurement of Lyn spatial coupling to cross-linked IgE-FcεRI in the first few minutes after antigen stimulation, during the initiation of the stimulated response. We observe a stimulation time-dependent increase in Lyn/IgE-FcεRI co-localization that is detectable at the first time point measured 1 min following stimulation (Figs. 3.2, 3.3). This shows that a population of Lyn spatially re-distributes with IgE-FcεRI on the length scale of receptor clusters or slightly larger. Our ability to measure the initiation of Lyn association allows us to study the regulation of Lyn spatial co-redistribution with IgE-FcεRI at this early stage of signaling. These experiments build upon electron microscopy measurements of Lyn/IgE-FcεRI co-localization (2, 3) and additionally investigate regulation of Lyn by the actin cytoskeleton.

Our results demonstrate a regulatory role for the actin cytoskeleton that is at work even at these early times following antigen stimulation. Disruption of stimulated actin polymerization leads to an enhancement of Lyn co-localization with IgE-FcεRI (Fig. 3.6), suggesting that actin negatively regulates signaling at this stage by physically segregating Lyn from clustered receptors. Increases in Lyn coupling to IgE-FcεRI correlate with enhanced phosphorylation of receptor clusters (Fig. 3.9, 3.9), consistent with the idea that modulation of spatial co-localization of Lyn and IgE-FcεRI has

consequences for signal initiation. Actin also affects receptor co-localization with PM-mEos3.2, a minimal construct that shares the order-preferring lipid anchorage of Lyn (Fig. 3.10), implying that association with ordered lipids could be a structural factor that facilitates regulation by actin via the membrane environment of Lyn.

Our conclusion that actin regulates phosphorylation of IgE-FcεRI clusters through spatial separation of Lyn from cross-linked receptors is complementary to existing theories that receptor activation by Lyn is enabled by redistribution of cross-linked receptors into an ordered lipid environment that allows it to associate with Lyn and affords protection from phosphatases (4–7). Together they reinforce the idea that spatial compartmentalization of signaling molecules on the plasma membrane is a key mechanism in the initiation of functional FcεRI signaling.

Through the studies described above we characterize changes in distribution and dynamics of IgE receptor and its co-localization with Lyn that accompany mast cell activation. We go on to explore factors that modify these properties of receptors and Lyn and that have an impact on signaling as a result, including the cholesterol content of the membrane and the participation of the actin cytoskeleton. Super-resolution fluorescence localization microscopy allows us to measure these antigen-stimulated changes at high resolution and under more physiological conditions, even in living cells. We are able to shed light on the role of spatial organization of signaling molecules in the antigen-stimulated response by imaging membrane structures, such as IgE-FcεRI clusters or co-clusters with Lyn, at length scales relevant to their function. We detect antigen-stimulated co-localization of clustered IgE-FcεRI with Lyn at earlier time points than previously possible with optical microscopy, and as a result we are able to identify

a role for actin in the regulation of the spatial association of Lyn with IgE-FcεRI. We can also characterize dynamic, simultaneous changes in antigen-induced clustering and immobilization of IgE-FcεRI in great detail and delineate this behavior into two distinct stages, which we then correlate with Ca²⁺ mobilization. In sum, our results suggest that the super-resolution imaging approach is well suited to experiments that probe signaling interactions during the initiation of the antigen-stimulated response. Our results motivate future work investigating the physical interactions that give rise to stimulated changes in the spatial arrangement and mobility of IgE receptors and signaling partners, and how they translate into processes that regulate the stimulated response and specific cell functions.

FUTURE DIRECTIONS

There is significant potential for uncovering details of the mechanism of actin regulation of Lyn coupling to cross-linked IgE through variations of the super-resolution imaging experiments described in Chapters 2 and 3. Our experiments using PM-mEos3.2 in Chapter 3 suggest the lipid environment of Lyn is a factor in regulation of Lyn by actin. This notion that the actin cytoskeleton regulates signaling through modulation of lipid phase heterogeneity has appeared through experimental as well as theoretical work (8–11), and could be further investigated in the context of actin regulation of Lyn in further super-resolution imaging experiments.

As a starting point, we could look for interactions between actin and Lyn as a function of antigen stimulation in 2-color fixed cell experiments similar to those described in Chapter 3. Our observation that actin regulates Lyn spatial organization

relative to IgE-Fc ϵ RI suggests that there is a direct or indirect interaction of actin with Lyn, which could produce detectable cross-correlations between Lyn and cortical actin even though we do not detect co-localization of actin with IgE-Fc ϵ RI. If we are able to detect Lyn association with actin, we could test the cholesterol dependence of this association through depletion of membrane cholesterol using M β CD. Additionally, two-color experiments on living cells where individual trajectories are examined relative to the density of a second labeled species, in analogy to the one-color experiment shown in Fig. 2.7, could be powerful in detecting Lyn interactions with actin that affect mobility; we could look at diffusion of Lyn relative to the density of actin to assess their interactions. Again, any observed interactions could be tested for cholesterol dependence using cholesterol perturbation.

An alternative approach to better understand a potential lipid-mediated interaction between Lyn and the actin cytoskeleton could be to investigate interactions of Lyn with an adaptor protein that might link it to the cytoskeleton. As mentioned in Chapter 3, Cbp/PAG binds the actin cytoskeleton via Ebp50 and ezrin and has been proposed to act as a link between the cytoskeleton and ordered membranes (12). Cpb/PAG itself is strongly associated with ordered lipids and binds Lyn (12–14). One possible hypothesis is that Cpb/PAG interacts with Lyn via their shared ordered lipid environment after Fc ϵ RI clustering, and that this interaction facilitates regulation of Lyn by actin. It would be interesting to see if Cbp/PAG has any antigen-stimulated association (or dissociation) with clustered IgE-Fc ϵ RI, Lyn, or actin, and if these potential interaction could be disrupted through perturbation of the cytoskeleton or membrane lipid order.

Super-resolution fluorescence localization microscopy remains a useful method to measure molecular interactions on the plasma membrane that give rise to nanoscale co-localization and affect the diffusion of signaling molecules. In future experiments, these capabilities can be used to detect and characterize interactions of Lyn with F-actin to determine the role of ordered lipids in mediating the regulation of Lyn by the actin cytoskeleton.

REFERENCES

1. Shelby, S.A., D. Holowka, B. Baird, and S.L. Veatch. 2013. Distinct stages of stimulated Fc ϵ RI receptor clustering and immobilization are identified through superresolution imaging. *Biophys. J.* 105: 2343–2354.
2. Veatch, S.L., E.N. Chiang, P. Sengupta, D.A. Holowka, and B.A. Baird. 2012. Quantitative nanoscale analysis of IgE-Fc ϵ RI clustering and coupling to early signaling proteins. *J Phys Chem B.* 116: 6923–6935.
3. Wilson, B.S., J.R. Pfeiffer, and J.M. Oliver. 2000. Observing Fc ϵ RI signaling from the inside of the mast cell membrane. *J. Cell Biol.* 149: 1131–1142.
4. Field, K.A., D. Holowka, and B. Baird. 1995. Fc ϵ RI-mediated recruitment of p53/56lyn to detergent-resistant membrane domains accompanies cellular signaling. *PNAS.* 92: 9201–9205.
5. Field, K.A., D. Holowka, and B. Baird. 1997. Compartmentalized Activation of the High Affinity Immunoglobulin E Receptor within Membrane Domains. *Journal of Biological Chemistry.* 272: 4276 –4280.
6. Sheets, E.D., D. Holowka, and B. Baird. 1999. Critical Role for Cholesterol in Lyn-mediated Tyrosine Phosphorylation of Fc ϵ RI and Their Association with Detergent-resistant Membranes. *J Cell Biol.* 145: 877–887.
7. Young, R.M., D. Holowka, and B. Baird. 2003. A Lipid Raft Environment Enhances Lyn Kinase Activity by Protecting the Active Site Tyrosine from Dephosphorylation. *Journal of Biological Chemistry.* 278: 20746 –20752.
8. Han, X., N.L. Smith, D. Sil, D.A. Holowka, F.W. McLafferty, and B.A. Baird. 2009. IgE receptor-mediated alteration of membrane-cytoskeletal interactions revealed by mass spectrometric analysis of detergent-resistant membranes. *Biochemistry.* 48: 6540–6550.
9. Honigsmann, A., S. Sadeghi, J. Keller, S.W. Hell, C. Eggeling, and R. Vink. 2014. A lipid bound actin meshwork organizes liquid phase separation in model membranes. *eLife.* 3.
10. Machta, B.B., S. Papanikolaou, J.P. Sethna, and S.L. Veatch. 2011. Minimal Model of Plasma Membrane Heterogeneity Requires Coupling Cortical Actin to Criticality. *Biophysical Journal.* 100: 1668–1677.
11. Ehrig, J., E.P. Petrov, and P. Schwille. 2011. Near-critical fluctuations and cytoskeleton-assisted phase separation lead to subdiffusion in cell membranes. *Biophys. J.* 100: 80–89.

12. Hrdinka, M., and V. Horejsi. 2014. PAG - a multipurpose transmembrane adaptor protein. *Oncogene*. 33: 4881–4892.
13. Itoh, K., M. Sakakibara, S. Yamasaki, A. Takeuchi, H. Arase, M. Miyazaki, N. Nakajima, M. Okada, and T. Saito. 2002. Cutting edge: negative regulation of immune synapse formation by anchoring lipid raft to cytoskeleton through Cbp-EBP50-ERM assembly. *J. Immunol.* 168: 541–544.
14. Ohtake, H., N. Ichikawa, M. Okada, and T. Yamashita. 2002. Cutting Edge: Transmembrane Phosphoprotein Csk-Binding Protein/Phosphoprotein Associated With Glycosphingolipid-Enriched Microdomains as a Negative Feedback Regulator of Mast Cell Signaling Through the FcεRI. *J Immunol.* 168: 2087–2090.

APPENDIX A

SUPER-RESOLUTION IMAGING OF IgE RECEPTOR CROSS-LINKING BY STRUCTURALLY-DEFINED LIGANDS IN RBL MAST CELLS

MOTIVATION AND BACKGROUND

To further understand the physical requirements for initiation of FcεRI signaling through receptor clustering, we use structurally-defined trivalent ligands specific for anti-dinitrophenyl (DNP) IgE, for which the ligand size and valency is controlled, to cross-link IgE-FcεRI. In this appendix we present preliminary data where we record organization and dynamics of IgE-FcεRI during cross-linking through live cell super-resolution fluorescence localization microscopy experiments analogous to the live cell experiments presented in Chapter 2.

These structurally-defined DNP ligands, designated $Y_n\text{DNP}_3$ are based on a Y-shaped double-stranded DNA scaffold with DNP groups conjugated to each of the three 5' ends. The distance between DNP groups is fixed by the length (n bases) of single-stranded oligonucleotides annealed to form the Y-shaped structure (Fig. A1). Because DNP groups are nearly co-planar, distance between DNPs is set by the length of oligonucleotides. As described previously for these $Y_n\text{DNP}_3$ ligands (1, 2), some (but not other) cell signaling pathways depend on inter-DNP distances, ranging from 5 – 15 nm, which constrain the proximity of ligand-bound IgE-receptors. $Y_n\text{DNP}_3$ ligands are uniform in size and valency, which allows us to assign signaling outcomes to the specific structure of ligands and resulting receptor clusters.

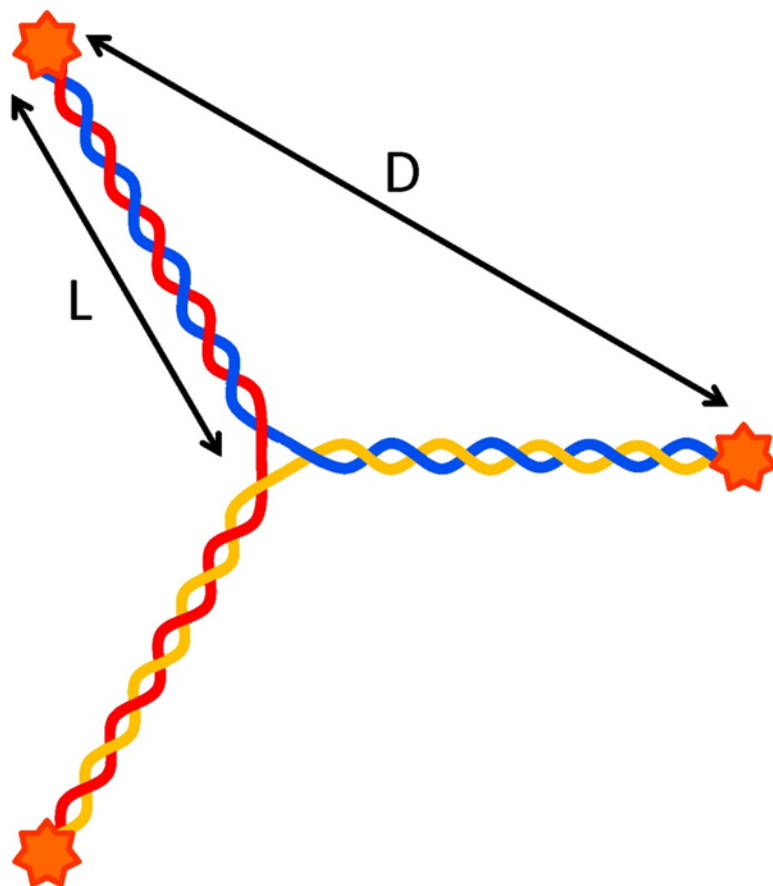


Fig. A1 Schematic of $Y_n\text{DNP}_3$ ligands. Ligands are based on a double-stranded DNA scaffold consisting of 3 annealed oligonucleotides of n bases. Oligonucleotides are conjugated on each 5' end with a dinitrophenyl (DNP) group. Ligands composed of oligonucleotides of a given length have characteristic dimensions L , the distance between the vertex of the ligand and the DNP group, and D , the distance between DNP groups.

We compare the effects of $Y_n\text{DNP}_3$ with two different characteristic lengths, $Y_{16}\text{DNP}_3$ and $Y_{46}\text{DNP}_3$. $Y_{16}\text{DNP}_3$, which has an inter-DNP spacing close to 5nm, elicits receptor phosphorylation and degranulation responses to a higher degree than $Y_{46}\text{DNP}_3$, which has an inter-DNP spacing around 15nm (1). We also compare stimulation with $Y_n\text{DNP}_3$ to stimulation with the multivalent antigen DNP-BSA, which has an average of 20 DNP groups bound. We find that both DNP-BSA and $Y_{16}\text{DNP}_3$ cause a sharp decrease in mobility upon ligand addition, but produce IgE-receptor clusters that appear distinctive in size and density. $Y_n\text{DNP}_3$ -stimulated changes occur on a shorter time scale when matched for DNP concentration with DNP-BSA.

RESULTS AND DISCUSSION

RBL-2H3 cells are sensitized with AlexaFluor 647 IgE and imaged using super-resolution fluorescence localization microscopy as described in Chapter 2. Imaging methods and data analysis procedures to characterize IgE-Fc ϵ R1 diffusion and organization are identical to those described in Chapter 2 for live cell super-resolution imaging, where they are illustrated in detail. The only point of difference for the experiments described here is the type and concentration of the antigen used for stimulation. In the experiments described below, $Y_{16}\text{DNP}_3$ and $Y_{46}\text{DNP}_3$ are added at concentrations of 25nM and 5nM for stimulation. For comparison, live cell data from experiments where 1.5nM (or .1 μ g/ml) DNP-BSA is used to stimulate cells are reproduced from Figs. 2.13 and 2.14.

IgE receptor clustering and immobilization after addition of Y_nDNP_3 are quantified using spatial correlation functions and single particle tracking in super-resolution images.

Fig. A2 shows super-resolution images of a representative live cell that is stimulated with 25nM $Y_{16}DNP_3$, which was prepared as previously described (1). Receptors are clearly clustered even at the .5 min time point after stimulation as evidenced by visual inspection of super-resolution images. Pair auto-correlation functions as a function of stimulation time are shown for the same representative live cell (Fig. A3, A) and are fit to a single exponential function to quantify the size and density of cross-linked domains:

$$g_{\text{fit}}(r) = 1 + A \exp(-r/\xi)$$

where A is the amplitude of the correlation and is related to cluster density, ξ is the correlation length and is related to average cluster size. The average number of correlated proteins in clusters is the integral of the correlation function, denoted N . These parameters as a function of stimulation time, as averaged over 10 live cell experiments, show that the correlation length decreases, while the correlation amplitude and the average number of correlated proteins increase quickly after the addition of 25 nM $Y_{16}.DNP_3$ at time = 0min (Fig. A3, B).

Diffusion is measured through tracking individual receptors and assembling displacements into MSD curves for each 500 frame segment of acquired raw data as in Chapter 2. Fig. A4, A shows MSD curves for the representative live cell shown in Fig. A1 as a function of stimulation time. MSD curves are fit to:

$$\text{MSD}(t_{2-4}) = 4D_S t_{2-4} + C$$

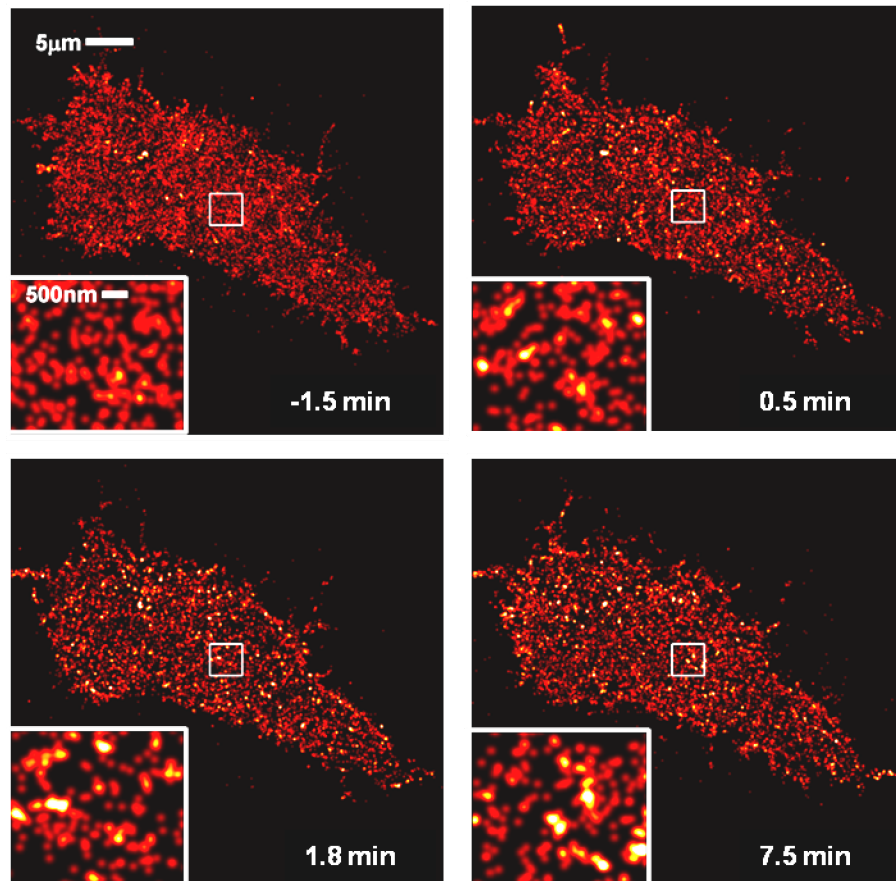


Fig. A2 $Y_{16}DNP_3$ addition causes rapid clustering of IgE-Fc ϵ RI in super-resolution images. Reconstructed super-resolution fluorescence localization images of an AF647-IgE-labeled living cell at various times in the stimulation sequence, where 25 nM $Y_{16}DNP_3$ is added at 0 min. Each image is reconstructed from 68s of acquired data. Insets show magnified images of the regions outlined with white squares.

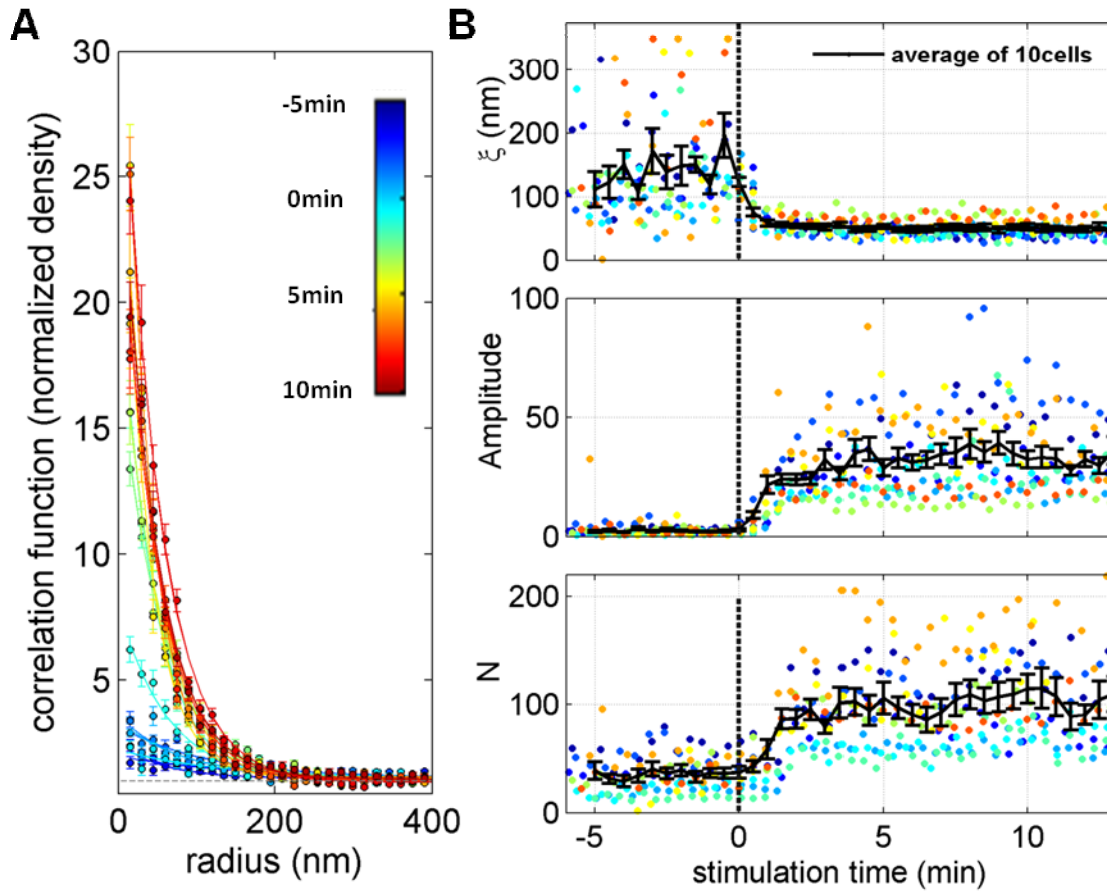


Fig. A3 Pair auto-correlation functions are used to quantify receptor clustering as a function of $Y_{16}DNP_3$ stimulation time. (A) Auto-correlation functions, $g(r)$, are calculated from reconstructed single molecule centers acquired over 16s as described in Ch. 2 (solid circles) and are fit to single exponentials (solid lines). (B) Correlation function parameters from 10 live cell experiments, distinguished by different colors: the correlation length, ξ (top), the correlation amplitude, A (middle), and the average number of correlated proteins, N (bottom). Solid black lines indicate averages over 10 cells, and error bars represent standard error of the mean.

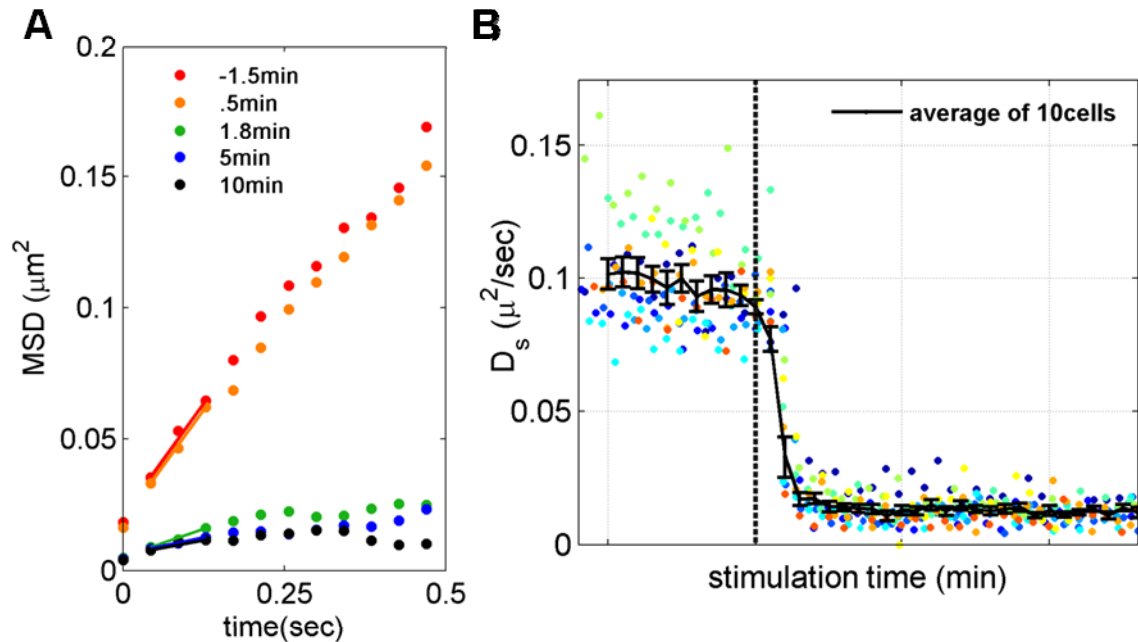


Fig. A4 Average IgE-Fc ϵ RI mobility drops quickly after Y₁₆DNP₃ addition. (A) Mean squared displacement (MSD) curves are generated for a representative live cell experiment by averaging over all IgE-Fc ϵ RI trajectories observed within a 500 frame time-period at the times during stimulation after addition of 25 nM Y₁₆DNP₃ as indicated, and as described in Ch. 2. MSD curves are fit to the equation $MSD(t_{2-4}) = 4D_S t_{2-4} + C$ to extract the short time diffusion coefficient D_S . (B) Summary of D_S extracted from MSD curves tabulated from single molecule trajectories acquired over 500 frames (approximately 20s and variable from cell to cell) for 10 distinct cells. Error bars represent standard error of the mean of the 10 live cell experiments.

to obtain the short time diffusion constant D_s . For the ensemble of 10 live cell experiments, the mobility of receptors quickly decreases after Y_{16} -DNP₃ is added at 0 min (Fig. A4, B).

Cluster structural properties and receptor mobility depend on the stimulating ligand.

To compare the effects of Y_{16} -DNP₃ stimulation on the mobility and organization of IgE-FcεRI to changes induced by Y_{46} -DNP₃ or DNP-BSA, we conducted analogous live cell experiments using Y_{46} -DNP₃ to stimulate cells. DNP-BSA data are reproduced from Figs. 2.13 and 2.14. The average fit parameters A , ξ , N , and D_s as a function of stimulation time for cells stimulated with 5nM or 25nM Y_{16} -DNP₃, 5nM or 25nM Y_{46} -DNP₃, and 1.5nM DNP-BSA are compared in Fig. A5. Y_{16} -DNP₃ produces significantly smaller, denser clusters than Y_{46} -DNP₃ or DNP-BSA as signified by lower values of ξ and larger values of A in stimulated cells. Y_{16} -DNP₃ also causes a faster increase in values of N compared to Y_{46} -DNP₃ at early stimulation time points, but not at later stimulation time points. Y_{16} - and Y_{46} -DNP₃ both cause faster immobilization of receptors compared to DNP-BSA as measured by D_s .

We compare the relationship between D_s and N for Y_{16} -DNP₃, Y_{46} -DNP₃, and DNP-BSA stimulation as in Fig. 2.5, A (Fig. A6). Unlike Y_{16} -DNP₃ and DNP-BSA, immobilization of Y_{46} -DNP₃ is not accompanied by a substantial increase in N .

The population of receptors is quickly immobilized and clustered by Y_{16} -DNP₃.

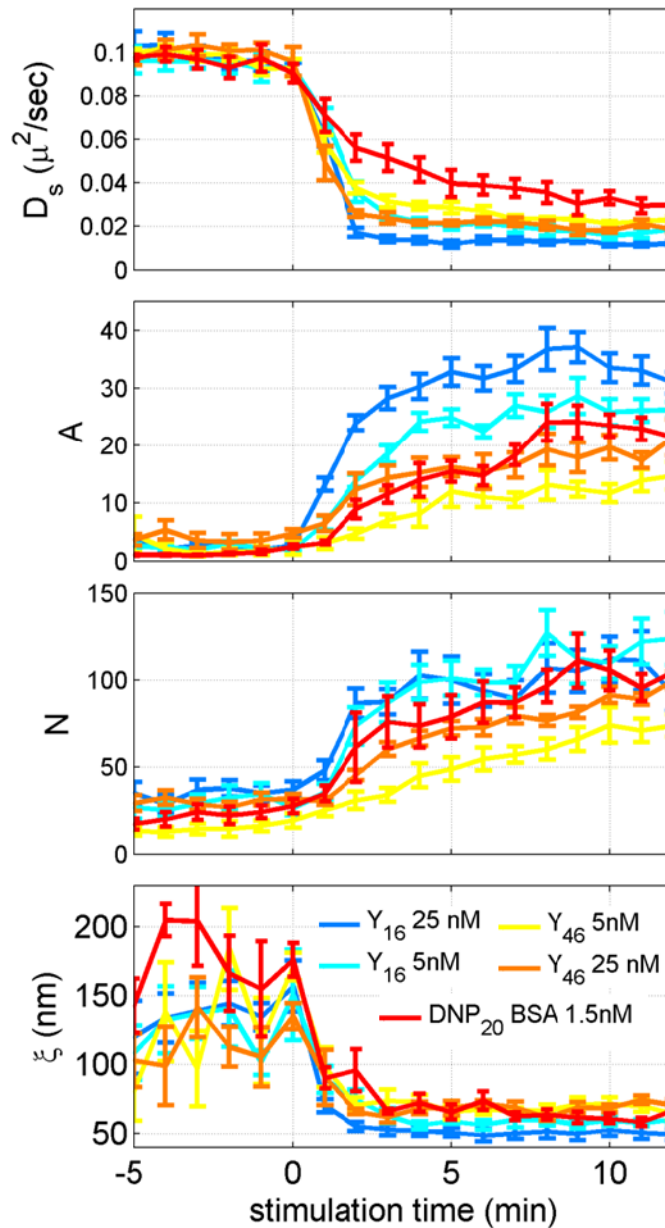


Fig. A5 IgE-Fc ϵ RI mobility and average physical properties of clusters depend on the stimulating ligand. Average values of the short time diffusion constant D_s , auto-correlation amplitude A , number of correlated proteins N , and cluster diameter ξ are shown for live cells stimulated with low (5 nM) or high (25 nM) doses of $Y_{46}\text{DNP}_3$ and $Y_{16}\text{DNP}_3$ or 1.5 nM DNP-BSA.

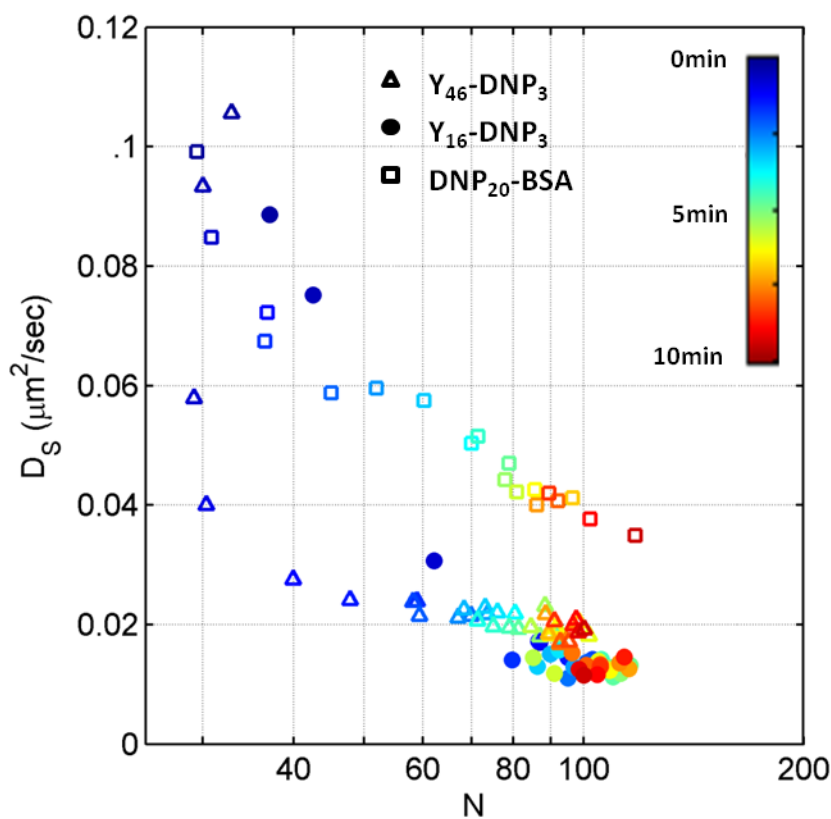


Fig. A6 The relationship between ligand-induced immobilization and number of correlated proteins depends on the ligand used. Average D_s is shown as a function of average number of correlated proteins N from the same live cell experiments for cells stimulated with 1.5 nM DNP-BSA (open squares), 25 nM $Y_{16}\text{DNP}_3$ (filled circles), or 25nM $Y_{46}\text{DNP}_3$ (open triangles) . Each point corresponds to values of D_s and N at a given time after stimulation averaged over the cells imaged for each stimulation condition, and data from individual cells are binned every 15 s to facilitate averaging. Time after the addition of ligand is indicated by the color bar.

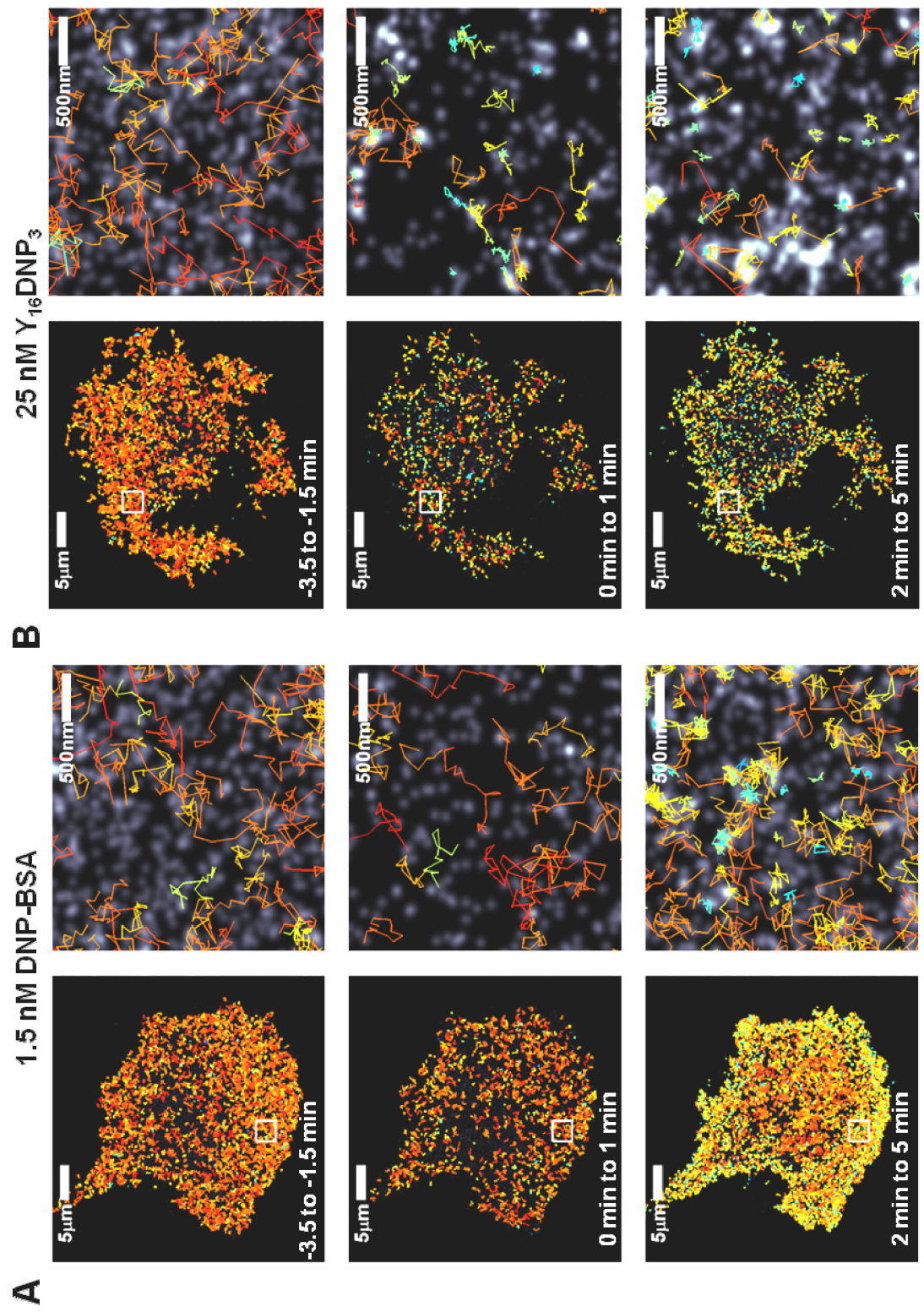
To correlate receptor localization with mobility, single molecule trajectories persisting for at least 0.5 sec are superimposed on reconstructed super-resolution images as in Fig. 2.7 (Fig. A7). Histograms of single-trajectory diffusion constants and 3-dimensional histograms of diffusion constants and receptor density estimated from average pixel grayscale values of the positions in the trajectory (Fig. A8) are constructed from trajectories and super-resolution images. These histograms suggest that Y_{16} -DNP₃ causes fast, uniform conversion of the receptor population receptors from high mobility in areas of low receptor density to low mobility within higher-density clusters. For DNP-BSA, a portion of the population of receptors remains mobile even at longer stimulation times. This result reflects the increased immobilization rate of receptors and faster increase in N upon stimulation with Y_{16} -DNP₃ vs. DNP-BSA. Together, these data show that cluster formation and receptor immobilization occurs more quickly and uniformly for Y_{16} -DNP₃ vs. DNP-BSA.

This difference as well as the faster immobilization shown in Fig. A6 can be explained by faster binding kinetics of Y_n -DNP₃ ligands (1) compared to DNP-BSA. DNP groups on the surface of DNP-BSA transiently associate with the surface of the protein, limiting the exposure of DNP groups at any given time and prolonging the binding of accessible DNP groups to IgE (4). Slower cross-linking kinetics of the DNP-BSA ligand caused by transient hapten exposure accounts for the long-lived fraction of mobile receptors we observe in experiments where mobility of individual IgE-FcεRI complexes are measured (Fig. A7 and A8).

CONCLUSIONS

Fig. A7 Live cell images reflect ligand-induced immobilization of the population of IgE-FcεRI complexes. Single molecule trajectories of A647 IgE persisting for at least 0.5 sec are superimposed on a reconstructed super-resolution image showing unstimulated data (top images), data taken within 1min of antigen addition (middle images), and between 2 and 5 minutes (bottom images). Track coloring indicates the calculated diffusion constant for each track on a log scale from $10^{-5} \mu\text{m}^2/\text{sec}$ (blue) to $1 \mu\text{m}^2/\text{sec}$ (red). A representative cell stimulated with 1.5 nM DNP-BSA at time = 0 min is shown in (A), and a cell stimulated with 25 nM $Y_{16}\text{DNP}_3$ is shown in (B).

Fig. A7



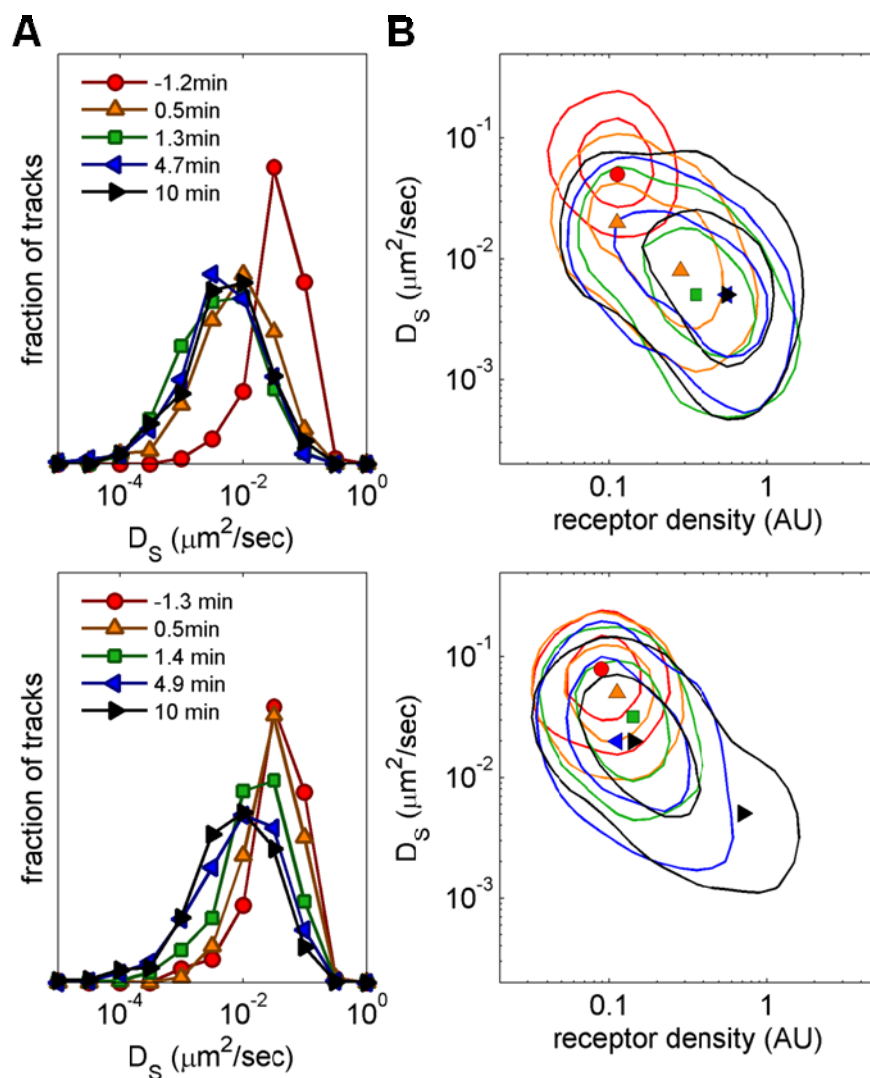


Fig. A8 The whole population of IgE-Fc ϵ RI complexes is more rapidly immobilized by Y₁₆DNP₃ stimulation than by DNP-BSA. Diffusion behavior of individual IgE-Fc ϵ RI complexes in a representative live cell experiment where the cell is either stimulated with 25 nM Y₁₆DNP₃ (top) or 1.5 nM DNP-BSA (bottom) (A) Short time diffusion coefficients (D_S) are evaluated from MSD curves tabulated from single molecule trajectories lasting at least 0.5 s within a 16 s time-period, and are assembled into histograms. Histograms are normalized by the total number of tracks collected to generate each histogram (D) 3-dimensional histograms of D_S vs. average receptor density along trajectories lasting at least 0.5 s. Average receptor density for each trajectory is determined by averaging the pixelated grayscale values from the time-averaged reconstructed image over all positions of the trajectory and then normalizing assuming $\rho_{ave}=200/\mu\text{m}^2$, as described in Chapter 2.

We use super-resolution imaging to characterize the single molecule details of IgE receptor clustering upon exposure to ligands of different valency, heterogeneity, binding kinetics, and inter-DNP distance. Cross-linking of IgE-FcεRI with Y₁₆-DNP₃ results in receptor clusters that are structurally different from clusters cross-linked with DNP-BSA and Y₄₆-DNP₃. We find that Y₄₆-DNP₃ receptors immobilize before forming large cross-linked domains, and note that the reduced ability of Y₄₆-DNP₃ stimulation to cause receptor phosphorylation and degranulation has no effect on immobilization, suggesting that another ligand-stimulated process is responsible for receptor immobilization. Instead, the measured differences in the spatial arrangement of receptors, in particular the size and density of clusters, may be directly related to the observed differences in the capacity of Y₁₆-DNP₃ and Y₄₆-DNP₃ to stimulate degranulation. Due to their structural homogeneity, Y_nDNP₃ ligands will provide a useful tool to study the clustering-dependent IgE-receptor association with membrane structures and downstream signaling partners, and to explore the dependence of these associations on ligand structure.

REFERENCES

1. Sil, D., J.B. Lee, D. Luo, D. Holowka, and B. Baird. 2007. Trivalent ligands with rigid DNA spacers reveal structural requirements for IgE receptor signaling in RBL mast cells. *ACS Chem. Biol.* 2: 674–684.
2. Holowka, D., D. Sil, C. Torigoe, and B. Baird. 2007. Insights into immunoglobulin E receptor signaling from structurally defined ligands. *Immunol. Rev.* 217: 269–279.
3. Shelby, S.A., D. Holowka, B. Baird, and S.L. Veatch. 2013. Distinct stages of stimulated Fc ϵ RI receptor clustering and immobilization are identified through superresolution imaging. *Biophys. J.* 105: 2343–2354.
4. Xu, K., B. Goldstein, D. Holowka, and B. Baird. 1998. Kinetics of Multivalent Antigen DNP-BSA Binding to IgE-Fc ϵ RI in Relationship to the Stimulated Tyrosine Phosphorylation of Fc ϵ RI. *J. Immunol.* 160: 3225–3235.

APPENDIX B

REGISTRATION OF TWO-COLOR SUPER-RESOLUTION FLUORESCENCE LOCALIZATION IMAGES.

MOTIVATION AND BACKGROUND

Two-color fluorescence localization microscopy is a powerful tool for characterizing spatial co-localization and interactions of biological molecules. In Chapter 3, we describe two-color super-resolution experiments where cross-correlation functions are used to characterize interactions between IgE-Fc ϵ RI and various signaling species on the membrane. In this appendix we illustrate the method used to attain registration of the two imaging channels that has sufficiently low error for this quantitative treatment of super-resolution data.

For EMCCD cameras and magnifications commonly used for super-resolution microscopy, single camera pixels span 100nm or more of the field of view. Channel alignment errors must be at or below the imaging resolution of individual channels in order to prevent channel alignment error from limiting the overall resolution of a two-color image. Therefore, because typical super-resolution imaging resolution is in the tens of nanometers, quantitative two-color fluorescence localization microscopy requires precise sub-pixel registration of imaging channels. Here, we accomplish this precise alignment through a strategy similar to previously published methods (1). We image a calibration sample of multi-color fluorescent beads and construct a registration transformation that can be used to align two-color super-resolution data.

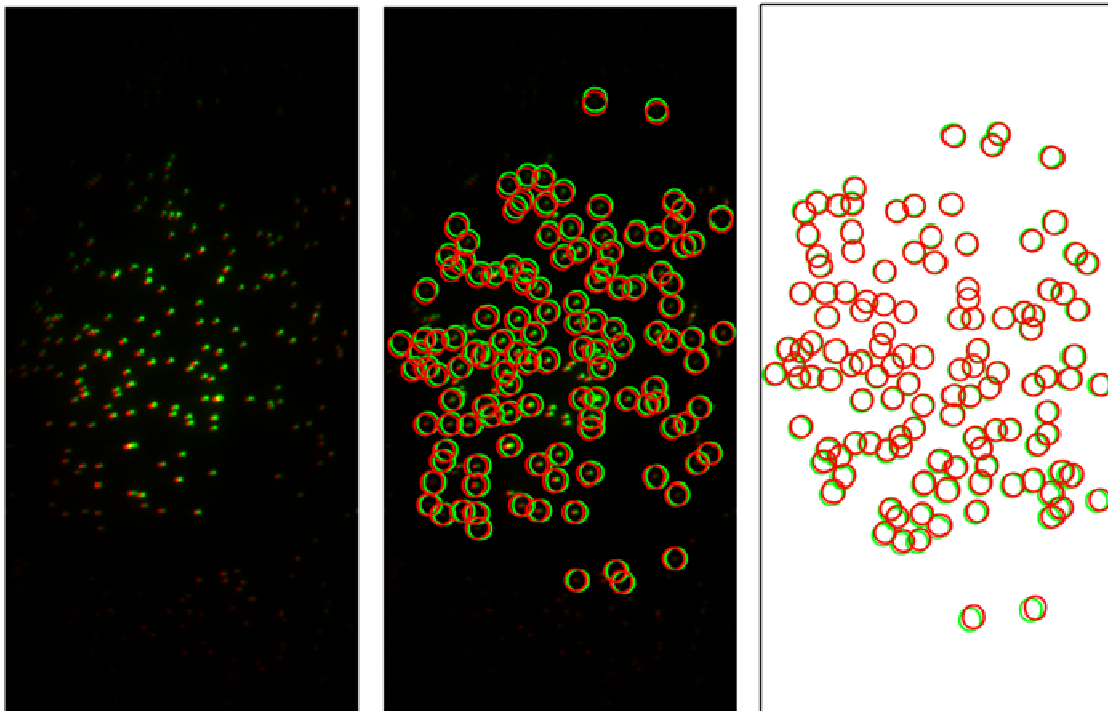
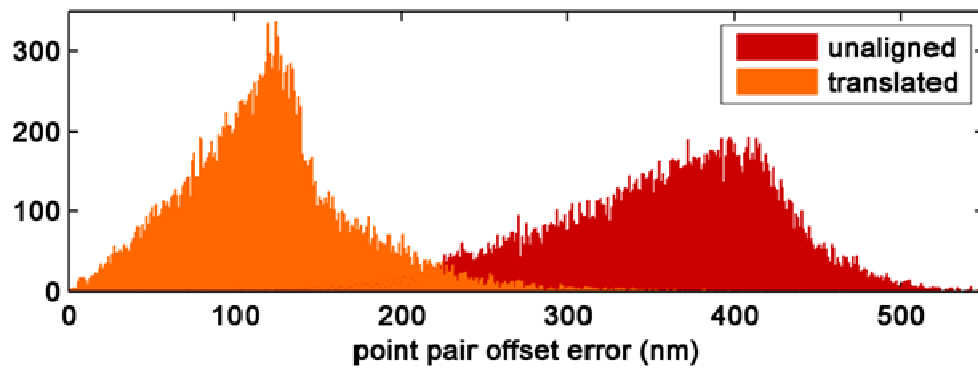
RESULTS AND DISCUSSION

Characterization of offset error

Optical strategies for splitting emission channels in two-color fluorescence imaging often inherently introduce non-uniform offsets between imaging channels. That is, misalignment that cannot be resolved simply by translation of one channel with respect to each other. These offsets can be clearly visualized through imaging of an alignment sample of fluorescent nanospheres labeled with multiple dyes. Nanospheres are imaged in both channels, and nonlinear offsets are evident when the channels are superimposed (Fig. B1, A).

Offsets can be quantified through localization of diffraction-limited fluorescent spots of individual nanospheres (Fig. B1, A, middle). Coordinates of a given individual nanosphere in each of the two imaging channels can be compared to assess offset error. Through localization of nanospheres in many two-color images, large sets of control point pairs are amassed to estimate average offset error across the imaging field of view. Even when one channel is translated to minimize offset error between control points, average offset errors still extend far beyond the resolution of a single-color fluorescence localization image (Fig. B1, A, right and Fig. B1, B). This is due to the fact that offset errors are not uniform across the field of view. When one channel is translated, offset errors are small in the center of the field of view but become larger as they approach the edges (Fig. B1, A, left).

Fig. B1 Two-color imaging systems have significant nonlinear offsets between channels that extend well beyond the resolution of a single-color fluorescence localization image. Tetraspeck fluorescent nanospheres are labeled with multiple dyes and are imaged in two color channels, represented here as red and green. Channels are split chromatically using an emission splitter that redirects the channels onto two halves of the camera CCD. When the images are overlaid (A, left), red and green images are clearly offset. Nanospheres are localized in each image (A, middle), and localizations are represented as red and green circles. Even when the set of green localizations are translated to maximize overlay with red localizations (A, right), offsets are still evident around the edges of the field of view. (B) This procedure is repeated for many fields of view to amass a large set of localization pairs. Histograms of offset errors for localization point pairs are shown for localizations when channels are overlaid without alignment and when the set of green localizations is translated to minimize offset error with red localizations.

A**B**

For the example experiments illustrated here, we use the green and far-red emission channels to image fluorescent nanospheres. In general, we observe that alignment offsets between the green and far-red emission channels are larger on average than offsets between red and far-red emission channels. Thus, the offset errors described here are representative of the upper limit of offsets observed in typical two-color experiments.

Localizations of fluorescent nanospheres are used as control points to infer a spatial transformation that is applied to one of the channels for registration.

Due to the inefficacy of simple translational transformations for channel alignment, we need a different approach to ensure that the two channels are aligned over the entire field of view. We use large sets of control points to infer a spatial transformation for two-color image registration through using the built-in Matlab function *cp2tform()*. A more complicated transformation form than simple translation is needed to capture non-uniformity of offset errors across the field of view. Transforms are tabulated using the "local weighted mean" or "lwm" method, which calculates a second-order polynomial centered at each control point using the surrounding 10 control points. The transform at a given position is the sum of polynomials weighted by proximity to control points at which each polynomial is centered. This is a piecewise transformation, that is, the functional form of the transformation varies in space. Accurate calculation of transformations of this form requires a high density of control points but can accommodate high local variability of offset errors across the field of view.

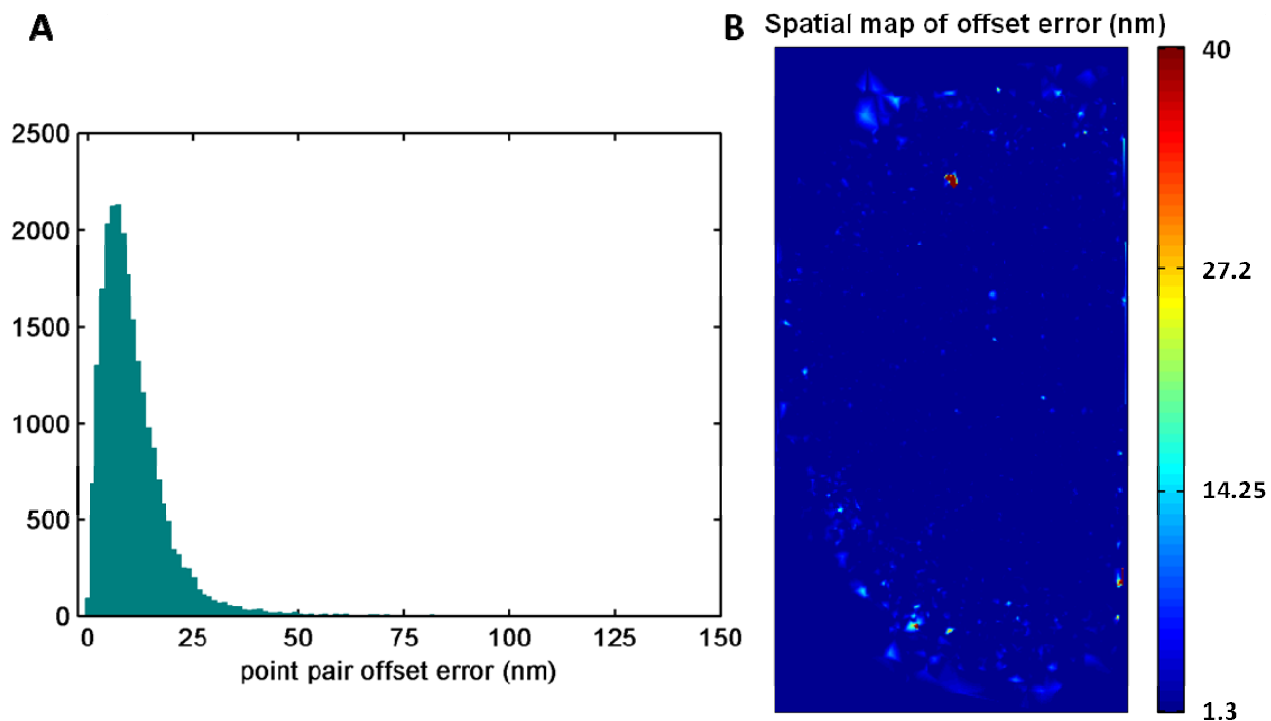


Fig. B2 One channel can be effectively spatially mapped onto the other using a piecewise, non-linear transformation. Large sets of nanosphere localization pairs (approximately 10,000 pairs) are used as control points to calculate a "local weighted mean" transformation that maps one channel onto the other. (A) Histogram of remaining offset errors for localization pairs when this transformation is applied to localizations in one channel. (B) A spatial map of offset errors in the field of view is generated when offset errors are plotted according to the location of control points. The spatial map or errors is a representation of expected error due to channel misalignment in a two-color fluorescence localization image across the field of view.

When applied, "lwm" transforms reduce average offset errors between channels to levels below the imaging resolution of individual channels of approximately 20nm (Fig. B2, A). Residual offset errors are relatively uniform across the field of view, although isolated areas of high error can remain (Fig. B2, B).

Transforms are sensitive to alignment drift.

Subtle drift in the optical components of an emission splitter system or drift of the entire unit with respect to the microscope body can lead to misalignment of channels over time. If transforms are calculated from sets of nanosphere images that are collected at 5 min intervals and the translational component of these transforms are compared, we observe that the translational component of the transform drifts across approximately 20nm over a 45 min period (Fig. B3). For this reason, mechanical stabilization of the emission splitting system through firm attachment to the optical table is recommended to minimize drift. Transforms are also calculated from nanosphere images collected immediately before and after fluorescence localization imaging of each sample to reduce the effects of transformation drift.

Control experiments confirm precise registration.

As a control experiment to test our channel alignment method, a given field of view of nanospheres is imaged in a sequence of 500-frame movies to mimic fluorescence localization microscopy data collection. Nanospheres are localized in each frame and a "super-resolution" image of the nanospheres is rendered as described in Chapters 2 and 3, except that here we count consecutive localizations recorded from

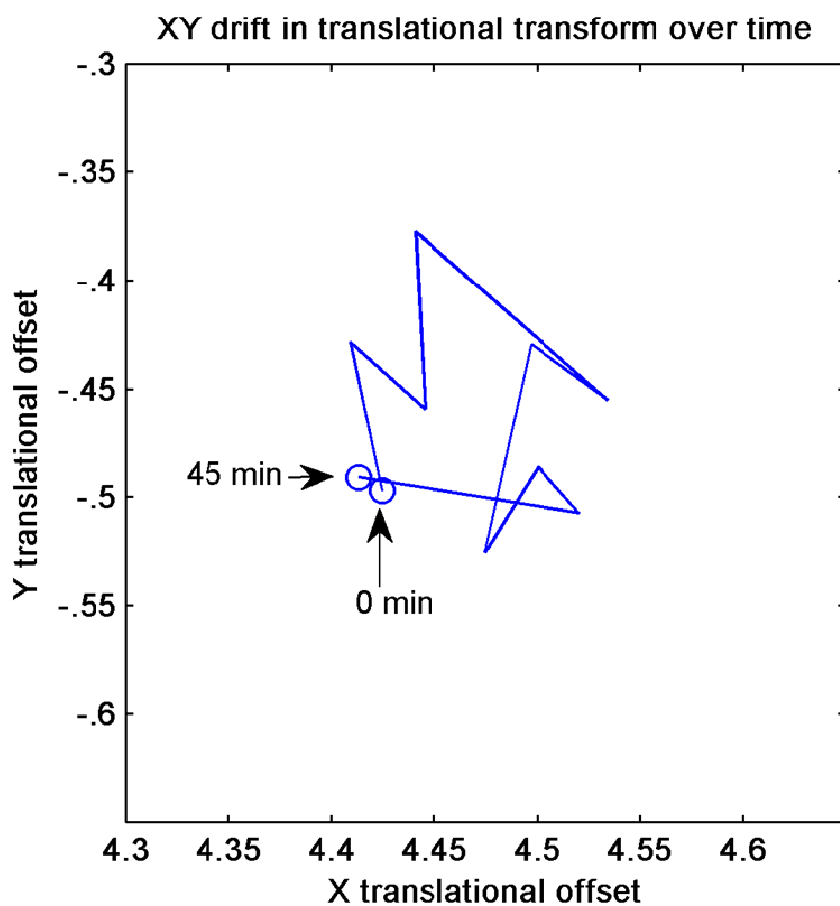


Fig. B3 The drift in the emission splitting system can cause drift in the alignment transformation over time. Sets of nanosphere images for calculation of a channel alignment transformation were recorded every 5 min for 45 min. The translational component was averaged and plotted in units of pixels for each transformation. The average translational component drifted over a range of approximately .15 pixels or 22nm in x and y directions over the course of 45 minutes. This time is comparable to the time frame for collection of fluorescence localization images, which is typically approximately 20 min.

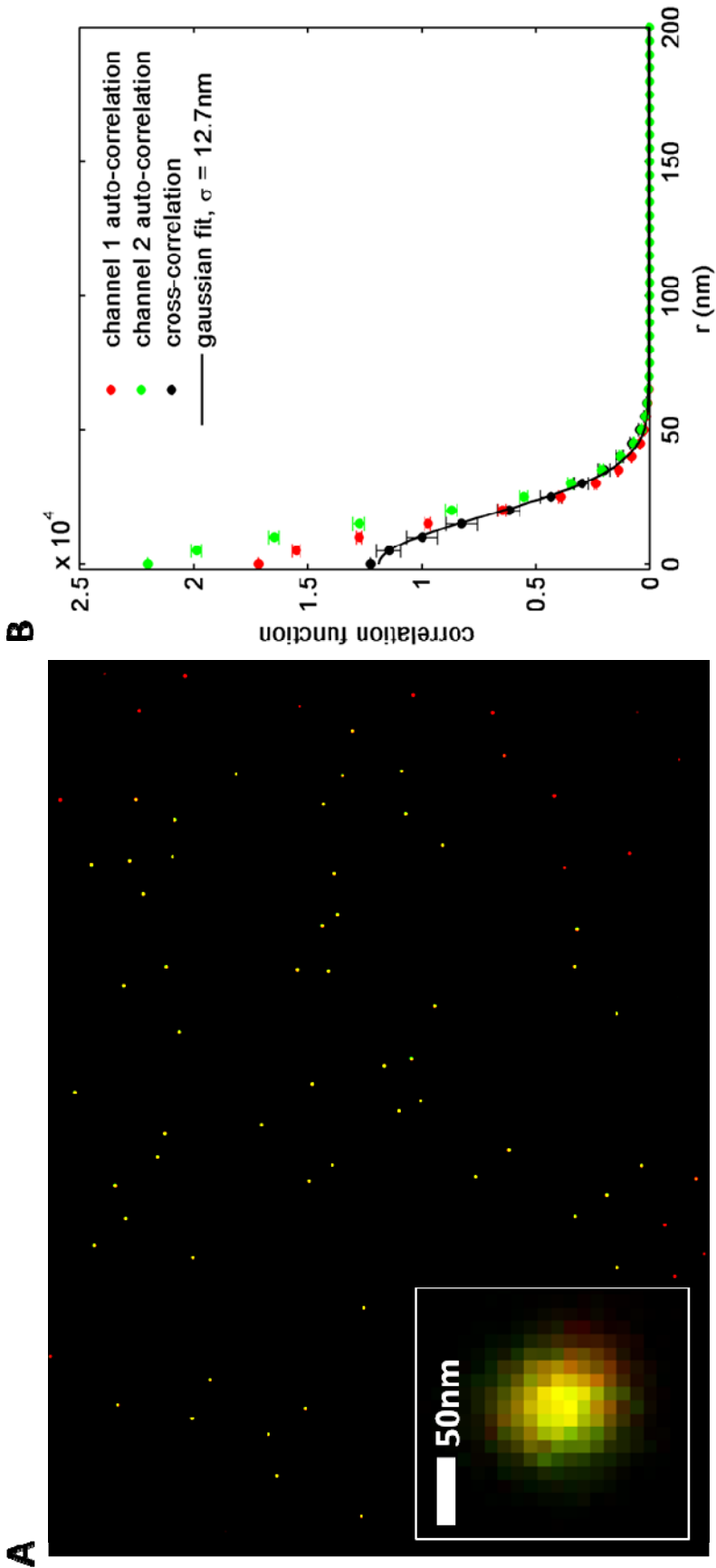
the same nanosphere separately instead of merging them. Nanospheres appear well aligned in the super-resolution image and in a zoomed image of a single nanosphere (Fig. B4, A). Some nanospheres in the super-resolution image appear red or green only, as opposed to yellow, due to lack of complete overlap of 488nm and 642nm TIRF illumination. The cross-correlation of nanosphere localizations is computed for the two-color image as described in Chapter 3 (Fig. B4, B). Nanosphere cross-correlation functions can be interpreted as the point spread function of a two-color super-resolution image. In light of this interpretation, we fit the cross-correlation function to a Gaussian form, and find that the nanosphere cross-correlation function has a standard deviation of 12.7nm. This value is well below the lowest imaging resolution obtained in either channel for single-color super-resolution images of labeled cells, approximately 20nm. This confirms that we can align the two channels with sufficient accuracy so that registration is not a limiting factor in the resolution of two-color image analysis.

CONCLUSIONS

Commercially available systems for two-color fluorescence imaging can introduce misalignments between imaging channels that are not uniform across the field of view. This is not a significant hurdle for conventional fluorescence imaging, because imaging resolution is limited by diffraction to several hundred nanometers, and this length scale can span several camera pixels at relatively high magnification. Channel misalignment can be characterized by localizing multicolor fluorescent nanospheres in each channel and comparing the spatial coordinates obtained for each channel. In our system, average misalignment between pairs of control points is over 100nm, even after

Fig. B4 Control experiments using fluorescent nanospheres that simulate super-resolution localization data collection routines confirm channel alignment. Fluorescent nanospheres in a single field of view were imaged in a series of 500-frame movies. These raw data were analyzed using the same method as is used for super-resolution fluorescence localization data of labeled cells, except that localizations of the same nanosphere in consecutive frames were not merged. An alignment transformation was calculated from nanosphere images of many fields of view collected before and after movies were acquired. The transformation was applied to one channel of nanosphere localizations collected in movies to align the images. Super-resolution images of nanospheres were rendered (A), and auto- and cross-correlation functions of localizations in the two channels were calculated (B). In (A), the rendered image shows that nanospheres are well registered over the field of view. The inset shows a zoomed image of a single nanosphere, where here localizations from each channel are binned into 5 nm pixels for display. The cross-correlation function calculated from nanosphere localizations is representative of the PSF or resolution of a nanosphere in the two-color image. It is fit to a Gaussian function and has a standard deviation of 12.7 nm.

Fig. B4



one channel is translated to minimize misalignment. Because imaging resolution for individual single-color images of labeled cells is around 20nm, much lower than offset errors between channels, quantitative measurements of co-localization using cross-correlation functions are limited by offset error.

We created a spatial map of offset errors by collecting many two-color images of fluorescent nanospheres and localizing them in each channel, such that the field of view is well sampled. We use corresponding nanosphere localizations in each channel as control points to infer a spatial transformation that maps one channel onto the other. Through application of this transformation, offset error is reduced to levels below fluorescence localization imaging resolution.

To confirm that our alignment method is sufficient for quantitative analysis using cross-correlation functions, we compute the cross-correlation function for nanospheres that are imaged and localized in a series of 500-frame movies, in analogy to our method for fluorescence localization data collection for labeled cells. The width of the cross-correlation function is below the fluorescence localization imaging resolution for labeled cells. Overall, our measurements of remaining offset error following channel alignment indicate that we can use this method to allow pair-correlation analysis for two-color images.

REFERENCES

1. Churchman, L.S., Z. Okten, R.S. Rock, J.F. Dawson, and J.A. Spudich. 2005. Single molecule high-resolution colocalization of Cy3 and Cy5 attached to macromolecules measures intramolecular distances through time. *Proc. Natl. Acad. Sci. U. S. A.* 102: 1419–1423.